2018

Effect of Nano-Pore Wall Confinements on Non-Ideal Gas Dynamics in Organic Rich Shale Reservoirs

Nupur Gupta

Effect of Nano-Pore Wall Confinements on Non-Ideal Gas Dynamics in Organic Rich Shale Reservoirs

Nupur Gupta

Thesis submitted to the
Benjamin M. Statler College of Engineering and Mineral Resources
at West Virginia University

in partial fulfillment of the requirements for the degree of

MASTER OF SCIENCE in
Petroleum and Natural Gas Engineering

Ebrahim Fathi, Ph. D., Chair
Ali Takbiri Borujeni, Ph. D.
Fatemeh Belyadi, Ph. D.

Department of Petroleum and Natural Gas Engineering

Morgantown, West Virginia
2018

Keywords: Lattice Boltzmann modeling, shale gas reservoir, non-ideal gas dynamics, pore wall confinement, Klinkenberg, slippage

Abstract

Effect of Nano-Pore Wall Confinements on Non-Ideal Gas Dynamics in Organic Rich Shale Reservoirs

By

Nupur Gupta

The advancements in horizontal well drilling and multistage hydraulic fracturing technology enabled us to unfold major sources of hydrocarbon trapped in ultra-tight formations such as tight sands and organic rich shales. Tremendous gas production from these reservoirs has transformed today's energy landscape. To effectively optimize the hydrocarbon production from these ultra-tight formations, it is essential to study and model the fluid transport and storage sealed in multiscale pore structure of these formations, i.e. micro-, meso- and macro-pores. In shale gas reservoirs, Kerogen, the finely dispersed organic nano-porous material with an average pore size of less than 10 nm holds bulk of the total gas in place (GIP) in an adsorbed state. The molecular level interactions between fluid-fluid and fluid-solid organic pore walls govern the transport and storage in these organic nano-pores. Among different methods used to model gas dynamics in organic nano-pores such as the multi-continuum, molecular dynamics and Monte Carlo, the lattice Boltzmann method (LBM) is a more effective method with much less computational cost relative to other techniques. This is due to the applicability of this technique in wide range of flow regimes and ease of handling complex boundary conditions such as incorporation of the molecular interactions in porous media.

The objective of this research is to develop a two-dimensional LBM of organic rich shales that can be used to quantify the effect of organic pore wall confinement on non-ideal gas flow and storage in organic nano-pores of the shale reservoirs. This method incorporates the involvement of molecular forces between fluid particles such as, adsorptive and cohesive forces. Using the Langmuir-slip boundary condition at capillary walls, slippage of free gas molecules and surface transport of adsorbed molecules are studied. This effect is investigated in a large range of Knudsen numbers from continuum flow to transition flow regime with varying capillary width sizes from 100 nm to 5 nm.

Simulation results concentrates on the molecular phenomena like- adsorptive/cohesive forces, and the kinetic energy of the fluid molecules at different pressures, and reservoir temperatures. The LBM model results displays a clear indication that the gas transport in the capillary tube is depends on the pore width size. A critical Knudsen number exists with changing reservoir conditions, where the anticipated fluid velocity profile in organic nano-pores alters showing higher flow rate as capillary widths reduces due to the underlying effect of molecular phenomena of double slippage and wall confinement, introduced earlier by Fathi et al[1].

These results are compared with traditional continuum Hagen-Poiseuille law, Klinkenberg slip theory, and recent modified version of Klinkenberg slip flow equation. This work is not only important for the advancement of shale gas flow simulator, but also for organic rich shale characterization.

Acknowledgements

There has been numerous people who have walked by my side during different phases of my life, shaping the person I am today. They have guided me, steered me towards opportunities, and showed me the brighter side of every situation making me stronger and happier with each day. I would like to thank each and every one of them.

I am extremely grateful to my research advisor Dr. Ebrahim Fathi, without his constant guidance and motivation, this thesis would not have been possible. I remember the meetings with him after which I would be energized and impelled to work harder. I am greatly indebted to Dr. Fathi for all the encouragement and financial help I received from him.

I want to thank my committee members Dr. Ali Takbiri Borujeni and Dr. Fatemeh Belyadi for sharing their knowledge and giving fruitful advice to me. I am grateful to Dr. Samuel Ameri, Chairperson- Petroleum Engineering (WVU), and Dr. Radhey Sharma, Professor- Civil Engineering and Associate Vice President- Global Strategies and International Affairs (WVU), for showing incredible support in times of distress, and caring as family while I was away from my family. I am thankful to this amazing spirited lady Ms. Beverly Matheny, Admistrative Assistant- Petroleum Engineering (WVU) for loving and protecting me.

I would like to take this opportunity to acknowledge West Virginia University for providing me with great infrastructure, resources, and a learning environment.

A big thank you to my parents and siblings for believing in me and loving me unconditionally. Special thanks to my sister Ms. Snehal Gupta for being my first ever teacher since childhood. I always looked up to her for inspiring me to be better with each day. Without my friends- Chetan, Manish, Suvineeth, and Naren, it would have been a lonely place for me in Morgantown. They imbibed immense confidence in me and supported me at unaccountable instances. I want to extend my gratefulness to other fellow graduates for boosting my morale, and offering great help throughout my studies at WVU

Lastly, I would like to thank the universe for all the favorable circumstances, and letting me complete my thesis successfully.

Table of Contents

List of Figures

List of Tables

Nomenclature

a	Channel half width
c	Proportionality constant
C	Free gas density
C_1	First-order slip coefficient
C_2	Second-order slip coefficient
C_μ	Adsorbed gas density
$C_{\mu s}$	Maximum monolayer adsorption capacity
D_k	Tortuosity-corrected coefficient of molecular diffusion
D_s	Surface diffusion coefficient
e	Lattice Velocity
f	single-particle distribution function
f^{eq}	Equilibrium distribution function
f^{neq}	Non-equilibrium distribution function
F	Long range fluid interaction force
G	Interaction strength
G^*	Pressure gradient
H	Width of capillary tube
J_{ads}	Adsorbed-gas flux
J_{free}	Free-gas flux
K	Langmuir partition coefficient
Kn	Knudsen number
L	Length of capillary tube
m	Molecular mass
M	Molar mass/ Molecular weight of the gas
N_R	Avogadro number
P	Pore pressure
P_L	Langmuir pressure

r	Distance from the center of the capillary
r_0	Capillary Half-width
R	Universal Gas constant
t	Time
T	Reservoir temperature
U	Macroscopic velocity
$U_{g,slip}$	Velocity of gas which is one mean free path distance away from the wall i.e. slip velocity
U_{slip}	Slip Velocity
$\frac{U_{slip}}{U_o}$	Normalized Slip Velocity
U_{surf}	Local wall velocity due to the adsorbed-phase transport
U_W	Fluid velocity by the wall
V_a	Adsorbed gas volume
V_{amax}	Maximum monolayer adsorbed gas volume
x	Lattice space
z	Compressibility factor

Greek Symbols

α	Equilibrium Langmuir isotherm coefficient
k_B	Boltzmann constant
λ	Mean free path of gas molecules
μ	Gas dynamic viscosity
ν	Gas Kinematic viscosity
Ω	Collision Operator
ρ	Macroscopic fluid density
ρ_{ads}	Average adsorbed gas density
ρ_g	Gas density

ρ_0	Arbitrary constant
ψ	Interaction potential function
τ	Relaxation time
τ^*	Effective relaxation time
w	Weighing factor

Chapter 1 Introduction

Shale gas formations introduces the possibility to increase the total gas production by accessing the trapped natural gas within organic rich shale sedimentary rocks, comprising of organic porous material (kerogen), and inorganic matrix. The properties of shale gas like its composition, organic richness, structure of nano- pores, flow regime primarily determines the production and flow of natural gas. To effectively simulate the shale gas flow in shale, it is critical to understand the shale gas transport mechanisms in a kerogen pore. The kerogen pores generally extends between micropore ($h < 2nm$) and mesopore ($2 \leq h < 50\ nm$), having an average pore size of $10\ nm$ [2], h being the pore size. Table 1-1 presents the International Union of Pure and Applied Chemistry (IUPAC) categorization of pore diameters. Previous analysis on pore diameter estimation of organic-rich shales displays the existence of ultra-micropores, micropores, mesopores, and macropores.

Table 1-1: IUPAC categorization of pore diameter

Ultra-micropore	$\leq 0.7nm$
Micropore	$> 0.7nm\ and\ < 2nm$
Mesopore	$> 2nm\ and\ < 50nm$
Macropore	$\geq 50nm$

In recent years, to study the micro-scale flow characteristics of shale gas, laboratory measurement techniques and numerical simulation methods have been incorporated. To begin with, a dimensionless parameter (Knudsen Number, $Kn = \lambda/h$) defined as the ratio of mean free path of gas molecules (λ) to hydraulic pore diameter of conduit (h). This number is used to differentiate different gas flow reigns, namely – Continuum flow ($Kn \leq 0.001$), Slip flow ($0.001 < Kn \leq 0.1$), Transition flow ($0.1 < Kn \leq 10$), and Free molecule flow ($Kn > 10$) [3]. The mean free path is commonly defined as the average distance travelled by a gas molecule before colliding with another gas molecule. The continuum flow is illustrated by the Navier-Stokes equations, dominated by the viscosity effects; the slip flow is characterized by the inclusion of a

slip parameter to the Navier-Stokes equations; the transition flow is described by molecular simulations, such as Direct Simulation Monte Carlo (DSMC); the free molecular flow is depicted as the flow where the molecular collisions are ignored, and is represented by the Boltzmann equation.

At thermodynamic equilibrium, due to strong pore wall influence, a part of the gas molecules adhere to the internal surface of the pore wall having restricted mobility and low kinetic energy called the adsorbed layer as shown in Figure 1-1. Adjoining this layer is the phase-transition layer called Knudsen layer where molecules possess some kinetic energy to continually get adsorbed and desorbed with little influence from the walls. The remaining of the gas molecules are attributed as the free-gas molecules having no wall influence taking the central zone of the pore. The free-gas molecules interact within themselves and with the adjacent Knudsen layer molecules. The free-gas molecular density is the same as the bulk fluid density without the pore walls.

In tight porous media, like shale, the transport phenomena of gas molecules at constant reservoir temperature depends on the matrix pore size and the reservoir pressure. At the average kerogen pore size of 10 nm, majority of the gas is trapped in adsorbed state. At such conditions, the mean free path of gas molecules becomes comparable to the organic pore size itself. This results in intense molecular interaction of the free-gas molecules with the Knudsen and adsorbed layer molecules. When the thermodynamic equilibrium is disturbed externally (change in molecular flux), these interactions lead to molecular streaming (slippage & hopping mechanism) in the organic pore. This effect produces non-zero wall velocity additional to the free-gas mass transport showing deviations from Darcy's law. When external flux is applied, some molecules in adsorbed layer and Knudsen layer overcome the local interactions with the wall to initiate a hopping mechanism, also known as surface diffusion. Surface diffusion becomes predominant in nano pores by increasing the kinetic energy by the pore walls.

During the studies of Kang et al. (2011) [4], it was found that the gas flowing in kerogen pores of shale matrix is non-ideal and is generally in the slip flow or transition flow regimes, under shale gas reservoir conditions. The gas transport in kerogen nano pores involves strong molecular interactions between gas and kerogen leading to adsorption/desorption phenomena. The adsorbed-gas molecules move along the pore wall due to surface diffusion, which has been confirmed lately [4] as shown in Figure 1-1. For pore size less than 2 nm, it is stated that the role of surface diffusion

contributing to total mass transfer could be significant [5]. Therefore, from above explanation of fluid flow in smaller pores, the assumption of Darcy flow becomes invalid and a new approach is essential to incorporate non-Darcy free-gas mass transport.

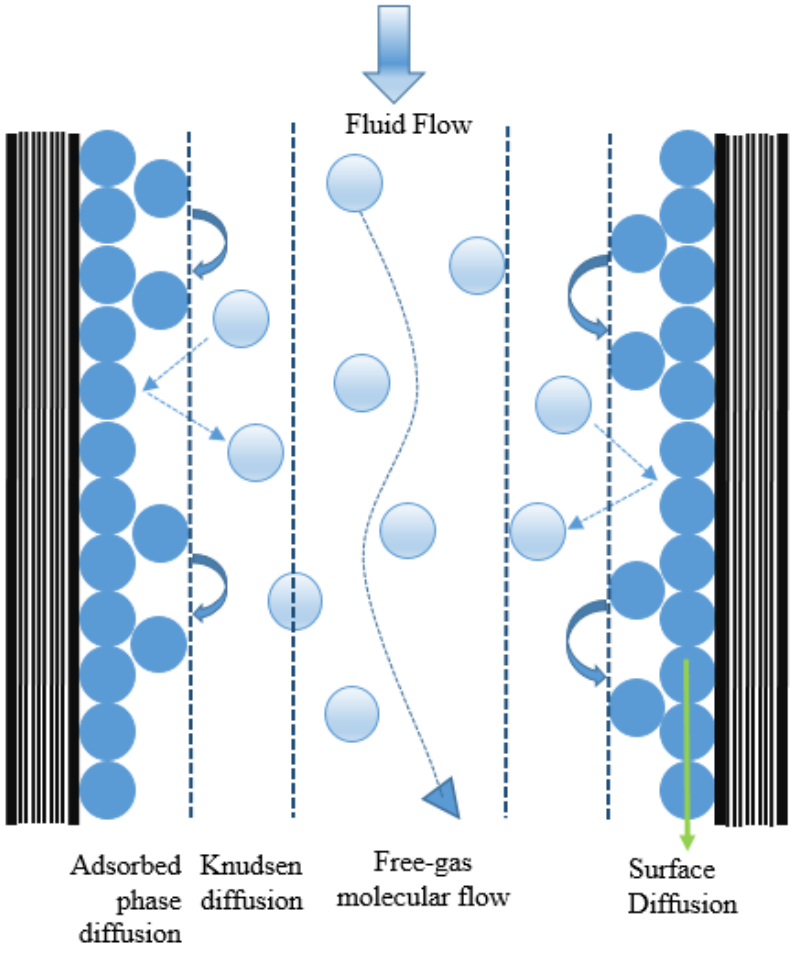

Figure 1-1: Schematic picture of shale gas flow in kerogen pore

The shale gas simulations are classified into three categories- continuum approach, molecular dynamics approach, and mesoscopic approach. The macro-level simulation methods (continuum method) include the discretization of Navier-Stokes equations using either of finite difference, finite element, or finite volume procedures which does not hold good or rather breaks down and is invalid for fluid flow in organic nano-pores of the shale gas reservoirs. The molecular dynamics method requires high computational power and high storage capacity of computers, and thus it is practically not advisable for the simulation of complex flow field, nano-scale porous network of shale. The direct simulation Monte Carlo method also requires high computational costs and becomes turbulent with small Mach numbers, thus not advisable. Therefore, unlike the

Continuum approach, Molecular Dynamics approach, and Direct Simulation Monte Carlo (DSMC) approaches, Lattice Boltzmann model (LBM) provides an efficient approach for simulating gas flow in kerogen pores. LBM is suitable for simulation of complex flow of shale gas having multi fluid phase interfaces. During the last few years, the Lattice Boltzmann method (LBM) is used as a prime alternative numerical approach for modeling physical phenomena in fluid flows combining microscopic and macroscopic physical mechanisms. LBM's ability to integrate and merge the complex solid boundaries have enabled us to simulate realistic porous media, which presents as one of the most appealing factors for its wide acceptability. LBM is also used to estimate the apparent matrix permeability as it is simple, easy to program and highly scalable. It is also suggested that LBM can offer probability for future research to simulate gas flow in major pore portions of shale gas reservoirs, ranging from continuum to slip flow regimes [6].

According to the theory of phase behavior equilibrium of gases, the measurement of gas in a bulk system or in a tube is treated likewise when a constant pressure and constant temperature is applied to a system of same volume (different shape), that ignores the container wall effects. But as the system volume shrinks to mesopore and micropore scales the phase equilibrium becomes pore size dependent where the wall confinement effect changes the hydrodynamic behavior of fluid significantly [7].

1.1. Problem Statement

In spite of many advancements in LB models to study the gas slippage and wall confinement effects, there are always controversial arguments between each due to the inadequacy of thorough knowledge of surface properties and surface interaction potentials.

In the bulk system, the ideal gas equation of state $PV = nRT$ does not hold good and it needs to be corrected, which is when the compressibility non-ideal gas equation of state $PV = znRT$ is introduced. Although the incorporation of z factor corrects for non-ideal gas behavior, it does not account for pore size or the wall confinement effect. To show the impact of container (in this case pore size) on non-ideal gas dynamics, different pore sizes were considered and LBM simulation of gas transport in organic rich shale nano-capillaries are performed to quantify the gas slippage and wall confinement effect.

The fluid flow in organic pores is essentially single phase, so in this study, a two-dimensional LBM is employed to evaluate the velocity profile of a single component methane gas flowing through an organic nano-capillary tube. This research solves the Boltzmann equation Eq. (2-2) using the velocity Eq. (2-3), the BGK collision operator Eq. (2-6). To determine the equilibrium distribution functions Eq. (2-29), the macroscopic fluid density and macroscopic velocity equations Eq. (2-4) and Eq.(2-5) are adopted. An effective relaxation time Eq. (2-25) is defined to correct from continuum flow to Knudsen flow regime. The periodic boundary conditions are adopted for the capillary inlet and outlet, making the system closed. The modified Langmuir slip boundary condition developed earlier by Fathi et al., 2012 [8] is incorporated to picture the adsorbed-phase transport, wall confinement, and gas slippage phenomenon. The pressure-density curve determined using the non-ideal equation of state provides the interaction potential function which are used in this study accounting interaction forces between the gas particles in the LBM formulation.

1.2. Objective

The objective of this research is to develop a two-dimensional LBM of organic rich shales that can be used to quantify the effect of organic pore wall confinement on non-ideal gas flow and storage in organic nano-pores of the shale reservoirs. This effect is investigated in a large range of Knudsen numbers from continuum flow to transition flow regime with varying capillary width sizes from 100 nm to 5 nm.

Through this study it was found that the capillary length does not affect the velocity profile, it is shown by varying the length: width size ratios between 2:1 and 10:1. Studies show that the 20nm width size is critical at high pore pressures of 1623 psi and 77F temperature corresponding to Knudsen number $5.51E-3$ where the velocity at the center of the capillary and at the walls increases with decreasing the pore width which contradicts with Poiseuille flow, original Klinkenberg and modified Klinkenberg theories developed earlier. This observation suggests that the momentum of fluid particles bouncing back from the capillary walls influences the bulk fluid flow resulting in higher velocities at the center and wall.

Using the LBM formulation, the molecular phenomena like- adsorptive/cohesive forces, and the kinetic energy of the fluid molecules at different pressures, and reservoir temperatures are studied.

These results are then compared with traditional continuum Hagen-Poiseuille flow velocity profile, Klinkenberg and modified Klinkenberg theories.

1.3. Chapter Review

This thesis includes four chapters. The chapter one presents the background of shale gas formation, its production and simulation methods. Here the purpose of study and statement of problem, and its significance was defined. Chapter two introduces the literature review where the conceptual and theoretical physics involved is explained, along with previous work done by researchers in the field of lattice Boltzmann simulations. Chapter three proposes the research methodology, formulation based on hypotheses. Chapter four represents results and discussions based on the research design incorporated. All the findings of each case is explained and concluded with suggestions for future research work.

Chapter 2 Literature Review

This chapter presents the evolution of lattice gas models, transition from Boltzmann's original concepts to lattice Boltzmann models, fundamentals of LBM, basic concepts and equations to define the model. Background knowledge on lattice arrangements, particle movement, correction factors, and boundary conditions are also described.

2.1. Background

Lattice Boltzmann method was first derived from lattice gas automata, an algorithm which defines an entities interaction with its neighbors based on its placement on a grid in space. One dimensional cellular automata are considered to be the simplest form, where the entity recognizes its own states (0 and 1, for example) and two of its adjacent neighbors existing on a line. In this case, the possible rules for updating the central automaton are 256 ($n_s^{n_n}$) entries, where n_s is the number of states for a neighborhood of n_n automata. Generally, the update rule symbolically can be represented as $a_i' = \phi(a_{i-1}, a_i, a_{i+1})$ where a_i' is the updated state, ϕ is one of 256 functions, and a_{i-1}, a_i, a_{i+1} are the initial states of the automaton itself and its left and right neighbors respectively.

The FHP model, named after Frisch, Hasslacher, and Pomeau was the first lattice gas model able to simulate the 2-dimensional Navier-Stokes equations apart from simulating the diffusion and reaction-diffusion equation having hexagonal symmetry. This model is constructed on an equilateral triangular lattice that provides an isotropic solution. Each of the lattice points are separated by 1 lattice unit (lu) and each particle have a speed of 1 lu/timestep ($lu\ ts^{-1}$). Every lattice point may have up to 6 particles based on the possible velocities defined by particle speed Eq. (2-1) and six possible directions.

$$e_a = \left(cos\frac{\pi a}{3}, sin\ \frac{\pi a}{3}\right) \tag{2-1}$$

Where a = 1, 2, 3, 4, 5, 6, and e_a is the velocity vector pointing from the origin (0, 0) to the Cartesian coordinate (cos πa/3, sin πa/3).

Rothman and Zaleski (1997) illustrated the FHP lattice model indicating the presence (1) or absence (0) of particles that move from position x to a neighboring position $x + e_a$ as shown in Figure 2-1 [9].

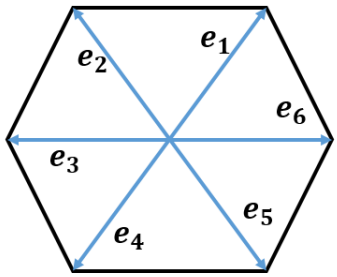

Figure 2-1: FHP Lattice Model Unit Velocity Vectors

2.2. LBM Framework and Equations

The fundamental concept of Boltzmann is to link microscale and macroscale to mesoscale by considering the behavior of a group of particles as a unit unlike considering each particle's behavior. The characteristic of the set of particles as a unit is defined as a distribution function. This method was evolved to unblock some of the incapacities of lattice gas automaton, which eradicates the statistical noise issue and occurrence of extra terms in the upscale Navier-Stokes equations while preserving its local kinetic form. According to Maxwell, determining the velocity and position of particles at every time instant is irrelevant. Instead, the distribution function is crucial in portraying the effect of molecules within a definite range and at a time instant.

2.2.1. Basic Lattice Boltzmann scheme

The general form of the lattice Boltzmann equation includes a lattice pattern, a local equilibrium distribution function apart from the lattice Boltzmann equation itself, presented as Eq. (2-2).

$$f_a(x + e_a\Delta x\ .\ t + \Delta t) = f_a(x, t) + \Omega(\mathrm{f_a}) \qquad (2\text{-}2)$$

Where, f_a is the distribution function of particles, travelling with velocity e_a at directional index node $a = 0,1,\ldots..\ N;\ x$ and t are lattice space and lattice time dimensions, respectively; Δt is the lattice timestep (ts); $\Omega(\mathrm{f_a})$ is the collision operator, representing the changes in particle distribution as a result of particle collision.

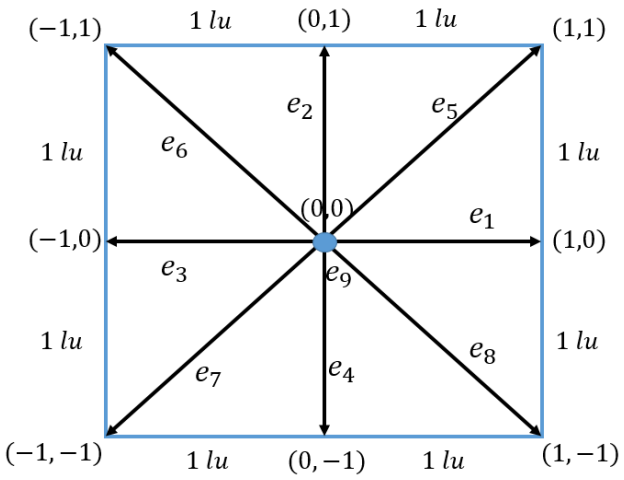

Figure 2-2: D2Q9 LBM Lattice model depicting x, y velocity components in nine directions

The transition from Boltzmann's original concept to Lattice Boltzmann models not only reduces the possibility of particle special positions but also discretizes microscopic momenta into time and space from a continuum. In LBM equation, the particle positions and their velocity directions are restricted to the number of nodes in each lattice. An extensively popular two-dimensional LBM model scheme proposed by Qian et al. (1992)[10] demonstrates a single particle mass having eight directions and three magnitudes. This model is known as D2Q9 as it is two-dimensional and involve nine velocities. The 2D LBM Cartesian lattice with the velocities (e_a) moving one lattice unit in nine directions, and its x- and y- velocity components (-1, 0, or 1) having directional index $a = 0,1, \dots ,8$ is shown in Figure 2-2. The particle at position '0' is at rest with velocity ($e_0 = 0$). The fundamental measure of units in LBM models for length and time are lattice units (lu) and time steps (ts) respectively. The magnitude of velocity of $e_1\ to\ e_4$ is 1 $luts^{-1}$ and of $e_5\ to\ e_8$ is $\sqrt{2}\ luts^{-1}$, and typically defined in Eq. (2-3).

$$e_a = \begin{cases} (0,0) & a = 0 \\ \left[Cos\dfrac{(a-1)\pi}{4}, sin\dfrac{(a-1)\pi}{4}\right] & a = 1,2,3,4 \\ \sqrt{2}\left[Cos\dfrac{(a-1)\pi}{4}, sin\dfrac{(a-1)\pi}{4}\right] & a = 5,6,7,8 \end{cases} \qquad (2\text{-}3)$$

Employing the macroscopic fluid density and macroscopic velocity equations Eq. (2-4) and Eq.(2-5) in their discreet form, the continuum fluid motion is formed for LBM. The macroscopic fluid density is formed for nine discrete direction-specific fluid densities f_a as-

$$\rho = \sum_{a=0}^{8} f_a \tag{2-4}$$

Where, f is the single-particle distribution function representing a frequency of occurrences on a histogram for nine discrete 'bins'[9].

On a similar note, the macroscopic velocity U is defined as average of the microscopic velocities e_a over directional densities f_a.

$$U = \frac{1}{\rho}\sum_{a=0}^{8} f_a e_a \tag{2-5}$$

2.2.2. Collision Operators

Collision operators specifies the collision between particles at each location on the lattice which contributes to the change in distribution functions. In this section some general collision operators used for micro-gaseous flows are demonstrated.

2.2.2.1. Single Relaxation Time - BGK Model

The classical LBM involves the Bhatnagar-Gross-Krook (BGK) (Bhatnagar et al. 1954) [11] collision operator which is an efficient simplification operator, where the distribution functions are relaxed explicitly. The BGK collision operator is derived by assuming $\Omega_a\left(f_a^{eq}\right)$ equal to zero, built on linearizing the collision operator at the equilibrium state (omitting higher order terms), therefore the BGK collision operator is retrieve as Eq. (2-6)

$$\Omega_{\mathrm{a}} = \frac{1}{\tau}\left[-f_a(x,t) + f_a^{eq}(x,t)\right] \tag{2-6}$$

Where, τ is the relaxation time, and f^{eq} is the equilibrium distribution function.

Although the BGK collision operator reproduces most of the hydrodynamic behavior, it is easy to implement and is reliable[12][9]; it still has issues relating to numerical instability and inaccuracy at low viscosities[13][14].

2.2.2.2. Two Relaxation Time

The two relaxation time (TRT) collision operator scheme was established by Ginzburg [15], where the distribution function is divided into symmetric f_a^s and anti-symmetric f_a^a components, relating to the shear viscosity and energy fluxes respectively, defined in Eq. (2-7) and Eq.(2-8).

$$f_a^s = \frac{1}{2}(f_a + f_{-a}) \tag{2-7}$$

$$f_a^a = \frac{1}{2}(f_a - f_{-a}) \tag{2-8}$$

By adding and subtracting the above two equations, we obtain the distribution functions f_a and f_{-a} (Eq. (2-9)), where f_{-a} is moving opposite to distribution function f_a. The symmetric and anti-symmetric distribution functions can also be defined as Eq. (2-10).

$$f_a = f_a^a + f_a^s \quad ; \quad f_{-a} = f_a^a - f_a^s \tag{2-9}$$

$$f_a^a = f_{-a}^a \quad ; \quad f_a^s = -f_{-a}^s \tag{2-10}$$

The collision operator in the TRT scheme is represented in its basic form as Eq. (2-11).

$$\Omega_{\mathrm{a}} = -\frac{1}{\tau_s}\left(f_a^s(x,t) - f_a^{seq}\right) - \frac{1}{\tau_a}\left(f_a^a(x,t) - f_a^{aeq}\right) \tag{2-11}$$

Eq. (2-11) can also be written as Eq. (2-12).

$$\Omega_{\mathrm{a}} = -\frac{1}{2}(\omega_s + \omega_a) f_a^{seq} - \frac{1}{2}(\omega_s - \omega_a) f_a^{aeq} \tag{2-12}$$

Where $\omega_s = 1/\tau_s$ and $\omega_a = 1/\tau_a$. The symmetric and anti-symmetric relaxation coefficients for D2Q9 model are defined as Eq. (2-13) [12].

$$\omega_s = \frac{1}{3\nu + 0.5}$$
$$\omega_a = \frac{8(2-\omega_s)}{8-\omega_s} \tag{2-13}$$

The following set of equations represent solving for Eq. (2-12), by substituting Eq. (2-7), Eq.(2-8), and Eq. (2-10).

$$\Omega_a = -\frac{1}{2}\omega_s\left(f_a^{seq} + f_a^{aeq}\right) - \frac{1}{2}\omega_a\left(f_a^{seq} - f_a^{aeq}\right)$$
$$\Omega_a = -\frac{1}{4}\omega_s\left(f_a^{eq} + f_{-a}^{eq} + f_a^{eq} - f_{-a}^{eq}\right) - \frac{1}{4}\omega_a\left(f_a^{eq} + f_{-a}^{eq} - f_a^{eq} + f_{-a}^{eq}\right) \tag{2-14}$$
$$\Omega_a = -\frac{1}{2}\omega_s\left(f_a^{eq}\right) - \frac{1}{4}\omega_a\left(f_a^{eq} + f_{-a}^{eq} - f_{-a}^{eq} + f_a^{eq}\right)$$

The revised collision operator for TRT is developed as Eq. (2-15).

$$\Omega_a = -\frac{1}{2}\omega_s\left(f_a^{eq}\right) - \frac{1}{2}\omega_a\left(f_a^{eq}\right) \tag{2-15}$$

It is to be noted that, the two-relaxation-time reduces to single-relaxation-time scheme if $\tau_s = \tau_a$.

2.2.2.3. *Multiple Relaxation Time*

The multiple relaxation time (MRT) collision operator is an improved form of the BGK collision operator, where the distribution functions are presented in a system which is based on moments, and each of these moments are relaxed with its specific relaxation times. This method of individually relaxing moments incorporates the physical effects caused on discrete moments at unique time scales through their equivalent relaxation times which adds more degree of freedom for simulating collision process and helps in overcoming the BGK collision operator drawbacks of increased numerical stability and accuracy.

The MRT scheme collision operator is presented in the momentum space as Eq. (2-16) [16][12].

$$\Omega_a = -M^{-1}S[m(x,t) - m^{eq}(x,t)] \tag{2-16}$$

Where $m(x,t)$ and m^{eq} are moment vectors defined as $m = (m_0, m_1, m_2, \ldots m_n)^T$ and S is the non-negative relaxation diagonal matrix.

The relation between velocity distribution functions and moment vectors is defined using a linear transformation as- $m = Mf$ and $f = M^{-1}m$

For D2Q9, the orthogonal transform matrix M and its inverse matrix is represented in Eq. (2-17) and Eq. (2-18).

$$M = \begin{bmatrix} 1 & 1 & 1 & 1 & 1 & 1 & 1 & 1 & 1 \\ -4 & -1 & -1 & -1 & -1 & 2 & 2 & 2 & 2 \\ 4 & -2 & -2 & -2 & -2 & 1 & 1 & 1 & 1 \\ 0 & 1 & 0 & -1 & 0 & 1 & -1 & -1 & 1 \\ 0 & -2 & 0 & 2 & 0 & 1 & -1 & -1 & 1 \\ 0 & 0 & 1 & 0 & -1 & 1 & 1 & -1 & -1 \\ 0 & 0 & -2 & 0 & 2 & 1 & 1 & -1 & -1 \\ 0 & 1 & -1 & 1 & -1 & 0 & 0 & 0 & 0 \\ 0 & 0 & 0 & 0 & 0 & 1 & -1 & 1 & -1 \end{bmatrix} \tag{2-17}$$

$$M^{-1} = a\begin{bmatrix} 4 & -4 & 4 & 0 & 0 & 0 & 0 & 0 & 0 \\ 4 & -1 & -2 & 6 & -6 & 0 & 0 & 9 & 0 \\ 4 & -1 & -2 & 0 & 0 & 6 & -6 & -9 & 0 \\ 4 & -1 & -2 & -6 & 6 & 0 & 0 & 9 & 0 \\ 4 & -1 & -2 & 0 & 0 & -6 & 6 & -9 & 0 \\ 4 & 2 & 1 & 6 & 3 & 6 & 3 & 0 & 9 \\ 4 & 2 & 1 & -6 & -3 & 6 & 3 & 0 & -9 \\ 4 & 2 & 1 & -6 & -3 & -6 & -3 & 0 & 9 \\ 4 & 2 & 1 & 6 & 3 & -6 & -3 & 0 & -9 \end{bmatrix} \tag{2-18}$$

Where $a = 1/36$, the moment vector m and equilibrium of the moment vector m^{eq} are represented in Eq. (2-19) and Eq. (2-20).

$$m = \left(\rho, e, \epsilon, j_x, q_x, j_y, q_y, p_{xx}, p_{xy}\right)^T \tag{2-19}$$

$$\begin{aligned} m_0^{eq} &= \rho \\ m_1^{eq} &= -2\rho + 3\left(j_x^2 + j_y^2\right) \\ m_2^{eq} &= \rho - 3\left(j_x^2 + j_y^2\right) \\ m_3^{eq} &= j_x \\ m_4^{eq} &= -j_y \\ m_5^{eq} &= j_x \\ m_6^{eq} &= -j_y \\ m_7^{eq} &= \left(j_x^2 - j_y^2\right) \end{aligned} \tag{2-20}$$

$$m_8^{eq} = j_x j_y$$

These moments have a physical significance, where ρ is the density, e is the energy mode, ϵ is associated to energy squares, (j_x, j_y) are the x, y components of the momentum represented by Eq. (2-21), (q_x, q_y) are related to x, y components of the energy fluxes, (p_{xx}, p_{xy}) are linked to the diagonal and off-diagonal components of the stress tensors.

$$j_x = \rho u_x = \sum_{a=0}^{8} f_a e_{ax}$$
$$j_y = \rho u_y = \sum_{a=0}^{8} f_a e_{ay} \quad (2\text{-}21)$$

The diagonal matrix S, is represented as Eq. (2-22), which can also be written as Eq. (2-23).

$$S = \begin{bmatrix} s_0 & 0 & 0 & 0 & 0 & 0 & 0 & 0 & 0 \\ 0 & s_1 & 0 & 0 & 0 & 0 & 0 & 0 & 0 \\ 0 & 0 & s_3 & 0 & 0 & 0 & 0 & 0 & 0 \\ 0 & 0 & 0 & s_4 & 0 & 0 & 0 & 0 & 0 \\ 0 & 0 & 0 & 0 & s_5 & 0 & 0 & 0 & 0 \\ 0 & 0 & 0 & 0 & 0 & s_6 & 0 & 0 & 0 \\ 0 & 0 & 0 & 0 & 0 & 0 & s_7 & 0 & 0 \\ 0 & 0 & 0 & 0 & 0 & 0 & 0 & s_8 & 0 \\ 0 & 0 & 0 & 0 & 0 & 0 & 0 & 0 & s_9 \end{bmatrix} \quad (2\text{-}22)$$

$$S = diag(1.0, 1.4, 1.4, s3, 1.2, s5, 1.2, s7, s8 \quad (2\text{-}23)$$

Where $s7 = s8 = 2/(1 + 6v)$, $s3$ and $s5$ are fixed to 1.0 [12].

The MRT scheme reduces to BGK if the diagonal relaxation matrix S is set to $1/\tau$, and reduced to TRT if the even non-conserved relaxation rate moments are set to $1/\tau$ and odd relaxation rate moments are set to $\left[8 \times \frac{2\tau-1}{8\tau-1}\right]$ [14][12].

2.3. Correction from continuum flow to Knudsen flow

For incompressible fluids, $\tau -$ relaxation time, is assumed to be constant which generates second order truncation error in the lattice Boltzmann equation. However, this error is entirely absorbed into kinematic viscosity ν for isothermal LBM models [17].

$$\nu = (\tau - 0.5)RT \tag{2-24}$$

where R is the universal gas constant and T is the temperature. For D2Q9, value of RT is taken as 1/3. The above equation characterizes the relationship between relaxation time and kinematic viscosity in continuum flow, where the flow is controlled by Reynold's number. But for the flow transport with large Knudsen numbers, the flow is controlled by Knudsen number and thus the relaxation time will have to be corrected [18], where the effective (new) relaxation time is a function of Knudsen number. The effective relaxation time clearly depicts the wall effect, showing a macroscopic mean slip velocity at the wall.

$$\tau^* = \tau\psi(Kn) \tag{2-25}$$

$$\psi(Kn) = \frac{2}{\pi}\arctan(\sqrt{2}\,Kn^{-3/4}) \tag{2-26}$$

$$Kn = \frac{\nu}{H}\sqrt{\frac{\pi}{2RT}} \tag{2-27}$$

2.4. Streaming and Collision

The development of lattice gas model progresses in two steps occurring with each time step. The first step is streaming step, also known as propagation or hopping where the particles move to new lattice sites with respect to their preceding positions and velocities. The second is collision step which according to the collision rules, the particles approaching a node collide and changes its velocity direction, dispersing to new lattice sites according to the collision operator Ω.

The distribution function f_a is used to define the streaming and collision of particles in the lattice, by substituting the SRT collision operator Eq. (2-6) in the lattice Boltzmann equation Eq. (2-2) to obtain Eq. (2-28), representing the basic lattice Boltzmann equation.

$$f_a(x + e_a\Delta x, t + \Delta t) = f_a(x, t) - \frac{\left[f_a(x, t) - f_a^{eq}(x, t)\right]}{\tau} \quad (2\text{-}28)$$

Where $f_a(x + e_a\Delta t, t + \Delta t) = f_a(x, t)$ is the streaming part, $\left[f_a(x, t) - f_a^{eq}(x, t)\right]/\tau$ is the collision part, f_a^{eq} is the local equilibrium distribution function, τ is the relaxation time defined as the elementary time of collision.

2.4.1. Streaming

In streaming, the direction- specific densities f_a moves to its nearest neighbor lattice nodes. Figure 2-2 denotes the neighboring nodes relative to the point from which the directional densities are streamed. The Cartesian coordinates of the simplest LBM lattice model, where $ip, in, jp, and\ jn$ are calculated at every timestep is shown in Figure 2-3. This pattern of neighbor referencing was designed by Louis Colonna-Romano.

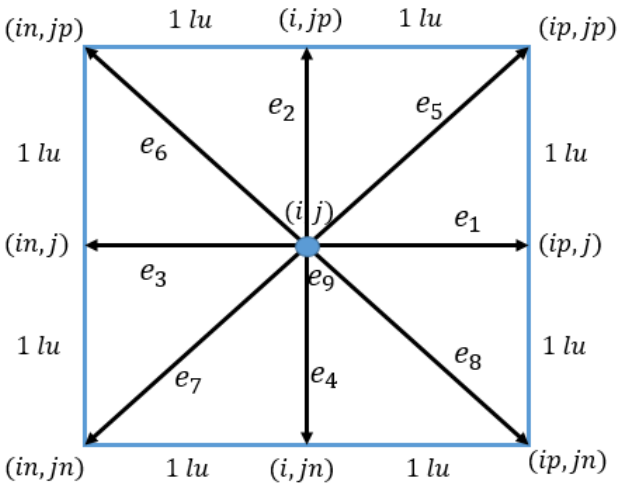

Figure 2-3: 2D LBM scheme following Louis Colonna-Romano neighbor referencing

2.4.2. Collision

According to the classical FHP model, the concept of collision can be defined as having zero net momentum during a head-on collision between particles. The elementary form of FHP model acknowledges only two- body and three-body collisions associating two and three particles respectively. The most important factors of the lattice gas to allow simulate the Navier-Stokes

equations are the conservation of mass and momentum. In this model, the colliding particles are present at the center of the hexagon before and after the collision step, the particle velocity vectors can be understood from Figure 2-4.

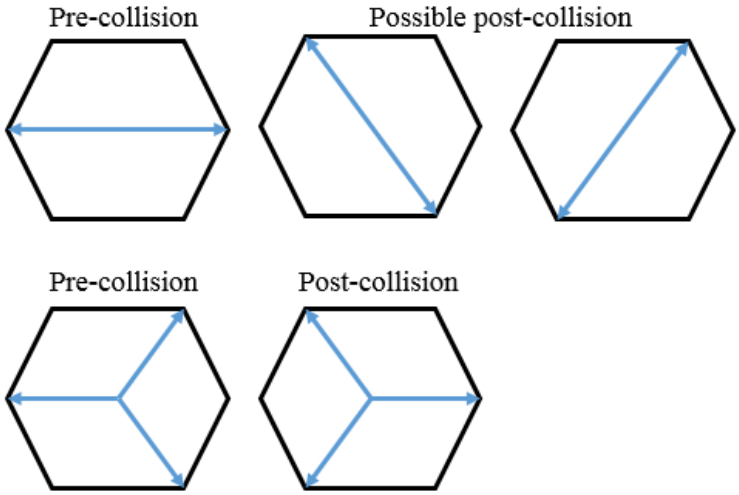

Figure 2-4: FHP Model showing head-on collision of 2- and 3- particles having zero net momentum

In presence of a solid boundary the collision and streaming steps are separated because the particle bounces back and collides with another particle. Collision of fluid particles is commonly denoted as relaxation towards local equilibrium and the equilibrium distribution function f_a^{eq} for D2Q9 model derived by Qian et al. (1992) [10] is defined in Eq. (2-29).

$$f_a^{eq}(x) = w_a \rho(x) \left[1 + 3\,\frac{e_a u}{c^2} + \frac{9}{2}\frac{(e_a u)^2}{c^4} - \frac{3}{2}\frac{u^2}{c^2} \right] \tag{2-29}$$

Where, the weights for D2Q9 model are $w_a = 4/9$ for particles at rest ($a = 0$); $w_a = 1/9$ for ($a = 1,2,3,4$); $w_a = 1/36$ for ($a = 5,6,7,8$); c is speed on lattice in the simplest form ($1\ luts^{-1}$), otherwise can also be described as lattice size Δx over lattice timestep Δt.

2.5. Lattice Arrangements

At every node in a LBM lattice domain, there exists a set of particles. While these particles stream or collide with the neighboring nodes, its direction and linkage depends on the lattice arrangement.

Generally, the dimension of the problem and the linkages is defined as $DnQm$, where n depicts the dimension (Eg.1-D, 2-D and 3-D) and m depicts the number of linkages.

2.5.1. One-Dimensional

There are three regular 1-D lattice arrangements, known as D1Q2, D1Q3 and D1Q5 represented in a work by Mohammad 1998, [12]. At the lattice speed, the particle stream move from the central node to neighboring nodes. For D1Q2 arrangement, the weighting factors are $\frac{1}{2}$ each for f_1 and f_2, and the speed of sound in lattice units is $1/\sqrt{2}$. For D1Q3 arrangement, one particle is at the central node, and the other two particles stream to either of its left or right node. The weighting factors are $4/6, 1/6, \& 1/6$ for $f_0, f_1 \,\&\, f_2$ respectively, and the speed of sound in lattice units is $1/\sqrt{3}$. For D1Q5 arrangement, the weighting factors are $\frac{6}{12}, \frac{2}{12}, \frac{2}{12}, \frac{1}{12}, \frac{1}{12}$ for f_0, f_1, f_2, f_3, f_4 respectively, and the speed of sound in lattice units is $1/\sqrt{3}$.

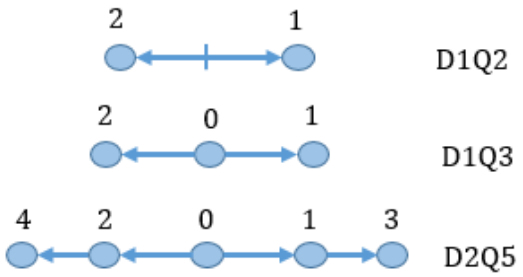

Figure 2-5: One-Dimensional lattice arrangement models

2.5.2. Two-Dimensional

The 2-D lattice arrangement models are D2Q4, D2Q5 and D2Q9. The difference between D2Q4 and D2Q5 is that both have four velocity vectors emerging from the central node, having no particle existing at the central node in D2Q4, and a particle existing at the central node in D2Q5 with zero speed, as shown in Figure 2-6. For D2Q4, the weighting factors are $\frac{1}{4}$ each for f_1, f_2, f_3, f_4 directions. For D2Q5, the weighting factors are $\frac{2}{6}, \frac{1}{6}, \frac{1}{6}, \frac{1}{6}, \frac{1}{6}$ for f_0, f_1, f_2, f_3, f_4 respectively.

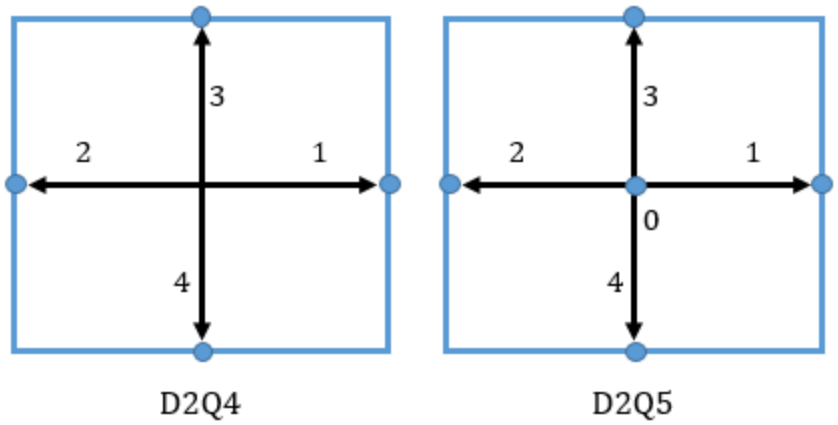

Figure 2-6: Two-Dimensional D2Q4 and D2Q5 lattice arrangement models

The D2Q9 model is a highly accepted two-dimensional model to solve fluid flow problems depicted in Figure 2-7. Its nine velocity vectors and weighing factors are defined in the earlier section of this chapter Eq. (2-3) and Eq. (2-29).

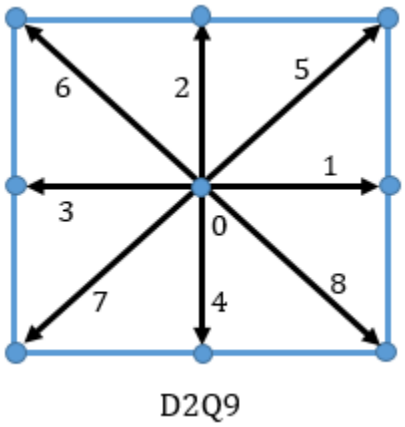

Figure 2-7: Two-Dimensional D2Q9 lattice arrangement model

2.5.3. Three-Dimensional

Typically, there are two 3D lattice arrangement models used, known as D3Q15 (most commonly used and shown in Figure 2-8) and D3Q19. For D3Q15 model, 15 velocity vectors emerge from a central node (f_0) having a zero speed. The weighting factors are $16/72$ for f_0 , $8/72$ for $f_1$to f_6 , and $1/72$ f_7 *to* f_{14}. For D3Q19 model, 19 velocity vectors emerge from a central node (f_0)

having a zero speed. The weighting factors are $12/36$ for f_0 , $2/36$ for f_1 to f_6 , and $1/36$ f_7 *to* f_{18}.

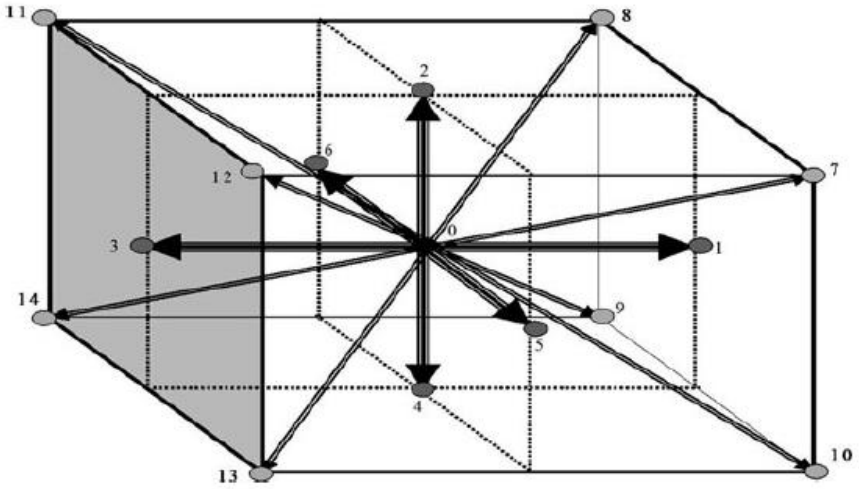

Figure 2-8: Three-Dimensional D3Q15 lattice arrangement model [12]

Suga[19] compiled the velocities e_a, speed of sound c_s, weighing factors ω_a in different directions for 2D/3D LBM based on the lattice arrangements, presented in Table 2-1.

Table 2-1-: Discrete velocity and weighing factor parameters for 2D/3D LBM models

Models	c_s^2/c^2	e_a/c	w_a
D2Q9	$1/3$	$(0,0)$	$4/9(a=0)$
		$(\pm1,0),(0,\pm1)$	$1/9(a=1-4)$
		$(\pm1,\pm1)$	$1/36(a=5-8)$
D2Q21	$2/3$	$(0,0)$	$91/324(a=0)$
		$(\pm1,0),(0,\pm1)$	$1/12(a=1-4)$
		$(\pm1,\pm1)$	$2/27(a=5-8)$
		$(\pm2,0),(0,\pm2)$	$7/360(a=9-12)$
		$(\pm2,\pm2)$	$1/432(a=13-16)$
		$(\pm3,0),(0,\pm3)$	$1/1620(a=17-20)$
D3Q19	$1/3$	$(0,0,0)$	$12/36(a=0)$
		$(\pm1,0,0),(0,\pm1,0),(0,0,\pm1)$	$2/36(a=1-6)$
		$(\pm1,\pm1,0),(\pm1,0,\pm1),(0,\pm1,\pm1)$	$1/36(a=7-18)$
		$(0,0,0)$	$1/12(a=0)$

D3Q39	2/3	$(\pm1,0,0),(0,\pm1,0),(0,0,\pm1)$	$1/12(a=1-6)$
		$(\pm1,\pm1,\pm1)$	$1/27(a=7-14)$
		$(\pm2,0,0),(0,\pm2,0),(0,0,\pm2)$	$2/135(a=15-20)$
		$(\pm2,\pm2,0),(\pm2,0,\pm2),(0,\pm2,\pm2)$	$1/432(a=21-32)$
		$(\pm3,0,0),(0,\pm3,0),(0,0,\pm3)$	$1/1620(a=33-38)$

2.6. Boundary Conditions

Boundary conditions play an essential role in determining the dynamics of a fluid flow. Many researchers have analyzed and studied the behavior of different boundary conditions for years (Ziegler 1993; Skordos 1993; Inamuro et al. 1995; Noble et al. 1995; Ginzbourg and d'Humieres 1996; Maier et al. 1996; Zou and He 1997; Fang et al. 1998; Verberg and Ladd 2000; Zhang et al. 2002; Ansumali and Karlin 2002; Chopard and Dupuis 2003). And after intense research, the following are some frequently used boundary conditions - periodic, bounceback and Zou and He (1997), constant pressure and constant velocity which will be discussed in this section.

2.6.1. Periodic Boundaries

In this boundary condition, the system turns out to be closed by having the opposite ends or edges attached. This is considered to be the simplest boundary condition type, and also sometimes recognized as the 'wrap-around' boundary. Periodic boundary condition is applied to the open end of a slit in the system.

2.6.2. Bounceback Boundaries

The 'bounce back' condition generally refers to the state of sending back the particle from where it originated. This condition is applied at the solid surface of the system, classified broadly into two types – solid-fluid interface, and the confined solids which are not in contact with the fluid, neglecting the inactive nodes during computation. A 'mid-plane' bounceback pattern might be used when the wall location is midway between the fluid and solid nodes, where the direction specific densities are temporarily stored inside the solids and re-emerge at a later time step[20].

2.6.3. Von Neumann (Flux) Boundaries

In the Von Neumann boundary condition, the flow (flux) is restrained at the boundary, where the macroscopic density/pressure and unknown directional densities are calculated. Post streaming, at

each lattice node, there are three directional densities which needs to be computed (Figure 2-9: Post Streaming Step- depicts the unknown direction-specific densities at a North Boundary) which face the system back from the boundary. This can be determined when an explicit velocity of $\boldsymbol{u_0} = \begin{pmatrix} u_0 \\ v_0 \end{pmatrix}$ is maintained at the lattice nodes.

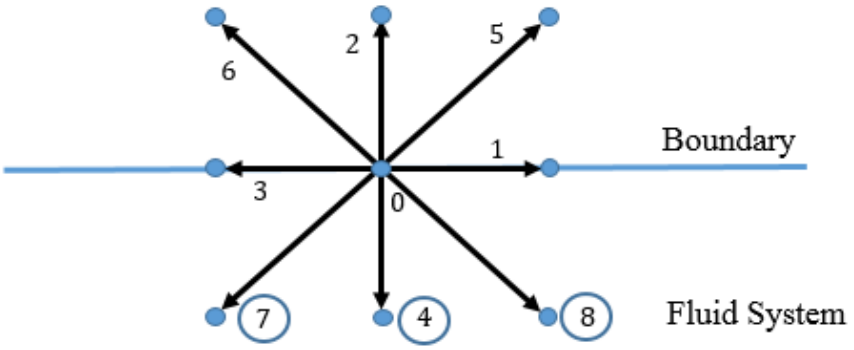

Figure 2-9: Post Streaming Step- depicts the unknown direction-specific densities at a North Boundary

Based on the assumption that bounceback is accomplished in the direction normal to the boundary, the unknown directional densities are determined using four equations. Initially a velocity is specified, at the north boundary, where the horizontal velocity is zero and vertical velocity is v_0 i.e. the specified velocity becomes $\boldsymbol{u_0} = \begin{pmatrix} 0 \\ v_0 \end{pmatrix}$. Adopting the usual macroscopic formulae Eq. (2-4) and Eq.(2-5) the three unknown directional densities f_4, f_7, f_8 and ρ can be computed.

The macroscopic density leads to Eq. (2-30). For the north boundary, the x and y direction macroscopic velocities can be obtained as Eq. (2-31) and Eq. (2-32).

$$\rho = f_0 + f_1 + f_2 + f_3 + f_4 + f_5 + f_6 + f_7 + f_8 \tag{2-30}$$

$$0 = f_1 + f_5 + f_8 - f_3 - f_6 - f_7 \tag{2-31}$$

$$\rho v_0 = f_2 + f_5 + f_6 - f_4 - f_7 - f_8 \tag{2-32}$$

Assuming bounceback boundary condition holds good in the direction normal to the boundary, we get another set of equation (2-33) as suggested by [21]

$$f_2 - f_2^{eq} = f_4 - f_4^{eq} \tag{2-33}$$

Eq. (2-30) to Eq. (2-33) forms a system of four equations to solve four unknowns ρ, f_4, f_7, f_8. Re-arranging Eq. (2-30) and Eq. (2-32), we get:

$$f_4 + f_7 + f_8 = \rho - f_0 - f_1 - f_2 - f_3 - f_5 - f_6 \tag{2-34}$$

$$f_4 + f_7 + f_8 = f_2 + f_5 + f_6 - \rho v_0 \tag{2-35}$$

Equating Eq. (2-34) and Eq. (2-35), and solving for ρ obtains Eq. (2-37).

$$\rho - f_0 - f_1 - f_2 - f_3 - f_5 - f_6 = f_2 + f_5 + f_6 - \rho v_0 \tag{2-36}$$

$$\rho = \frac{f_0 + f_1 + f_3 + 2(f_2 + f_5 + f_6)}{(1 + v_0)} \tag{2-37}$$

Solving Eq. (2-33) using the equilibrium distribution equation Eq. (2-29), solves for the directional density f_4 as Eq. (2-39).

$$\begin{aligned} f_2^{eq} - f_4^{eq} = &\left[\frac{1}{9}\rho + \frac{1}{3}\rho(-1.v_0) + \frac{1}{2}\rho v_0^2 - \frac{1}{6}\rho(u_0^2 + v_0^2)\right] \\ &- \left[\frac{1}{9}\rho + \frac{1}{3}\rho(1.v_0) + \frac{1}{2}\rho v_0^2 - \frac{1}{6}\rho(u_0^2 + v_0^2)\right] \end{aligned} \tag{2-38}$$

$$f_4 = f_2 - f_2^{eq} + f_4^{eq} = f_2 - \frac{2}{3}\rho v_0 \tag{2-39}$$

Re-arranging Eq. (2-31) and substituting Eq. (2-39) and Eq. (2-40) in Eq. (2-32), solves for directional density f_7 as Eq. (2-42).

$$-f_8 = f_1 + f_5 - f_3 - f_6 + f_7 \tag{2-40}$$

$$\begin{aligned} &\rho v_0 = f_2 + f_5 + f_6 - f_4 - f_7 - f_8 \\ &\rho v_0 = f_2 + f_5 + f_6 - \left(f_2 - \frac{2}{3}\rho v_0\right) - f_7 + (f_1 + f_5 - f_3 - f_6 - f_7) \end{aligned} \tag{2-41}$$

$$\rho v_0 = 2f_5 + \frac{2}{3}\rho v_0 + f_1 - f_3 - 2f_7$$

$$2f_7 = 2f_5 + \left(\frac{2}{3} - 1\right)\rho v_0 + f_1 - f_3$$

$$f_7 = f_5 + \frac{1}{2}(f_1 - f_3) - \frac{1}{6}\rho v_0 \quad (2\text{-}42)$$

Substituting the computed directional density f_4 and f_7 in Eq. (2-32), solves for f_8 as Eq. (2-44)

$$\rho v_0 = f_2 + f_5 + f_6 - f_4 - f_7 - f_8$$

$$\rho v_0 = f_2 + f_5 + f_6 - \left(f_2 - \frac{2}{3}\rho v_0\right) - \left(f_5 + \frac{1}{2}(f_1 - f_3) - \frac{1}{6}\rho v_0\right) - f_8 \quad (2\text{-}43)$$

$$\rho v_0 = f_6 + \frac{2}{3}\rho v_0 - \frac{1}{2}(f_1 - f_3) + \frac{1}{6}\rho v_0 - f_8$$

$$f_8 = f_6 - \frac{1}{2}(f_1 - f_3) - \frac{1}{6}\rho v_0 \quad (2\text{-}44)$$

Similarly, the unknown directional densities at every boundary (South, West & East) could be calculated based on the same fundamental concept, where a velocity is specified, and using macroscopic density and velocity formulae to yield a system of four equations and four unknowns to solve.

2.6.4. Dirichlet (Pressure) Boundaries

In the Dirichlet type of boundary condition, the pressure/density is restrained at the boundary, where the macroscopic velocity and unknown directional densities are calculated. Post streaming, at each lattice node, there are three directional densities which needs to be computed, facing the system back from the boundary. This can be determined when an explicit pressure/density ρ_0 is specified at the lattice nodes. Based on the assumption that velocity tangent to the boundary is zero, the velocity component normal to the boundary can be calculated. Considering the north boundary as shown in Figure 2-9, accounting for the boundary condition $\rho = \rho_0$ and the known directional densities $f_0, f_1, f_2, f_3, f_5, f_6$, the y-component of velocity v and unknown directional densities f_4, f_7, f_8 are computed. Using the macroscopic density, macroscopic velocity formula, and the assumption that bounceback is satisfied in the direction normal to the boundary as proposed

by Zou and He (1997)[21], obtains a system of four equations with four unknown which after solving is gives the following equations Eq. (2-45) through Eq. (2-48).

$$v = -1 + \frac{f_0 + f_1 + f_3 + 2(f_2 + f_5 + f_6)}{\rho_0} \tag{2-45}$$

$$f_4 = f_2 - \frac{2}{3}\rho_0 v \tag{2-46}$$

$$f_7 = f_5 + \frac{1}{2}(f_1 - f_3) - \frac{1}{6}\rho_0 v \tag{2-47}$$

$$f_8 = f_6 - \frac{1}{2}(f_1 - f_3) - \frac{1}{6}\rho_0 v \tag{2-48}$$

On a similar note, the unknown directional densities at every boundary (South, West & East) could be built based on the same fundamental concept implying through a pseudo-code. Initially computing the velocity and then using this velocity to determine the unknown direction-specific densities.

Chapter 3 Methodology

3.1. Defining the problem

Since the typical extend of pore sizes in the organic-rich shale falls in nano-pore region with high Knudsen number, the conventional continuum and Navier-Stokes equations with no-slip boundaries may fail to study the fluid flow in these nano-pores. Therefore, the gas flow model established on Darcy's law may be unfit for the reservoir flow simulation in the nano-pore region.

In this research, we explored the LBM-LS model, adopted from Fathi et al.[8], to study gas transport and storage in multi-scale pore structure of organic rich shales. The phenomenon of slip contributes as one of the major attributes of flow through porous media. Some other components, which define the flow behavior, are also examined, such as surface diffusion, Knudsen diffusion, and wall confinement. This methodology aids in investigating on the organic pore wall confinement, gas adsorption on fluid flow and storage in multi-scale pore structure with varying Knudsen number ranging from continuum flow to transition flow regimes. At different pressures, molecular level interactions of fluid molecules are investigated. Effects of temperature and pressure are studied on the shale gas transport in kerogen. The results are then analyzed and compared with traditional Poiseuillar flow, Klinkenberg slippage flow [22], modified Klinkenberg slippage flow [23] that capture the wall effect.

3.2. Flow of gas through a straight capillary with slip

Kundt and Warburg (1875) confirmed that when gas is flowing across a solid wall, the layer immediate to the solid wall moves with respect to the solid wall i.e., if the wall velocity is stationary, the gas layer adjacent to the wall has a finite velocity. This indicates Poiseuille law that assumes zero gas velocity by the wall underestimates the gas mass flux.

If the layer next to the wall has a thickness less than the mean free path λ of the gas molecules- no collision takes place in this layer. In this thin layer at a given point, half of the gas molecules move with a velocity component towards the wall and the other half move away from the wall. The average velocity of gas molecules moving towards the wall have a non-zero velocity as their last collision was taken place at a distance from the wall in the bulk. The other half coming back from the wall assuming in-elastically colliding with the solid wall would lose a fraction or all of their

average velocity in the direction of the flow. Still, the average velocity component of all the molecules in the direction of flow in the layer will at least be equal to half of the average velocity of the molecules moving towards the wall. Therefore the velocity of gas in this layer adjacent to the solid wall has a finite flow rate. Klinkenberg assuming inelastic collision of molecules by the wall and constant velocity gradient across the capillary developed his slippage theory.

Researchers, such as Kundt and Warburg presented that Klinkenberg's assumption of velocity gradient being constant across the capillary width is not true, and that the velocity gradient near the wall is much higher than the velocity gradient away from the wall [22], implying that the velocity at the center of the pore is nearly the same than compared to velocities closer to the solid wall.

The velocity equation considering the gas flow through a straight capillary having slip flow is represented by Eq. (3-3)[22], here r, r_0, and λ are defined as the distance from the center of the capillary, capillary half-width, mean free path respectively. The proportionality constant- c although assumed to be slightly less than 1, in this study the value of c is considered to as 1. The term cλ is calculated for the Klinkenberg's slip equation using Eq. (3-4).

$$u = -\frac{1}{4\mu}\frac{dP}{dx}(r_0^2 - r^2 + 2c\lambda r_0) \tag{3-1}$$

$$u = -\frac{1}{4\mu}\frac{dP}{dx}r_0^2\left(1 - \left(\frac{r}{r_0}\right)^2 + \frac{2c\lambda}{r_0}\right) \tag{3-2}$$

$$u = -u_{ymax}\left(1 - \left(\frac{r}{r_0}\right)^2 + \frac{2c\lambda}{r_0}\right) \tag{3-3}$$

$$\mathrm{c}\lambda = \frac{\mathrm{c}\mu}{\rho}\sqrt{\frac{\pi M}{2RT}} \tag{3-4}$$

When the fluid in contact with the wall does not slip i.e. when $c\lambda = 0$, the Klinkenberg's slippage equation reduces to Poiseuille equation.

3.3. Modified Klinkenberg's slippage equation

The study on modifyingKlinkenberg slippage equation introduces a new analytical procedure [23] based on Klinkenberg's research, Kundt and Warburg's conclusions to predict the slippage of gas

molecules in low permeable porous media, and provides improved reservoir simulation fluid flow model.

The original work of Klinkenberg assumes a constant velocity gradient which holds well in high permeable formations but deviates at low permeable formations. According to Kundt and Warburg, the velocity gradient changes with the distance from the wall and is higher closer to the wall than towards the center of the pore. To incorporate the velocity gradient changes across the capillary tube, a Taylor series approximation to the second order for computing the velocity near the wall is considered as shown in Eq. (3-7) [23]. The derivation to calculate the velocity of gas flow in a straight capillary tube implementing the second order Taylor series gives the maximum non-trivial value while determining the slip boundary condition. If higher order Taylor series would have been implemented, to solve for the boundary condition, the higher derivatives of velocity will become zero indicating the significance of second order Taylor series expansion. The terms r, r_0 and λ are defined as the distance from the center of the capillary, capillary half-width, mean free path respectively. The value of proportionality constant- c is assumed to be 1. The term cλ is calculated using Eq. (3-8) for the modified Klinkenberg slippage equation Eq. (3-5) to Eq.(3-7).

$$u = -\frac{1}{4\mu}\frac{dP}{dx}(r_0^2 - r^2 + 2c\lambda r_0 - (c\lambda)^2) \tag{3-5}$$

$$u = -\frac{1}{4\mu}\frac{dP}{dx}r_0^2\left(1 - \left(\frac{r}{r_0}\right)^2 + \frac{2c\lambda}{r_0} - \left(\frac{c\lambda}{r_0}\right)^2\right) \tag{3-6}$$

$$u = -u_{ymax}\left(1 - \left(\frac{r}{r_0}\right)^2 + \frac{2c\lambda}{r_0} - \left(\frac{c\lambda}{r_0}\right)^2\right) \tag{3-7}$$

$$c\lambda = \frac{m}{P}\ where, m = \mathrm{c}\left(\frac{\mu}{\rho}\sqrt{\frac{\pi M}{2RT}}\right)\left(\frac{\rho RT}{M}\right) = c\mu\sqrt{\frac{\pi RT}{2M}}\ \left[\because P = \rho\frac{RT}{M}\right] \tag{3-8}$$

This study states that at low permeable formations, there is a deviation from Klinkenberg's assumption where the mean free path is not completely inversely proportional to pressure. It also demonstrates that while considering larger pores, the permeability equation reduces to Klinkenberg's permeability equation because the mean free path becomes very small and the term $(c\lambda)^2$ becomes negligible. The relevance of the above equation Eq. (3-7) is justifiable under the

assumption of continuum flow and when slip flow is influential i.e., where Knudsen number is lower than 0.1 [23].

3.4. Lattice Boltzmann Model

The lattice Boltzmann simulation model used here incorporates the molecular interactions (adsorptive/cohesive forces) between the fluid particles (fluid-fluid, fluid-solid) and a Langmuir-slip boundary condition defined at the organic pore wall studied on a 2D D2Q9 lattice. This method regards natural gas as a group of spherical particles which continuously collide elastically and stream in capillaries defined in a 2D discrete square lattice. The particles internally interact with themselves and the boundary surface walls leading to a viscous-flow inside the capillary. The particles collectively obey the Boltzmann transport equation, however, the lattice space and time evolution of particles is analyzed by predicting velocities at each node within the capillary. This method can not only deal with complex pore geometry but also can serve for high Knudsen number regime, beneficial in simulating interfacial dynamics originated from fluid-fluid or fluid-solid interactions such as, surface tension, cavitation, or adsorption in porous materials.

Applying the right boundary condition to the pore walls has been extensively studied for LBM development (Martys and Chen 1996 [24]; Or and Tuller 2002 [25]; Sukop and Or 2005 [9]). It is critical to understand the slip boundary conditions at the wall for gas flows. Research has been done to alter the common bounce-back boundaries (Nie et al. 2002 [26]), combining the bounce back and specular reflection (Succi 2002 [27]). One of the widely used approach to define the slip velocity for rarified gas flow is the Maxwell slip model, where the slip velocity is a function of Knudsen number, velocity gradient, and an accommodation coefficient. In the Maxwell's model, the slip velocity was greatly dependent on the accommodation coefficient which lead to deviated results from the standard values (Maxwell 1879 [28]; Myong 2004 [29]; Kim et al. 2007 [30]; Chen and Tian 2009 [31]). Langmuir theory of equilibrium adsorption was also adopted to attribute for the accommodation coefficient (Myong 2004 [29]; Myong et al. 2005 [32]). Later, the Langmuir slip model was found successful in dealing with the micro flow problems (Myong 2004 [29]; Myong et al. 2005 [32]) which is later stated in this process.

Based on the earlier analysis on gas storage and transport, the results from numerical and experimental procedures explained the emphasis of wall-dominated transport in organic-rich shale

(Fathi and Akkutlu 2013[8], 2011 [33], 2009 [34]; Kang et al. 2011 [4]). In the previous studies the slippage surface-transport mechanisms were examined with the integration of Langmuir slip boundary condition to the existing LBM, naming it LBM-Ls (Fathi and Akkutlu 2013 [8]). In this model, the adsorbed phase transport at the surface was proposed as a moving wall, whose velocity was determined locally using the Langmuir-isotherm equation. The results point to the existence of a critical Knudsen number value for the onset of laminar gas flow under typical shale gas reservoir pressure conditions. Suggesting beyond this critical number classical approach for modeling gas flow based on Darcy's law is not valid and transport mechanism is diffusion under the influence of molecular streaming (i.e., slippage and surface diffusion) by the organic pore walls [8].

3.5. Modified Langmuir slip Boundary Condition

Boundary conditions play an important role in studying the fluid-fluid and fluid-solid molecules interactions in LBM simulations. The Langmuir slip model took over the Maxwell slip model to eliminate the shortcoming of having the accommodation coefficient as a free parameter. It is assumed that gas molecules interact with solid surface and get adsorbed to the wall and desorbed into the fluid respectively with some time lag. The measure of adsorbed gas molecules to the walls complies with the equilibrium Langmuir isotherm illustrated as Eq.(3-9).

$$\alpha = \frac{C_\mu}{C_{\mu s}} = \frac{KC}{1 + KC} \tag{3-9}$$

where C_μ is the adsorbed gas density and $C_{\mu s}$ is the highest monolayer adsorption capacity, K is the Langmuir partition coefficient, and C is the free gas density. The equilibrium Langmuir isotherm can also be written in terms of pore pressure P as Eq. (3-10).

$$\alpha = \frac{V_a}{V_{amax}} = \frac{\frac{1}{P_L}P}{1 + \frac{1}{P_L}P} \tag{3-10}$$

where α is described at a fixed temperature, V_a is the adsorbed gas volume, V_{amax} is the maximum monolayer adsorbed gas volume, and P_L is the Langmuir pressure (when $V_a = V_{amax}/2$). The fluid velocity by the wall U_W is proposed as a function of α as Eq. (3-11).

$$U_W = (1-\alpha)U_{g,slip} + \alpha U_{surf} \tag{3-11}$$

Where $U_{g,slip}$ is the velocity of gas which is one mean free path distance away from the wall, U_{surf} is the local wall velocity due to the adsorbed-phase transport. When $\alpha = 1$ (adsorbed gas volume reaches the maximum monolayer adsorbed gas volume by increase in free gas pressure) the wall velocity becomes equal to the adsorbed phase velocity; and as α decreases (decline in pore pressure) the wall velocity becomes equal to slip velocity.

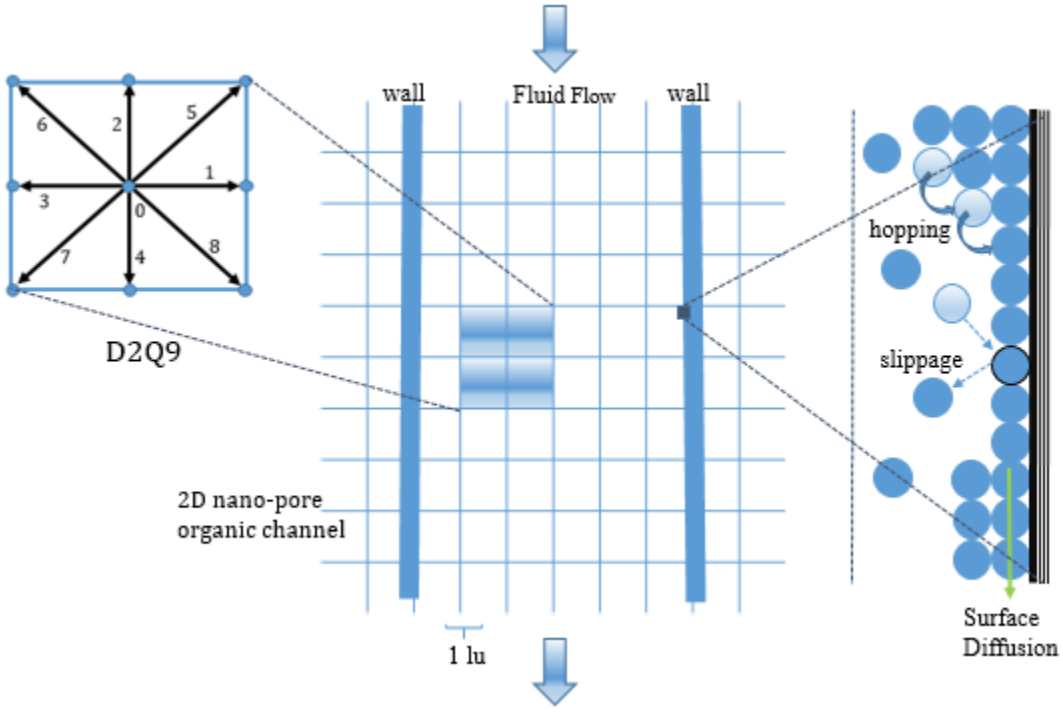

Figure 3-1: Schematic diagram presenting the D2Q9 lattice pattern, lattice geometry showing the flow of fluid in organic capillary, and molecular surface transport mechanisms at the wall

Chen and Tian (2009 [31], 2010 [35]) technique is been followed to incorporate the Langmuir boundary condition where the solid wall laps over the boundary nodes, shown in Figure 3-1.

The distribution function is required to be studied for the boundary node 0 using the Langmuir slip model. According to the Chapman-Enskog approach, the distribution function at the wall can be split into equilibrium and non-equilibrium sectors [36] as presented in Eq. (3-12).

$$f(0,t) = f^{eq}(0,t) + (1-\eta)f^{neq}(0,t) \tag{3-12}$$

Where, superscripts 'eq' and 'neq' represents the equilibrium and non-equilibrium sectors of distribution function, respectively, and η is explained as $\eta = 1/(\tau_{eff} + 0.5)$. From Chen and Tian (2009 [31], 2010 [35]) approach the f^{eq} and f^{neq} sections can be written as Eq. (3-13).

$$\begin{cases} f^{eq}(0,t) = \alpha f^{eq}(W,t) + (1-\alpha)f^{eq}(g,t) \\ f^{neq}(0,t) = \alpha f^{neq}(W,t) + (1-\alpha)f^{neq}(g,t) \end{cases} \tag{3-13}$$

As the macroscopic fluid density and macroscopic fluid velocity at any time (t) can be computed, the f^{eq} and f^{neq} can be determined. The adsorbed and free mass fluxes by the wall are based on Fickian diffusive transport as shown in Eq. (3-14) and Eq. (3-15).

$$J_{ads} = U_{surf}\frac{\rho_{ads}}{M} = -D_S\frac{\partial C_\mu}{\partial x} \tag{3-14}$$

$$J_{free} = U_{g,slip}\frac{\rho_g}{M} = -D_K\frac{\partial C}{\partial x} \tag{3-15}$$

where M is the molecular weight of the gas, D_S is the surface diffusion coefficient, and $\frac{\partial C_\mu}{\partial x}$ is the gradient of adsorbed gas concentration. This gradient can be determined using the chain rule and the Langmuir isotherm Eq. (3-9), identifying that velocity of gas (U_g) and density of gas (ρ_g) closer to the wall can be found at each timestep, as Eq. (3-16).

$$\frac{\partial C_\mu}{\partial x} = \frac{\partial C_\mu}{\partial C}\frac{\partial C}{\partial x} = \frac{KC_{\mu s}}{(1+KC)^2}\frac{\partial C}{\partial x} \tag{3-16}$$

Therefore, the local wall velocity is derived to be Eq. (3-17).

$$U_{surf} = \left(\frac{D_S}{D_K\rho_{ads}}\right)\left[\rho_g U_{g,slip}\frac{KC_{\mu s}}{(1+KC)^2}\right] \tag{3-17}$$

From the previous work done by Tang et al. 2005 [37], 2008 [38]; Chen and Tian 2009 [31], 2010 [35], the equilibrium distribution function at the wall can be determined as Eq. (3-18) (when the wall temperature and velocity is known at each timestep).

$$f^{eq}(W,t) = f^{eq}\left(\rho_g, T_W, U_{surf}, t\right) + O(\varepsilon^2) \tag{3-18}$$

This equilibrium distribution function implants a second order truncation error, ε is an arbitrary small quantity. On similar terms, the non-equilibrium distribution function can also be approximated as (Chen and Doolen 1998 [36]; Tang et al. 2005 [37], 2008 [38]; Chen and Tian 2009 [31], 2010 [35])

$$\begin{cases} f^{neq}(W,t) = f^{neq}\left(\rho_g, T_g, U_{g,slip}, t\right) + O(\varepsilon^2) \\ f^{neq}(W,t) = f\left(\rho_g, T_g, U_{g,slip}, t\right) - f^{eq}\left(\rho_g, T_g, U_{g,slip}, t\right) + O(\varepsilon^2) \end{cases} \quad (3\text{-}19)$$

Replacing the equations of f^{eq} and f^{neq} into the Chapman Enskog's distribution function at the wall, the eventual distribution function can be approximated as Eq. (3-20) [8]

$$f(0,t) = \alpha f^{eq}\left(\rho_g, T_W, U_{surf}, t\right) + (1-\alpha) f^{eq}\left(\rho_g, T_g, U_{g,slip}, t\right) + (1-\eta)\left[f\left(\rho_g, T_g, U_{g,slip}, t\right) - f^{eq}\left(\rho_g, T_g, U_{g,slip}, t\right)\right] + O(\varepsilon^2) \quad (3\text{-}20)$$

This methodology presents second-order accuracy, hence, the stability and accuracy are conserved by using this procedure [35].

3.6. Single Component, Multiphase (SCMP) LBM

Many researchers developed the single component multiphase LBM models that retains the molecular physics of the problem by providing a more practical and consistent analysis of the equation of state. Initially the work began with designing the lattice gas single component multiphase model. Later these models were incorporated using lattice Boltzmann method [39]. Next came the "free energy" approach, 'finite density' approach [40] that employs the Enskog equation for dense gases. A new approach was introduced where the temperature component was recorded. The relative permeability concepts for multicomponent system established on Darcy's law and using LBM was studied [9]. A flexible model described by Shan and Chen (1993) [39] is taken up in our research as it incorporates both solid interactions and fluid interactions as explained in the below section. .

3.6.1. Interparticle Forces and their Incorporation into LBM

The major differentiating aspect of SCMP LBM is the integration of attractive forces between fluid particles. For multiphase fluid interactions (in our case, two-phase), long range fluid interactions are incorporated between fluid particles. For a D2Q9 model, cohesive (attractive) force F between

nearest neighbor fluid particles was proposed previously by Shan and Chen (1993) [39] as Eq. (3-21).

$$F(x,t) = -G\psi(x,t)\sum_{a=1}^{8} w_a \psi\,(x + e_a \Delta t, t) e_a \tag{3-21}$$

Where G is the interaction strength (G < 0 for attraction between particles and the force is stronger when the density is higher causing surface tension phenomena), w_a is the weighting factor as defined for D2Q9 model, and ψ is the interaction potential. As stated by Shan and Chen (1993) [39], the interaction potential function should be monotonically increasing and bounded, which is a function of fluid density and arbitrary constant ρ_0, defined as Eq. (3-22).

$$\psi(\rho) = \rho_0 \left[1 - \exp\left(-\frac{\rho}{\rho_0}\right)\right] \tag{3-22}$$

Initially, Martys and Chen (1996) [24] considered $\psi = \rho$, later the interaction potential function as $\psi(\rho) = 1 - \exp(-\rho)$ was considered [9].

The equation of state (EOS) relating pressure and density in the single component single phase (SCSP) D2Q9 model is, $P = c_s^2 \rho = \frac{\rho}{3}$ [9]

Addition of cohesive interactive forces induces non-ideal equation of state (EOS) for the simulated fluids (He and Doolen, 2002 [40]) as Eq. (3-23).

$$P = \rho RT + \frac{GRT}{2}[\psi(\rho)]^2 \tag{3-23}$$

The term, ρRT represents the ideal gas law, addressing the single component, single phase model. For SCSP and SCMP models, the value of RT is precisely considered as $1/3$, leading the non-ideal equation of state to turn into Eq. (3-24).

$$P = \frac{\rho}{3} + \frac{G}{6}[\psi(\rho)]^2 \tag{3-24}$$

The next term $\frac{GRT}{2}[\psi(\rho)]^2$ serves as the non-ideal part accounting for the cohesive force between the molecules, resulting in a decline in pressure (when G < 0) and the non-linearity of the EOS. When the interaction strength between molecules becomes fairly negative, then the EOS becomes subcritical causing a phase separation, non-monotonic in nature.

3.6.2. Fluid-Surface Forces

Inclusion of adhesive force interaction fluid-surface is imperative to broaden the simulation of single component multi-phase in porous media. The basic methodology given by Martys and Chen (1996) [24] leads to phase separation by constructing an analogue to the particle-particle interaction force. In this method, the force interaction strength is determined by an adsorption coefficient (G_{ads}) and the sum of solid variable indicator is taken into consideration. The equation Eq. (3-25) illustrates the adhesive force between fluid and solid surface:

$$F_{ads}(x,t) = -G_{ads}\psi(x,t)\sum_{a=1}^{8} w_a s(x + e_a\,\Delta t)e_a \tag{3-25}$$

Here, s is a solid variable indicator which equals one if the site at $x + e_a\Delta t$ is a solid, and equals zero otherwise and w_a is the direction-dependent weighting factor as defined for D2Q9 model.

To summarize from above set of equations introduced to incorporate the interparticle forces, the cohesive (attractive) force F between nearest neighbor fluid particles was measured using Eq. (3-21); the interaction potential function is defined as Eq. (3-22); the non-ideal EOS is described by Eq. (3-24). Also, the adhesive force between fluid and solid surface is measured using Eq. (3-25) explained briefly in the sections above.

3.6.3. Simulation real gas properties

The adopted lattice Boltzmann numerical simulation [8] is been studied on high pore pressure of 1623 psi and low pore pressures of 600 and 300 psi; and the effects of temperature is investigated at the atmospheric temperature of 77 F, 150 F and 300 F each. The properties of pure-methane gas, such as- adsorbed gas density (ρ_{ads}) Langmuir pressure (P_L) maximum monolayer adsorbed gas volume (V_{amax}), are collected from previous experimental results of Kang et al 2011 [4]; Ambrose et al 2012 [41]; Didar [42] through studying the methane adsorption in organic pores on different shale samples as presented in Table 3-1. For the correction of $RT = \frac{1}{3}\ (lattice\ units)$ in ideal gas equation where R is universal gas constant and T is the temperature, to the real gas having the additional term ψ, Eq. (3-22), involves arbitrary constants ρ_0, ψ_0, interaction potential (G) [9] which are calculated by history matching the pressure/density curve of real gas methane with one obtained from LBM model with lattice width size of 50 lu, borrowed from the work done by Fathi et. al[8].

Table 3-1-: Methane gas properties used in the LBM simulation

ρ_{ads}	$0.4\ gm/cm^3$
$C_{\mu s}$	$0.025\ mol/cm^3$
P_L	$1800\ psi$
V_{amax}	$0.1962\ cm^3$
ρ_0	3
G	-0.4

3.7. Comparison of slip flow with various analytically derived solutions

To analyze the effect of slip velocity of a two-dimensional isothermal gas flow between parallel plates, with changing matrix pore size and Knudsen number, various analytically derived and empirical correction models exist. For a second-order slip model, the normalized slip velocity is calculated using first-order slip coefficient (C_1) and second-order slip coefficient (C_2) described in Eq. (3-26) [43]and the values listed in Table 3-2.

$$\frac{U_{slip}}{U_o} = 4(C_1 Kn + 2C_2 Kn^2) = 4C_1 Kn + 8C_2 Kn^2 \tag{3-26}$$

$$U_o = U_{max} - U_{slip} \tag{3-27}$$

where U_{slip} is the slip velocity calculated at the fluid-wall boundary, U_o is the velocity with which the slip velocity is normalized to compare different slip models and Kn is the Knudsen number.

Table 3-2-: List of various second-order slip models and slip coefficients [44]

Authors	$\boldsymbol{C_1}$	$\boldsymbol{C_2}$
Schamberg, 1947 [45]	1	$5\pi/2$
Cercignani, 1964 [46]	1.1466	0.9756
Hadjiconstantinou, 2003 [47]	1.1466	0.647
Deissler, 1964 [48]	1	9/8
Sreekanth, 1969 [49]	1.1466	0.14

Hsia and Domoto, 1983 [50]	1	0.5
Mitsuya, 1993 [51]	1	2/9
Beskok et al., 1996 [52]	1	-0.5

Notice that the second-order slip coefficient (C_2) is positive for most of the slip boundary models shown in Table 3-2. The value of C_2 being positive, negative or zero impacts in the deviation from a straight line (Klinkenberg slippage theory) when normalized slip velocities are plotted against Knudsen number. Considering the coefficients C_1 & C_2 from the Hsia and Domoto model (1 & 0.5) when plugged in Eq. (3-26), it is observed that the first and second-order coefficients have the same action as C_2 is positive. Similarly when considering the Beskok et al. model (1 & -0.5) the first and second-order coefficients have dissimilar action as C_2 is negative.

The ratio of apparent permeability (K_a) to intrinsic permeability (K) in a parallel channel is given by Eq. (3-28) which is dependent on Knudsen number [44]. According to Klinkenberg slippage theory, the permeability ratio at a finite pressure is expressed as Eq. (3-29). However, this equation was modified later by researcher Fathi et al. (2012) [1] to incorporate the kinetic energy of the bouncing back molecules by introducing a new length scale (L_{Ke}) given by Eq. (3-30) and found that the fluid flow is significantly higher than those predicted by Klinkenberg slippage theory, capturing the momentum carried by the bouncing-back molecules to the bulk fluid developed across the capillary width (less than 100 nm) i.e. double slippage. At larger capillaries, the correction to Klinkenberg slip theory Eq. (3-30) becomes Eq. (3-29) as the kinetic effect of gas molecules become negligible, where (L_{Ke}/λ) becomes the same order as (p/b). When Eq. (3-30) is expanded to include b/p, and re-arranged, leads to Eq. (3-32) where the ratio of permeability is a function of Knudsen number with only first-order slip coefficient suggesting that one might not even need to use the second order expansion of the Knudsen number as the relationship is most likely to be linear (this will be discussed in more details in section 4.4).

$$\frac{K_a}{K} = 1 + 6C_1Kn + 12C_2Kn^2 \tag{3-28}$$

$$\frac{K_a}{K} = 1 + \frac{b}{p} \qquad where, \frac{b}{p} = \frac{4c\lambda}{r} \tag{3-29}$$

$$\frac{K_a}{K} = 1 + \left(\frac{b}{p}\right)^2 \left(\frac{L_{Ke}}{\lambda}\right) \qquad where, \frac{b}{p} = \frac{4c\lambda}{r} \tag{3-30}$$

$$\frac{K_a}{K} = 1 + \left(\frac{32c^2}{r}\right) L_{Ke} Kn \tag{3-31}$$

$$\frac{K_a}{K} = (1 + C_1 Kn) \qquad where, C_1 = \left(\frac{32c^2}{r}\right) L_{Ke} \tag{3-32}$$

3.8. Procedure

First to study the flow behavior in organic nano capillary tubes, the Klinkenberg slip equation Eq. (3-3) and modification of Klinkenberg slip flow equation Eq. (3-7) are used to examine the maximum velocity at the center of capillary and wall velocity based on a range of Knudsen numbers varying between continuum to transition flow regimes.

Next, the effect of slippage, wall confinement, Knudsen and surface diffusion are analyzed through the new LBM-Ls model[8]. This model comprises of the followings: the lattice Boltzmann equation Eq. (2-2), lattice pattern and local equilibrium distribution function Eq. (2-29) defined as described in the preceding sections of Chapter-2. A D2Q9 model is adapted having nine-speed square lattice where at each lattice node its velocity in 8 directions are outlined Eq. (2-3). The BGK collision operator with a single relaxation time Eq. (2-6); relationship between relaxation time and kinematic viscosity in continuum flow Eq. (2-24) (to eradicate the second order truncation error in lattice Boltzmann equation); effective relaxation time (corrected for large Knudsen number) Eq. (2-25); macroscopic fluid density Eq. (2-4); and macroscopic velocity Eq.(2-5) are all used to characterize the flow problem along with the boundary conditions.

Periodic boundary condition is applied at the capillary inlet and outlet making the system closed. To account for the adsorbed phase transport and slip flow by the walls, the modified Langmuir slip boundary condition is applied, defined as Eq. (3-9) to Eq. (3-20). The cohesive and adsorptive forces are added to the equilibrium distribution function that reorients the particle distribution at a node to the direction of force term as described in Eq. (3-23) and Eq. (3-25).

To analyze the effect of slip velocity with changing matrix pore size and Knudsen number, the normalized slip velocity from LBM results are compared with various analytically derived second-order slip models. The normalized slip velocity is calculated by Eq. (3-26) using first-order and second-order slip coefficients described in Table 3-1. As the second-order slip coefficient determines the deviation from straight line when the normalized velocities are plotted against Knudsen number, C_2 is considered as zero and the velocity profiles are matched with a new set of first-order slip coefficients.

Chapter 4 Results and Discussions

4.1. Knudsen Number Regime in this research

Table 4-1 describes the range of Knudsen number values changing between continuum flow ($Kn \leq 0.001$), slip flow ($0.001 < Kn \leq 0.1$), and transition flow ($0.1 < Kn \leq 10$). As the capillary pore width size decreases, the average distance travelled by a gas molecule before colliding with another gas molecule increases, resulting in increased Knudsen number values, for a particular temperature and pressure. It is also observed that the flow changes from continuum to transition as the temperature increases or pore pressure drops.

With the change in pressure and temperature, the Knudsen number value varies as shown in Table 4-1. According to the definition of Knudsen number ($Kn = \frac{\lambda}{L}$). The mean free path, λ is inversely proportional to the pore pressure. From Table 4-1, it is clear that the Knudsen number value is inversely proportional to pressure and is directly proportional to temperature. The area highlighted in orange falls in continuum flow regime, while blue region signifies slip flow, and yellow shows the transition flow regime.

Table 4-1: Knudsen number values of varying capillary width sizes at different pore pressures and reservoir temperatures

Pore Pressure	Reservoir Temperature	Capillary Width (nm)							
		100 nm	50 nm	30 nm	20 nm	15 nm	10 nm	8 nm	5 nm
1623 psi	77 F	5.51E-03	1.10E-02	1.84E-02	2.75E-02	3.67E-02	5.51E-02	6.88E-02	1.10E-01
	150 F	6.62E-03	1.32E-02	2.21E-02	3.31E-02	4.41E-02	6.62E-02	8.28E-02	1.32E-01
	350 F	9.64E-03	1.93E-02	3.21E-02	4.82E-02	6.43E-02	9.64E-02	1.21E-01	1.93E-01
600 psi	77 F	1.34E-02	2.68E-02	4.47E-02	6.71E-02	8.94E-02	1.34E-01	1.68E-01	2.68E-01
	150 F	1.63E-02	3.25E-02	5.42E-02	8.14E-02	1.08E-01	1.63E-01	2.03E-01	3.25E-01
	350 F	2.40E-02	4.80E-02	8.00E-02	1.20E-01	1.60E-01	2.40E-01	3.00E-01	4.80E-01
300 psi	77F	2.67E-02	5.34E-02	8.91E-02	1.34E-01	1.78E-01	2.67E-01	3.34E-01	5.34E-01
	150 F	3.22E-02	6.44E-02	1.07E-01	1.61E-01	2.15E-01	3.22E-01	4.02E-01	6.44E-01
	350 F	4.72E-02	9.44E-02	1.57E-01	2.36E-01	3.15E-01	4.72E-01	5.90E-01	9.44E-01

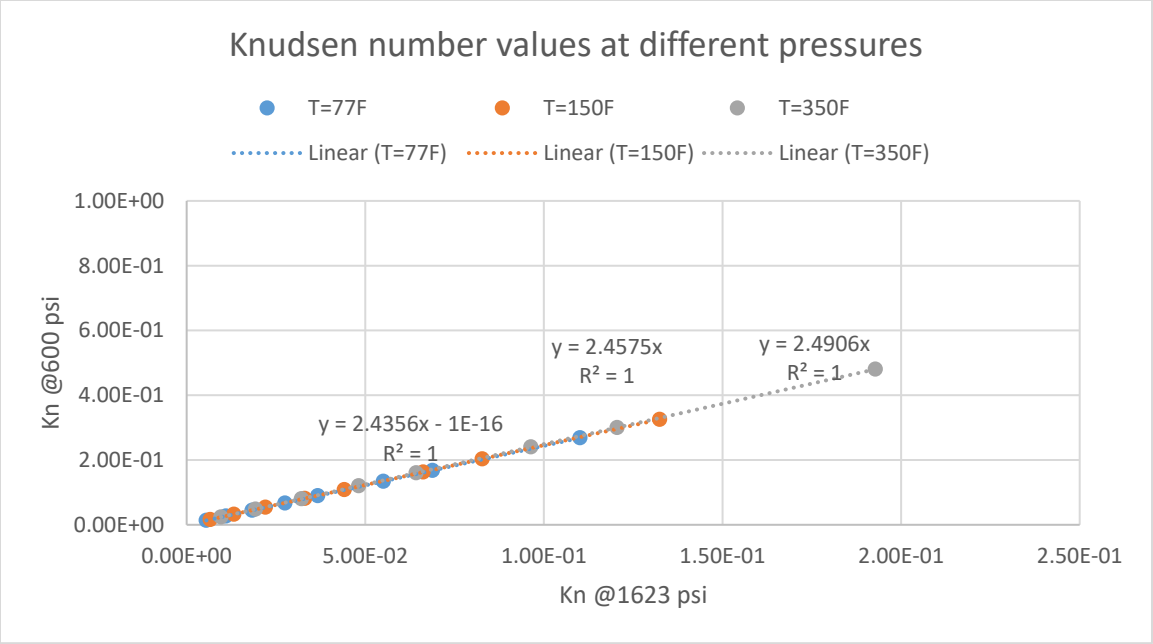

Figure 4-1: Range of Knudsen number values plotted between 1623 psi and 600 psi

A linear trend line is observed (Figure 4-1) with a slope of 2.4 and negligible intercept when Knudsen number values at 1623 psi, 77F are plotted against Knudsen number values at 600 psi, 77F. It is interesting that the same straight-line relationship holds as temperature changes i.e., approximately same value of slope is obtained when Knudsen number values at 1623 psi, 150F are plotted against Knudsen number values at 600 psi, 150F and similarly for 350F. During this process it is observed that as the temperature increases from 77F to 350F, the flow changes from continuum to transition flow. The value of slope is the ratio of Kinematic viscosities at changing pressures, refer to Eq. (2-27), when all the other parameters like temperature and capillary width are constant.

Similar trends are collected when Knudsen numbers at 600 psi are plotted against Knudsen numbers at 300 psi with a slope of 1.9. When Knudsen numbers at 1623 psi are plotted against Knudsen numbers at 300 psi a straight line is obtained having slope of 4.8 (attached in appendix Figure 0-1 and Figure 0-2). For practical purposes, it can be noted that the ratio of Knudsen numbers is a function of pressure and is independent of pore size and temperature.

4.2. Fluid flow using Analytical Poiseuille flow and, Klinkenberg slippage equation

To begin with, the gas behavior is studied across capillary widths ranging from 100 nm to 5 nm, the pore pressure and reservoir temperature is altered between 1623 psi, 600 psi, 300 psi and 77F, 150F, 350F respectively to consider the effects of pressure and temperature on fluid flow.

4.2.1. Analytical Solution

Figure 4-2 uses the Analytical solution and the maximum center velocities are plotted from larger to smaller capillary tubes at different pore pressures and temperatures as mentioned above. It is observed that the maximum velocities is higher for larger pore capillary widths; and as the capillary width narrows down to 20nm or below (high Knudsen number), the maximum velocity converges to very small value. Considering the velocity profile at a constant temperature of 77F with varying pore pressure, it is evident from Figure 4-3 (a) that as the pressure decreases from 1623 psi, 600 psi to 300 psi; the maximum velocities increases with increase in capillary width. Next, considering a particular pressure of 1623 psi and studying the effect of temperature on velocity profile, it is observed from Figure 4-3 (b) that as the reservoir temperature increases from 77F, 150F to 350F; the maximum velocity decreases with decrease in capillary widths.

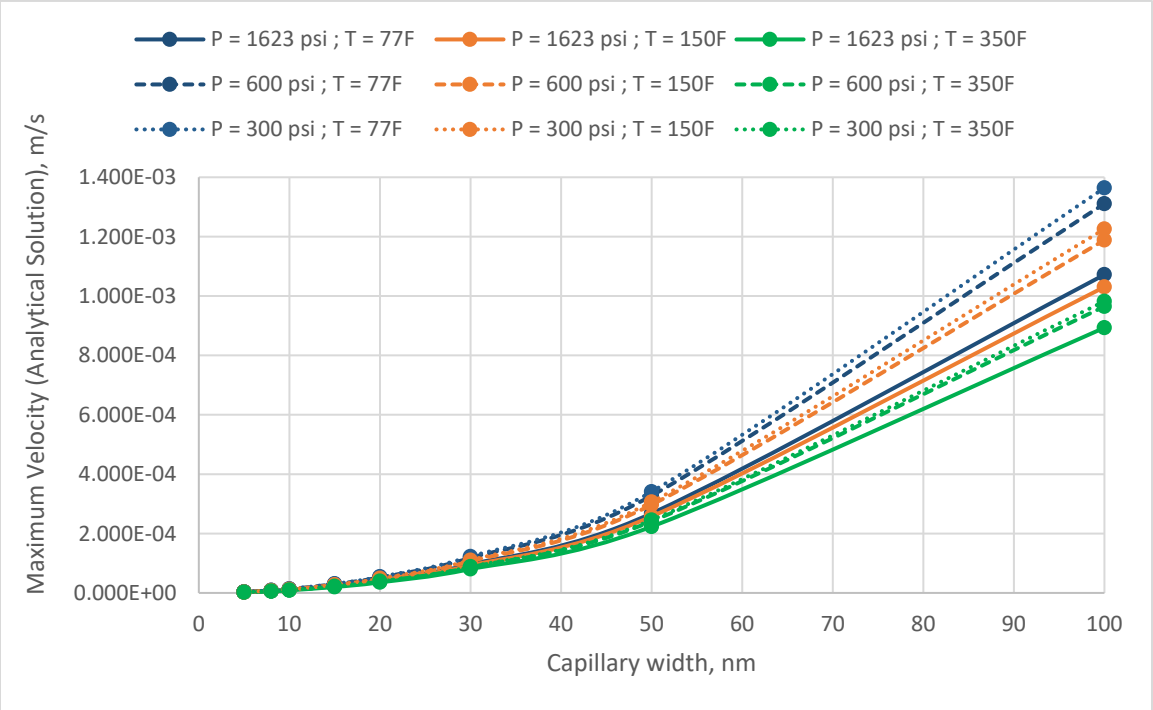

Figure 4-2: Plot displaying the maximum velocity of varying capillary widths from 5 nm to 100nm using analytical solution at different pore pressures and reservoir temperatures.

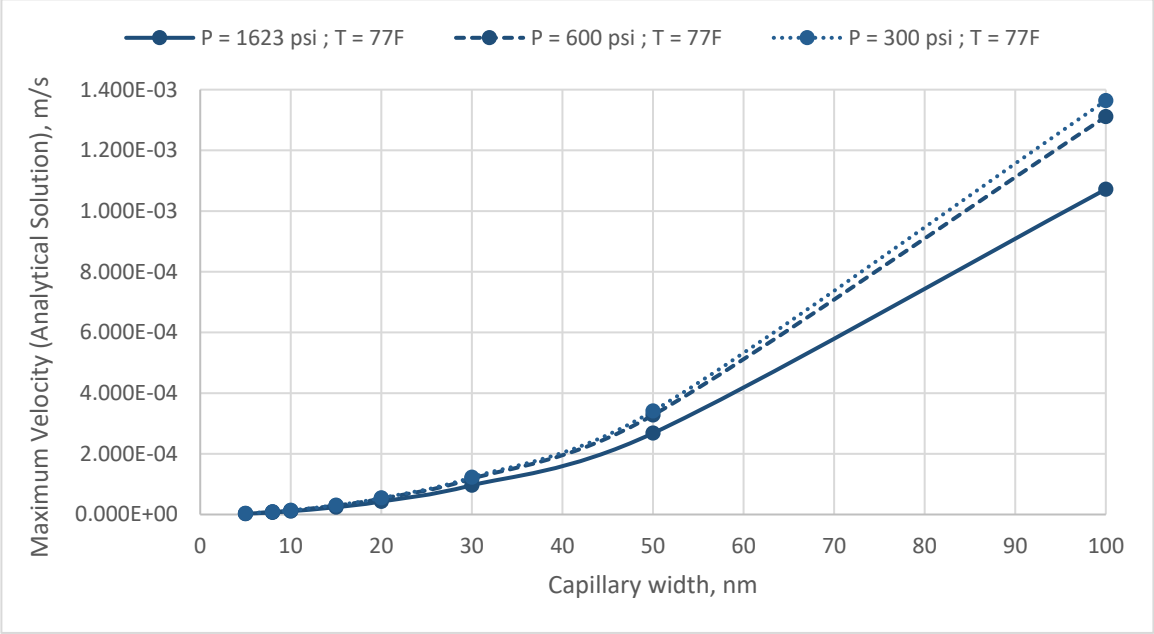

(a)

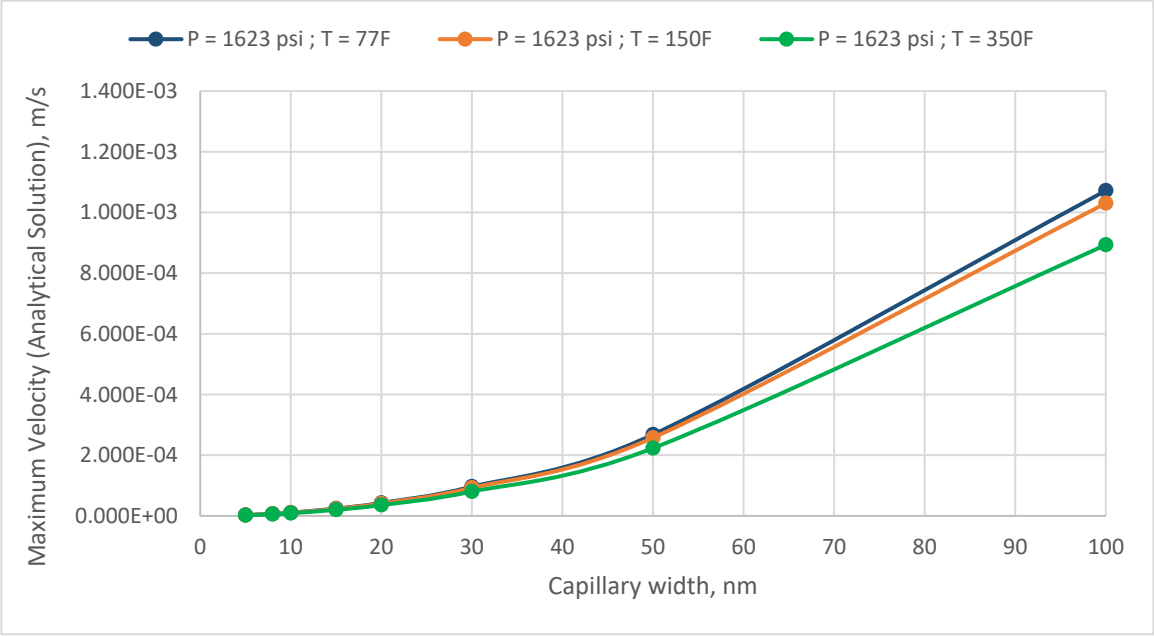

(b)

Figure 4-3: Plot displaying maximum velocity of varying capillary widths from 5 nm to 100 nm using analytical solution at (a) constant temperature of 77F, (b) constant pore pressure of 1623 psi

In figures 4-3, 4-4a and 4-4b, there are three regions which can be clearly identified. In capillaries with pore size larger than 50 nm changes in pressure and temperature result in linear decrease in

maximum capillary velocity with decreasing pore width using analytical solution of Poiseuille equation. Between 30-50 nm there is a non-linear decrease in velocity with decreasing capillary width, i.e., transition region, and below 30 nm another straight-line relationship observed, however with much slower paste between decrease in maximum velocity and decrease in capillary width. We use this behavior as characteristics of traditional flow modeling as a function of pore width, temperature and pressure using Poiseuille law and will compare that with different models published and our new lattice Boltzmann model.

4.2.2. Klinkenberg Slippage Equation and Modified Klinkenberg slip Equation

Kundt and Warburg (1875) confirmed that when gas is flowing across a solid wall, the layer immediate to the solid wall moves with respect to the solid wall i.e., if the wall velocity is stationary, the gas layer adjacent to the wall has a finite velocity called the slip velocity. The velocity equation considering the gas flow through a straight capillary having slip flow is represented by Klinkenberg slippage equation Eq. (3-3) [22].

The original work of Klinkenberg assumes a constant velocity gradient which holds well in high permeable formations but deviates at low permeable formations (smaller capillary tubes). According to Kundt and Warburg, the velocity gradient changes with the distance from the wall and is higher closer to the wall than towards the center of the pore. To incorporate the velocity gradient changes across the capillary tube, a Taylor series approximation to the second order for computing the velocity near the wall is considered as shown in Eq. (3-7) [23].

The maximum velocities at the center of the capillary are plotted from larger to smaller capillary tubes at different pore pressures and temperatures using both the Klinkenberg slippage equation and modified Klinkenberg slippage equation shown in Figure 4-4 and Figure 4-5 respectively. The maximum velocities at the center of the capillary from Eq. (3-3) and Eq. (3-7) presents an analogy with the analytical solution (Figure 4-2) i.e. the center velocity has an inverse relationship with the pore pressure and reservoir temperature; and the maximum velocities increase with increase in capillary widths. The same three regions are observed as discussed earlier using analytical solution where there is a linear relation between decrease in maximum velocity at the center of the capillary and capillary width in pores larger than 50 nm. Also nonlinear behavior between pore width and

maximum velocity in pores in the range of 30 to 50 nm and linear behavior in pores less than 30 nm.

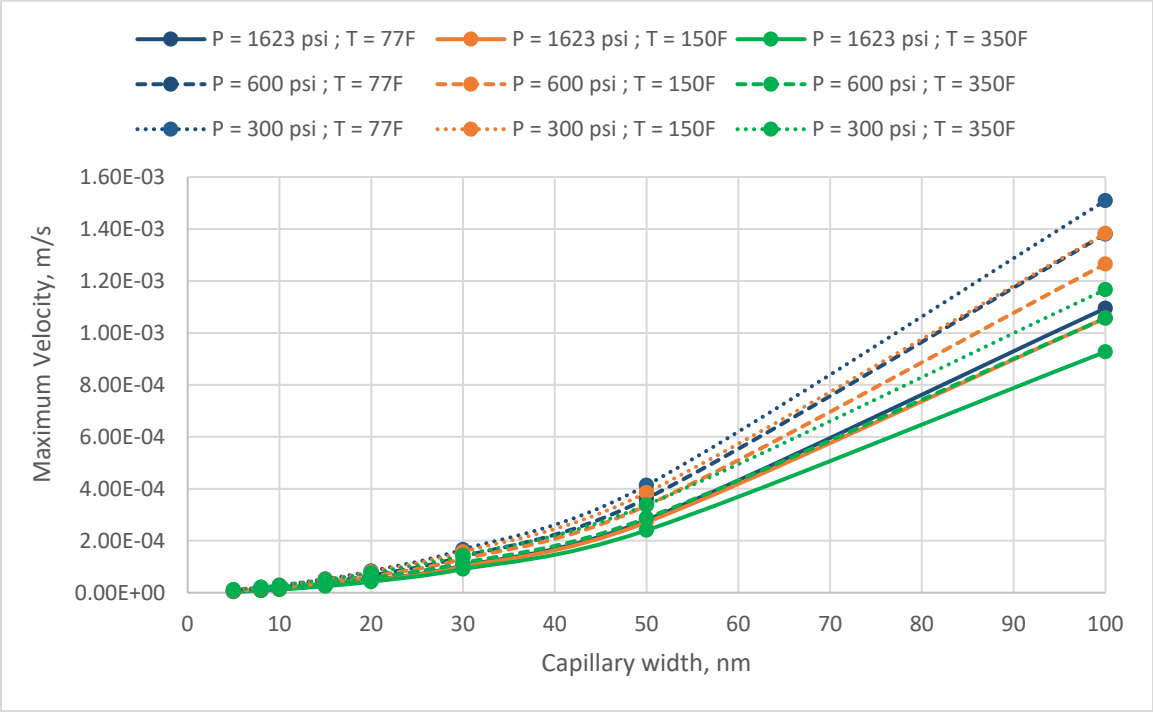

Figure 4-4: Plot displaying the maximum velocities of varying capillary widths from 5 nm to 100 nm using Klinkenberg slip flow equation at varying pore pressures and temperatures

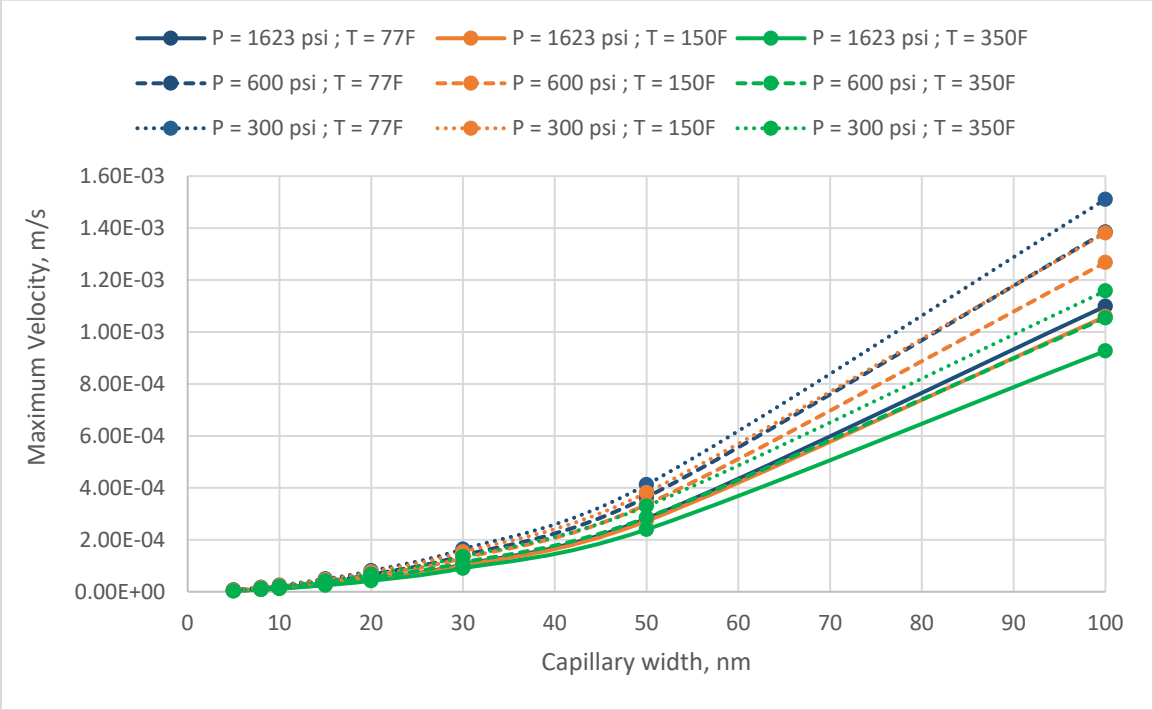

Figure 4-5: Plot displaying the maximum velocities of varying capillary widths from 5 nm to 100 nm using modified Klinkenberg slip flow equation at varying pore pressures and temperatures

To study the effect of slippage over different flow regimes based on fundamental equations, the wall velocity was calculated using Klinkenberg slippage equation Eq. (3-3) and the modified Klinkenberg slippage equation Eq. (3-7) plotted against the range of Knudsen numbers (Table 4-1) at different pore pressures and temperatures shown in Figure 4-6 and Figure 4-7 respectively. Observations are made for maximum velocity and wall velocity changes as a function of capillary width or Knudsen number, now using Klinkenberg or modified Klinkenberg equations Eq. (3-3) and Eq. (3-7). It is observed that as capillary width decreases (Knudsen number increases) the whole velocity including maximum velocity at the center of capillary and wall velocity adjacent to stationary wall decreases. Therefore, plotting wall velocity vs Knudsen number shows that as Knudsen number value increases i.e. at small capillary tubes the flow at wall reduces. Thus it is inferred that the wall velocity is captured only in larger capillaries (small Knudsen numbers) and at low pressures from Figure 4-6 and Figure 4-7. The effect of temperature and pressure on the wall velocity is explained in Figure 4-8.

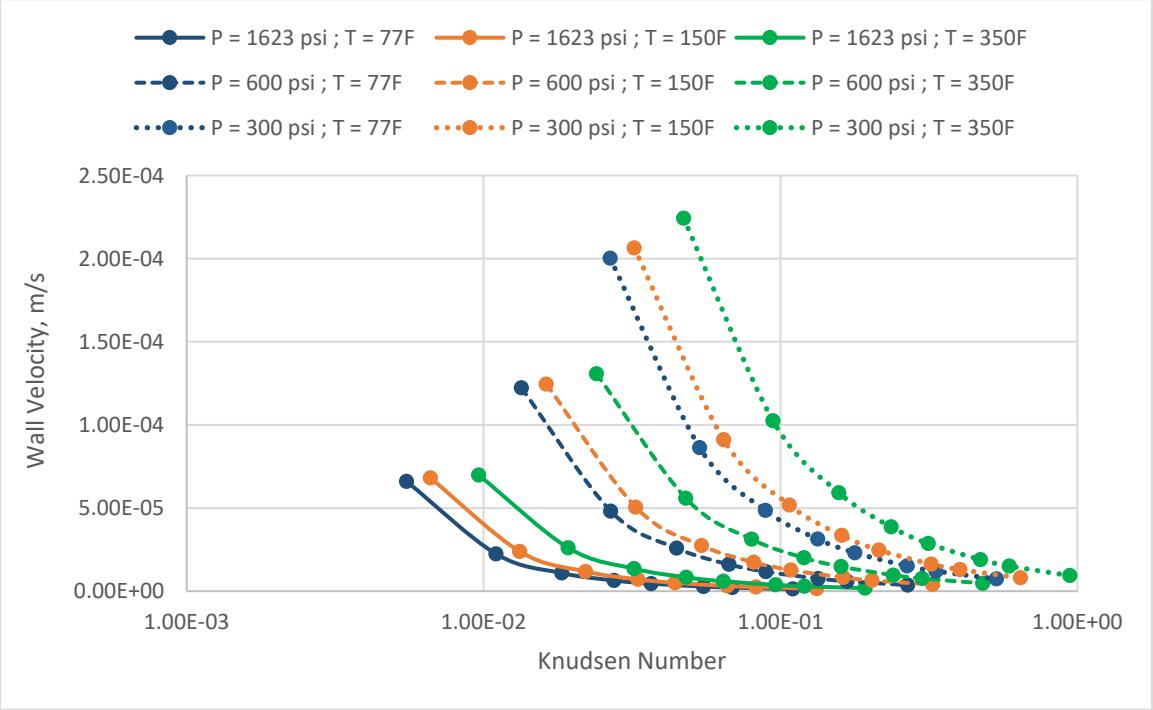

Figure 4-6: Plot displaying the wall velocities against Knudsen number using Klinkenberg slip flow equation at varying pore pressures and temperatures

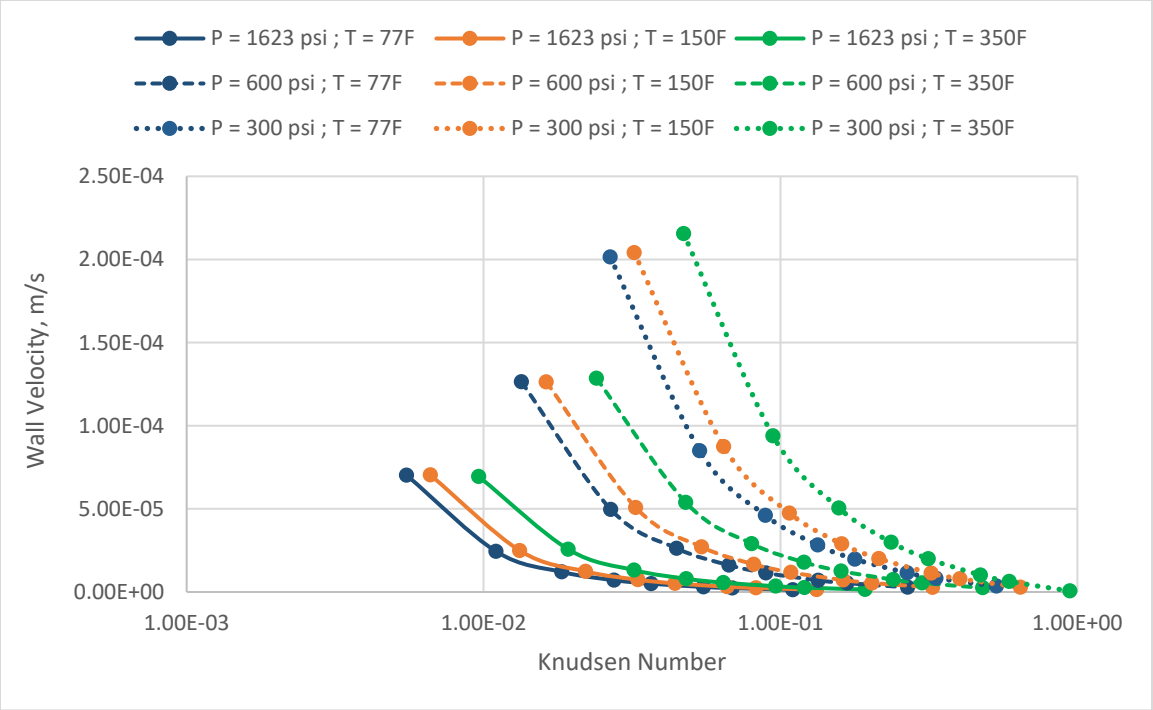

Figure 4-7: Plot displaying the wall velocities against Knudsen number using modified Klinkenberg slip flow equation at varying pore pressures and temperatures

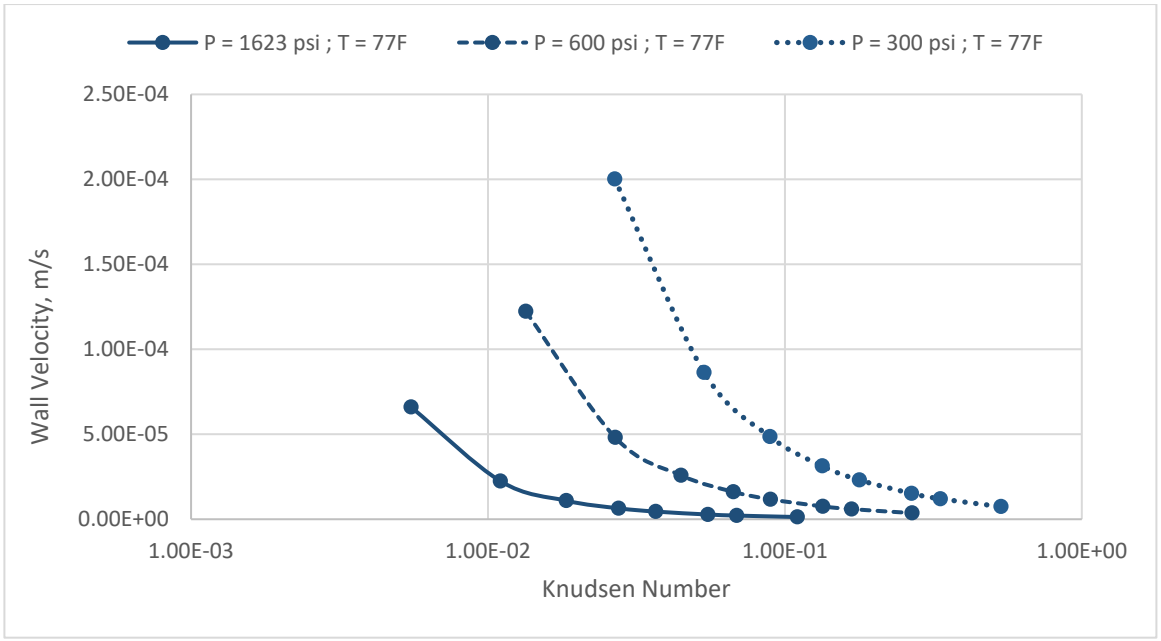

(a)

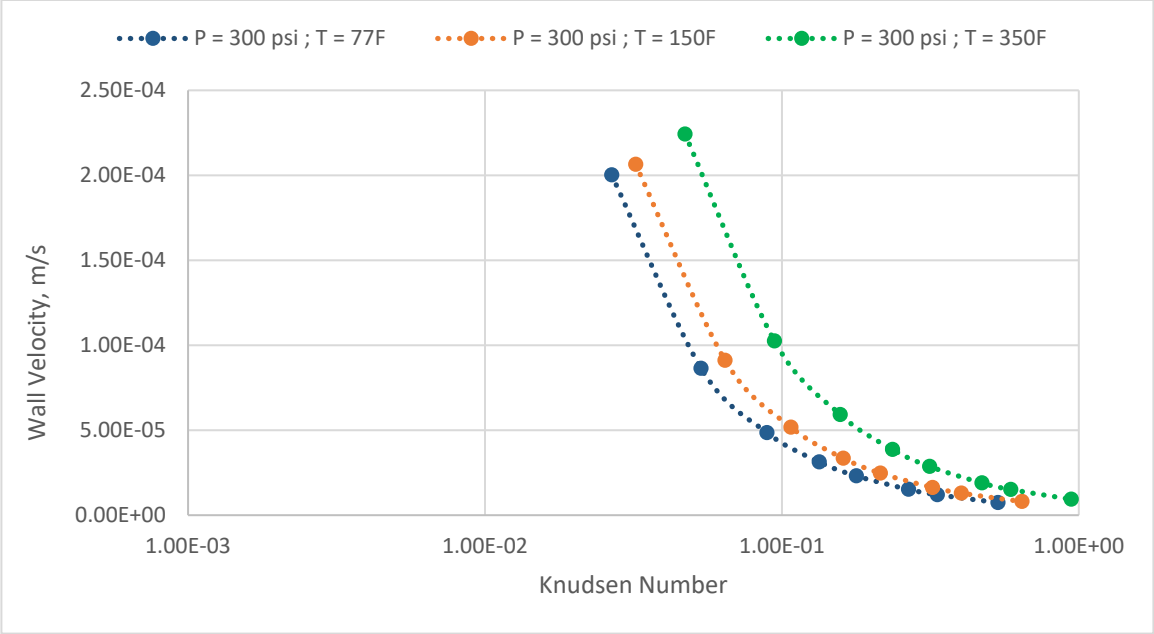

(b)

Figure 4-8: Plot displaying the wall velocities against Knudsen number using Klinkenberg slip flow equation at (a) constant temperature of 77F, (b) constant pore pressure of 300 psi

When studying the effect of pressure on wall velocity using Klinkenberg slip equation, it is found that the wall velocity increases with reduction in pressure. In this case the maximum wall velocity is captured at low pressures of 300 psi, and in slip flow regime as shown in Figure 4-8 (a). But as the flow moves to transition regime ($Kn > 0.1$), the wall velocities become negligeble. Similarly, considering the effect of temperature on wall velocity using Klinkenberg slip equation Figure 4-8 (b), it is found that the wall velocity have insignificant change with temperature.

Since the modified Klinkenberg equation Eq. (3-7) is valid only under the assumption of continuum flow, the wall velocities are compared at high pressure as the Knudsen numbers falls in the continuum and slip flow regimes. Figure 4-9 depicts the comparison between Klinkenberg slippage wall velocities and modified Klinkenberg slip flow wall velocities at a pressure of 1623 psi implying no difference between original Klinkenberg and modified Klinkenberg. However, when the comparison is plotted at a lower pressure of 300 psi, it is observed that the modified Klinkenberg slip flow wall velocities are lower to the Klinkenberg slippage wall velocities due to the Taylors series expansion incorporating the velocity gradient changes, as shown from Figure 4-10.

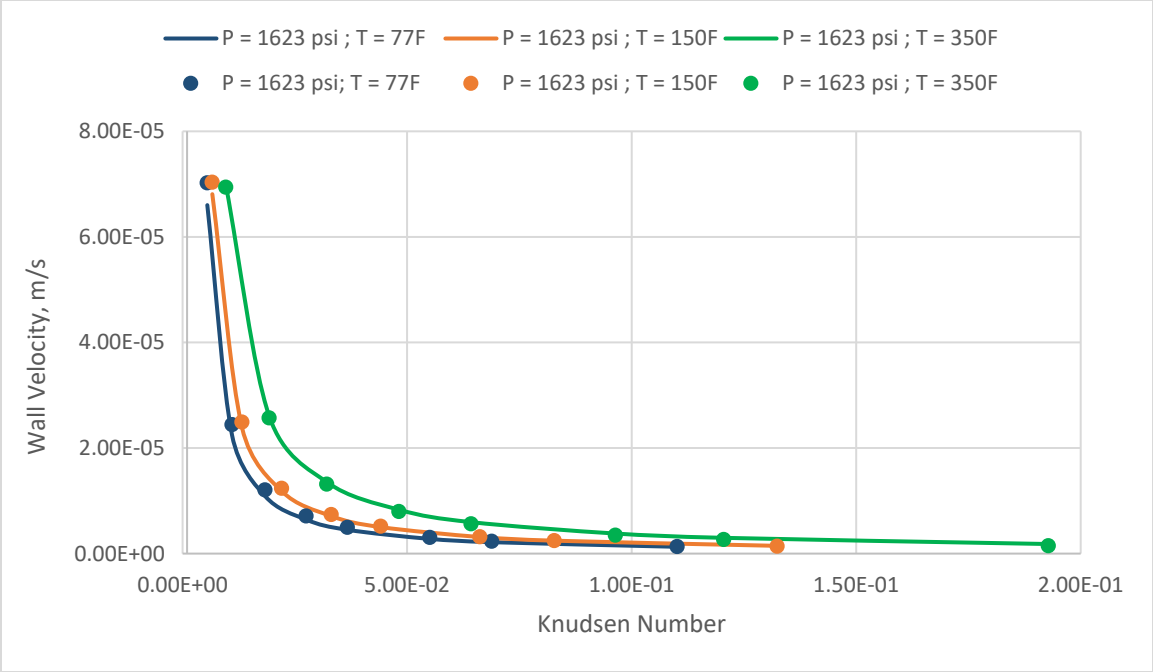

Figure 4-9: Plot displaying the comparison between Klinkenberg slip flow wall velocities (solid line) and modified Klinkenberg slip flow wall velocities (scatter points) at high pressure of 1623 psi, varying the reservoir temperature

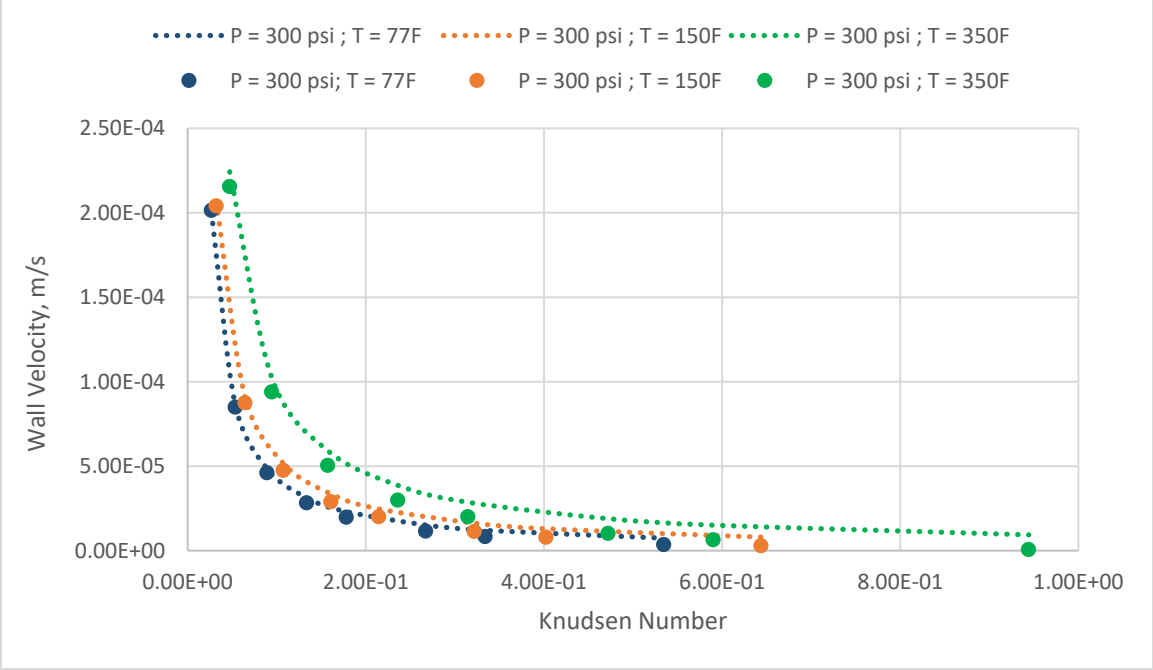

Figure 4-10: Plot displaying the comparison between Klinkenberg slip flow wall velocities (dotted line) and modified Klinkenberg slip flow wall velocities (scatter points) at low pressure of 300 psi, varying the reservoir temperature

From the original Klinkenberg and modified Klinkenberg slip flow equations, it is observed that the fluid flow including slippage is captured only for larger pores where the Knudsen number is in the continuum flow regime. When the capillary size reduces, and flow regime shift to slip and transient flow regimes, pore wall confinement or Knudsen diffusion effects cannot be captured. Therefore, in the next section we will study the fluid dynamics in nanopores using a Lattice Boltzmann model considering the methane gas flow in a straight capillary channel.

4.3. Numerical Solution - Lattice Boltzmann Model

The effects of pore confinement, gas slippage, surface diffusion and Knudsen diffusion mechanisms on non-ideal gas dynamics in various flow regimes is studied through a numerical simulation, designed for two-dimensional capillary tube where the gas flows between two parallel stationary walls flowing from north to south as shown in Figure 3-1.

The analytical solution, Klinkenberg slippage equation, and modified Klinkenberg slip flow equation demonstrates its validity for large pores where $Kn < 10^{-3}$ in the continuum flow regime. But as the pore width decreases, where the flow moves to slip and transition flow, the Knudsen number increases and the analytical solution does not hold good any longer. Using the LBM solution, high wall velocities are observed for smaller capillary widths depicting the presence of Knudsen diffusion, gas slippage, and wall confinement effect. These phenomenon are discussed in detail and results are presented in the followings chapters.

A capillary of dimension 100 nm by 200 nm, representing capillary width by length respectively is considered as our base case. Its corresponding dimensions in lattice units assigned are 50 lu by 100 lu. It is to be noticed that all the dimensions presented in this study are in the ratio of width by length. Some standard parameters considered in the numerical simulation are documented based on experiments performed on shale samples to capture the methane adsorption in kerogen by [4], listed in Table 3-1. Simulation results shown from Figure 4-11 until Figure 4-15 considers methane flow at atmospheric temperature of 25 C, initial pore pressure of 1623 psi.

Figure 4-11 illustrates the velocity profile in large pore capillary (100 nm width) in which single-phase single component methane gas is flowing downward. It is observed from the result that the flow through larger pores is in complete agreement with the analytical solution, and the surface diffusion is not prevalent when continuum flow exists, i.e., low Knudsen number. There is no wall

dominance or surface transport observed in the base case. The negative velocity shows the flow is downward.

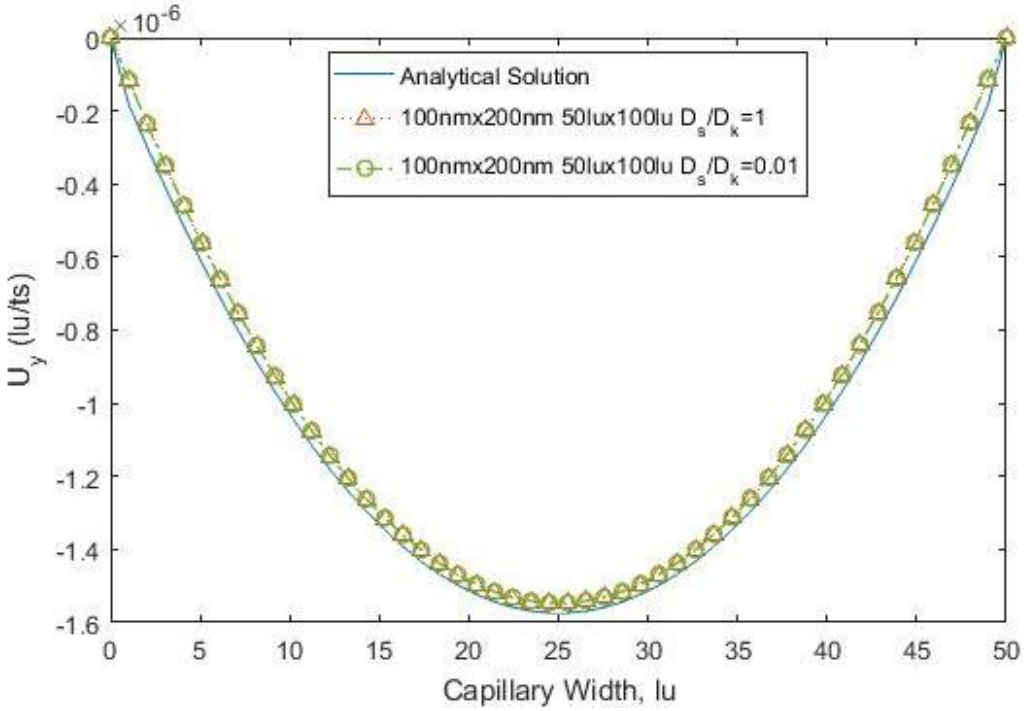

Figure 4-11: Numerical Simulation of a single capillary tube with large pore capillary size (in lattice units)

To make sure the gas velocity profiles are not being effected by the capillary length to width ratio, three different capillary lengths were chosen in the numerical solution and it was found that under different width to length ratios (W:L ratio in 1:2, 1:3, or 1:4), the velocity profile remained the same, in accordance with the analytical solution as expected and depicted in

Figure 4-12. The corresponding velocity profile in physical units was plotted in Figure 4-13. In lattice units the velocity was measured in the order of $10^{-6}\ lu/ts$ units, that is equivalent to $10^{5}\ nm/s$ in physical domain. This exercise has been conducted to ensure the stability of the numerical solutions at different width to length ratios.

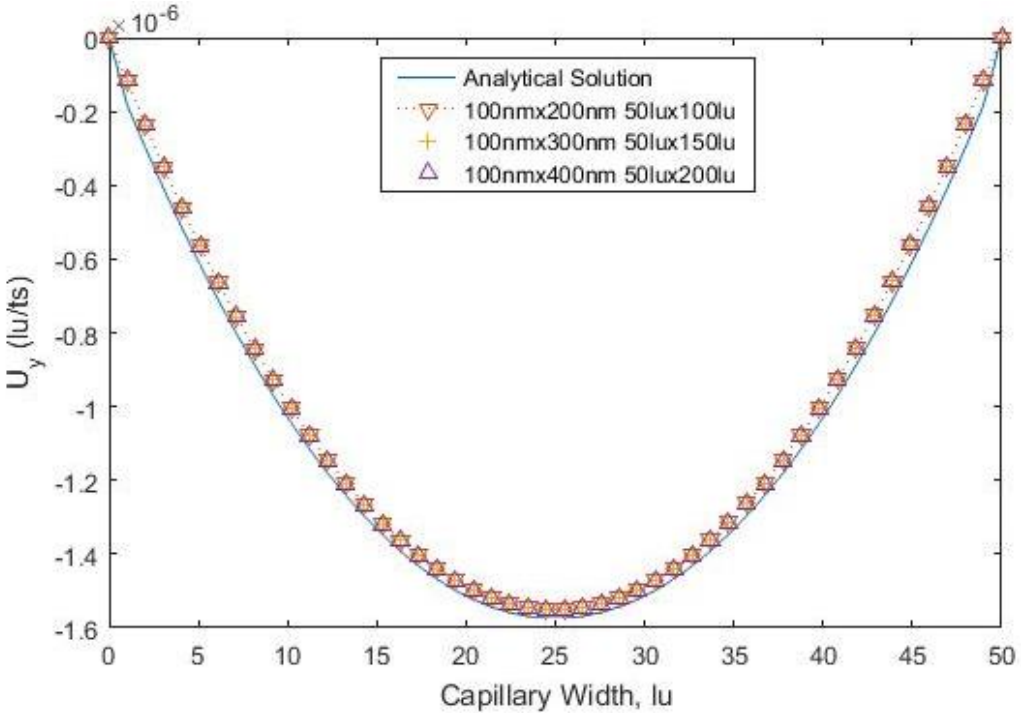

Figure 4-12: Numerical Simulation of a single capillary tube with varying capillary length sizes (in lattice units)

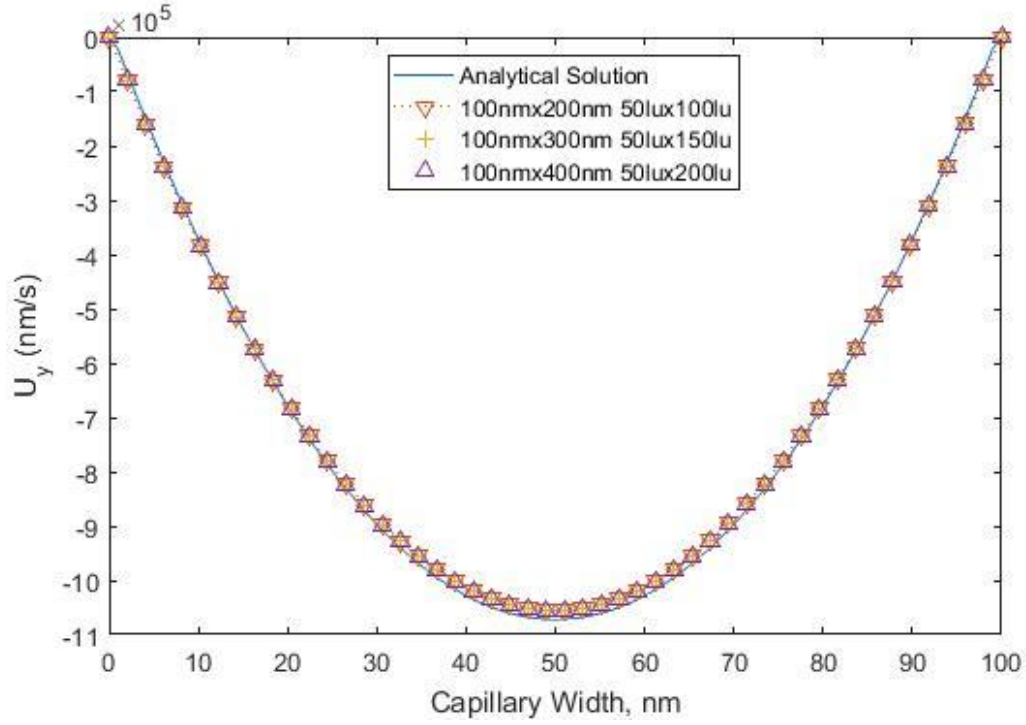

Figure 4-13: Numerical Simulation of a single capillary tube with varying capillary length sizes (in physical units)

Figure 4-13 represents the velocity profile in physical units which investigates the effect of capillary length. The result depicts that the results of the based case selected for this study (100 nm by 200 nm capillary) is not capillary length dependent as expected. A sample calculation is explained in detail in appendix describing the conversion from physical units to lattice units which were used in the numerical simulations.

The ideal gas equation has its equivalent of $RT = \frac{1}{3}$ in lattice units for D2Q9 model, where R is universal gas constant and T is the temperature. To correct the ideal gas assumption for real gas, the compressibility factor was introduced whose equivalent in lattice unit was introduced as an additional term Ψ, interaction potential function Eq. (3-23). This correction involves arbitrary constants ρ_0, and interaction potential- G [9] Eq. (3-22) which are calculated by history matching the pressure/density curve of real gas methane with one obtained from LBM model with lattice width size of 50 lu, borrowed from the work done by Fathi et. al[8]. Changing the lattice width from 50 lu to either of 40 lu, 45 lu, or 60 lu will result in change in arbitrary constants-ρ_0, G therefore developing deviated velocity profiles from analytical solution. While running this simulation, it is critical to have square lattices which is the basis to the D2Q9 model otherwise corrections to the velocity of different lattice nodes are required.

To study the sensitivity analysis of capillary width, the 100 nm width is reduced to 20 nm and 10 nm widths equivalent to 50 lu each. It is observed that as the capillary width is decreased the wall confinement effect and slippage is observed leading to non-zero wall velocity of $1.5 \times 10^5 nm/s$ and $2.5 \times 10^5 nm/s$ in 20 and 10 nm capillaries as shown in Figure 4-14 and Figure 4-15. The results also accounts to demonstrate the effect of changing capillary width to length ratios in smaller pores as discussed earlier in

Figure 4-12, here the width to length ratio ranges from 1:2, 1:4 to 1:10 ratios (this confirms that the capillary length of 40 nm is sufficient to develop a steady state velocity profile).

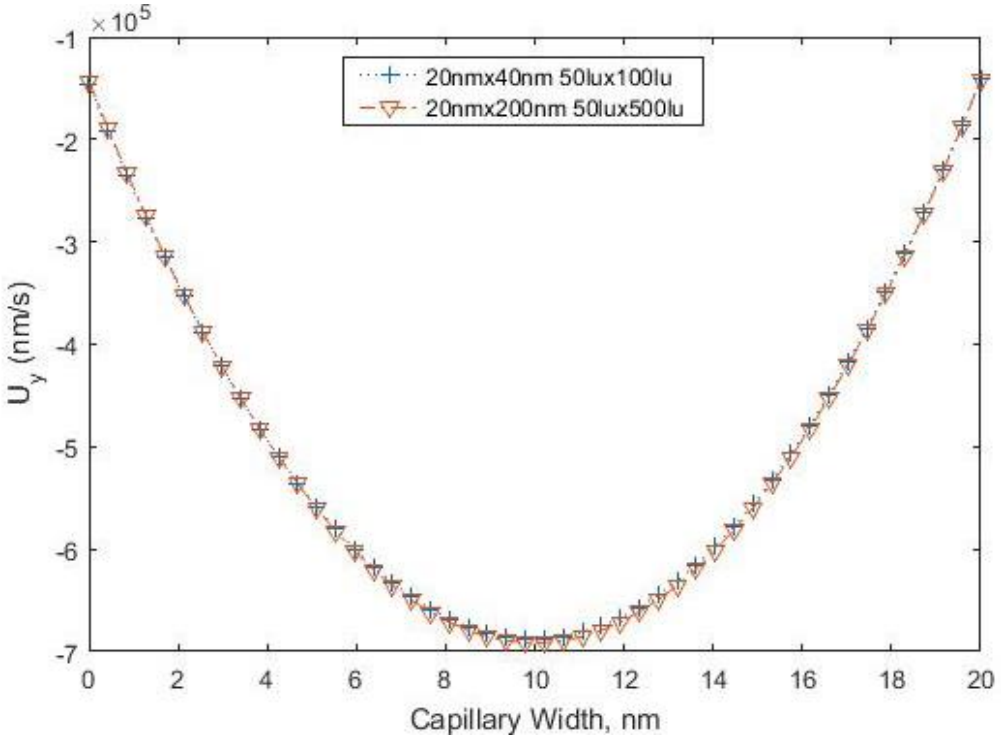

Figure 4-14: Numerical Simulation of a 20nm capillary tube with varying capillary length (in physical units) wall velocity = -1.432e+05 nm/s

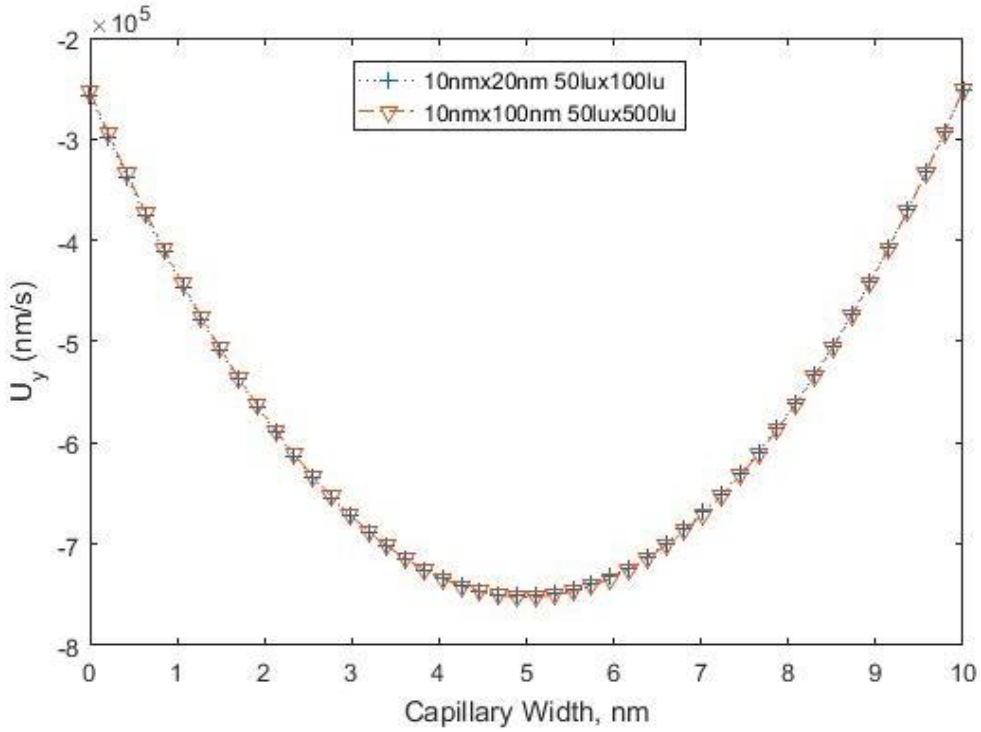

Figure 4-15: Numerical Simulation of a 10nm capillary tube with varying capillary length (in physical units) wall velocity = -2.528e+05 nm/s

As we go forward, using the LBM simulation, the gas behavior is studied across capillary widths ranging from 100 nm to 5 nm, the pore pressure and reservoir temperature is altered between 1623 psi, 600 psi, 300 psi and 77F, 150F, 350F respectively to consider the effects of pressure and temperature on non-ideal gas dynamics.

Traditionally from the fundamentals of fluid dynamics, we know that, with the reduction in capillary pore width the permeability of the capillary decreases resulting in decrease in flow rate and hence the velocity. However, using the LBM simulation it was observed that this trend of velocity profile shows an anomaly from the expected when studying fluid flow in nano-capillary widths. The results indicate the presence of high wall velocity being comparable to the maximum center velocity due to the presence of wall confinement, slippage, and Knudsen diffusion at the solid wall.

As the solid wall is a stationary wall, there is no velocity calculated at that position. The velocity of wall refers to the velocity one mean free path away from the wall. This region in large capillaries has much smaller velocity than the velocity away from the wall (center), thus in large capillaries the wall velocity is incomparable and can be neglected. But as the capillary size decreases to nano-scale, the wall velocity becomes comparable to the velocity at the center of the capillary.

On a broad scale, the outcome from results Figure 4-16 to Figure 4-24 show that as the temperature increases, pore pressure reduces, and capillary pore widths decreases (higher Knudsen number) the gas slippage and as discussed earlier by Fathi et al 2012[1] double slippage dominates resulting in higher velocity in nano-capillaries compare to what predicted by analytical solutions, Klinkenberg slippage theory and extensions of Klinkenberg equations.

At every specific capillary conditions (pressure and temperature), a critical Knudsen number exists which alters the flow pattern i.e. as the capillary pore reduces, it is expected that the velocity at the center of the tube also reduces, but at certain Knudsen number/pore width the velocity at the center starts increasing showing the double slippage effect [1]. Double slippage in addition to the momentum carried from bulk fluid to the wall accounts for the momentum carried by bouncing back molecules from the wall to the bulk fluid.

From definition, Knudsen number is a function of mean free path and the characteristic pore width. Mean free path is defined as the average colliding distance between two gas molecules which alters the molecule direction. This colliding distance depends on type of the gas, pressure, and temperature in the capillary pore. In larger capillary pores, the mean free path is very small where no collisions takes place between gas molecules and capillary solid wall, therefore a layer of stationary molecules prevails on the pore wall which leads to zero wall velocity. But at smaller pore size (low permeability), the mean free path becomes comparable to the capillary width, inducing molecules to collide unceasingly within the bulk and with the pore wall resulting in higher velocity across the capillary width. This increase in velocity is called gas slippage or double slippage, which is predominant at low pressures and when Knudsen number is large i.e. in the slip and transition flow regimes.

The next figures are conducted to show the existence of a critical pore width which alters the velocity flow profile with varying pore pressure and temperatures. Figure 4-16 through Figure 4-18 are the velocity profiles of capillary widths ranging from 100 nm to 5 nm at high pore pressure of 1623 psi and varying temperature. The velocities are in the range of $10^{-6}\ lu/ts$

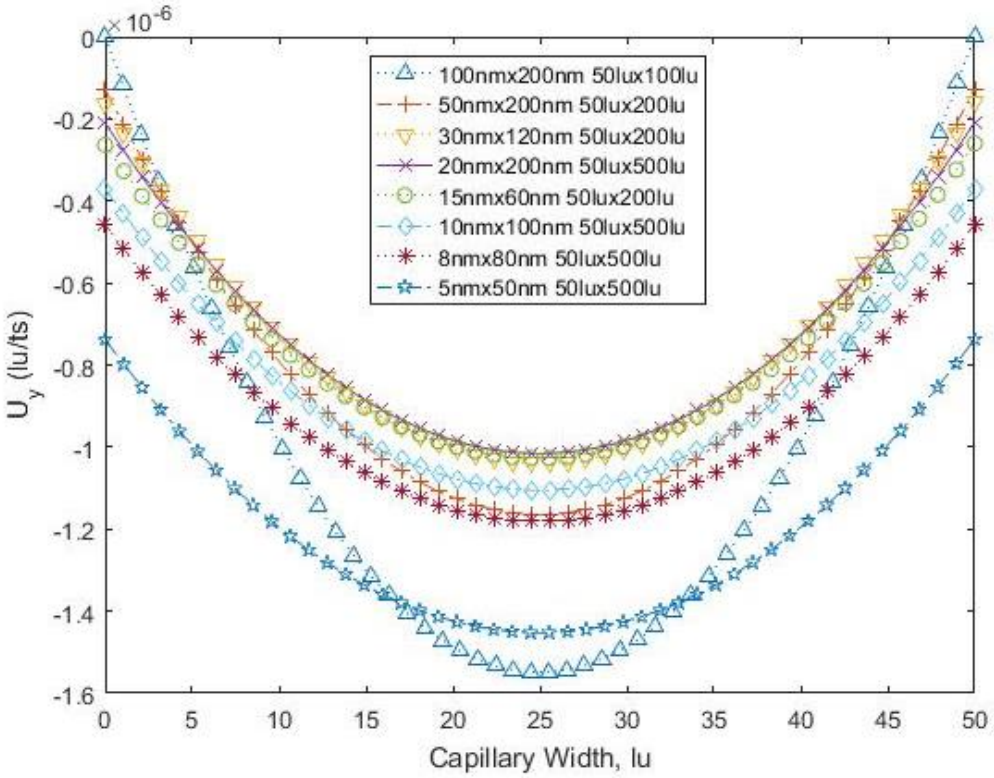

Figure 4-16: Velocity Profile of reducing capillary widths (100nm to 5 nm) (in lattice unit) (Pp=1623 psi T = 77F)

Figure 4-16 shows the LBM simulations being conducted at pore pressure of 1623 psi and temperature 77F with varying capillary widths from 100 nm to 5 nm. It is observed that as the capillary width decreases the wall velocity increases as suggested by Klinkenberg slippage theory, while the overall velocity profile decreases. However, there is a critical capillary width and Knudsen number below which not only the wall velocity increases but the entire velocity profile increases due to the effect of double slippage. In this case, pressure and temperature (1623 psi and 77F), the critical capillary width is at 20 nm, reducing the capillary width from 20 nm below will lead in increased overall velocity such that at 5 nm the maximum capillary velocity becomes comparable with velocity in 100 nm capillary.

At the same pore pressure of 1623 psi, when the reservoir temperature is increased from 77F to 150F and 350F, the LBM simulation results (Figure 4-17 and Figure 4-18) show that with increase in reservoir temperature velocity profiles also increases which also leads to new critical capillary width of 30 nm at higher temperature (350F). This implies that as the temperature increases the wall dominance and double slippage effect becomes more pronounced. When comparing the velocity profiles across temperatures and considering the smallest capillary width of 5 nm it is

observed that the wall velocity($2.88 \times 10^{-6}\ lu/ts$) at 350F is more than three times the wall velocity($0.74 \times 10^{-6}\ lu/ts$) at 77F. This is due to the dependence of temperature on the mean free path, which leads to increased kinetic energy and momentum transfer near the wall.

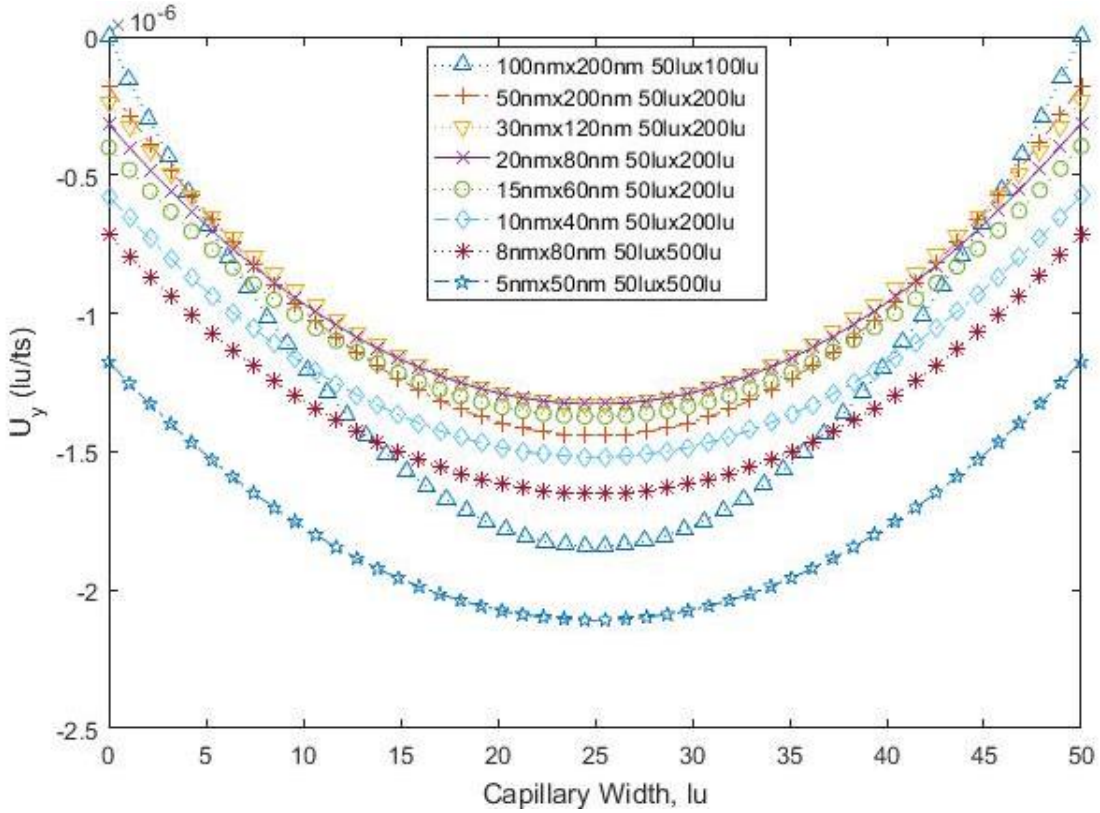

Figure 4-17: Velocity Profile of reducing capillary widths (100nm to 5 nm) (in lattice unit) (Pp=1623 psi T = 150F)

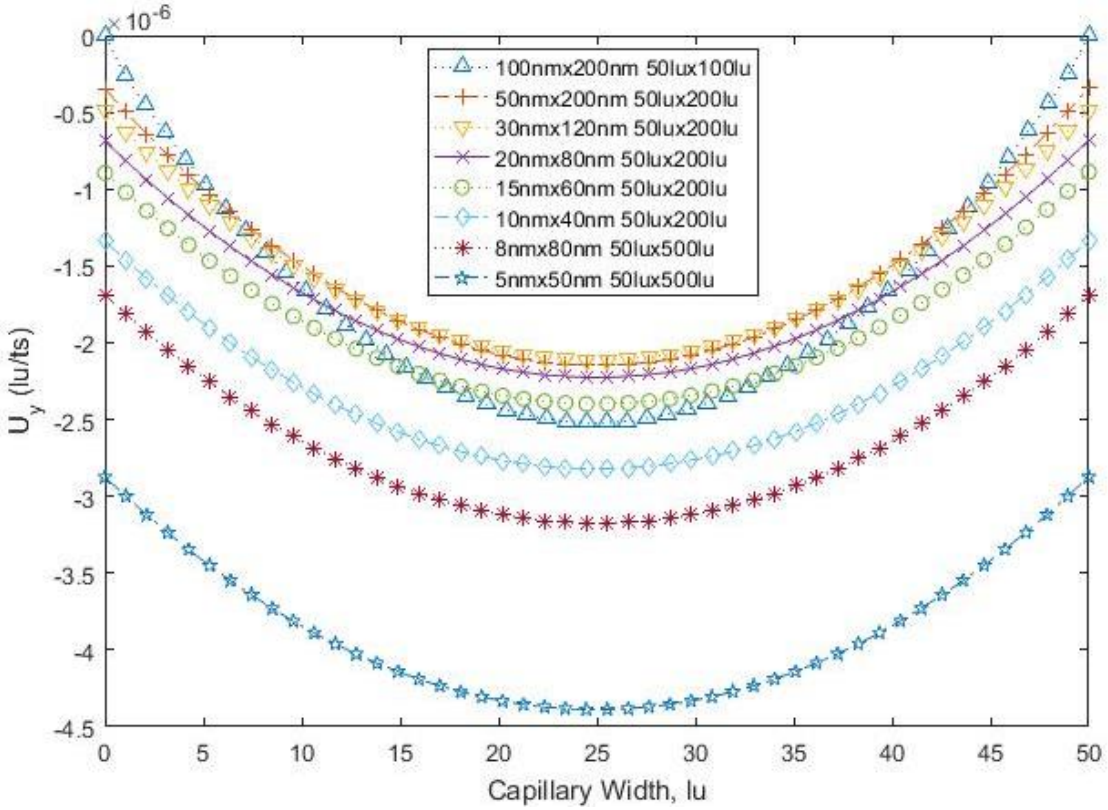

Figure 4-18: Velocity Profile of reducing capillary widths (100nm to 5 nm) (in lattice unit) (Pp=1623 psi T = 350F)

Advancing in studying the gas flow behavior in nanopores at reduced pressure of 600 psi, using the LBM numerical solution. Figure 4-19 through Figure 4-21 are the velocity profiles of capillary widths ranging from 100 nm to 5 nm at a reduced pore pressure of 600 psi with varying temperature. The velocities measured are in the range of $10^{-5}\ lu/ts$. This clearly indicates that as the pressure reduces to 600 psi, the velocities calculated are one order higher when compared to velocity at 1623 psi.

It is observed that as the pore pressure reduces, the double slippage effect is started to be seen at larger capillary tubes and the wall velocity become significant. Considering Figure 4-16 and Figure 4-19 where the temperature is 77F and the pore pressures are 1623 psi and 600 psi respectively. In the case of 1623 psi: with the decrease in capillary widths, the velocity profile surely increases in account of double slippage but doesn't exceed the maximum center velocity of 100 nm tube, whereas in the case of 600 psi: with the reduction in capillary widths, the 20 nm width velocity profile exceeds the 100 nm velocity profile because slip and transition flow regimes occur where effect of Knudsen diffusion and wall confinement is high along with double slippage.

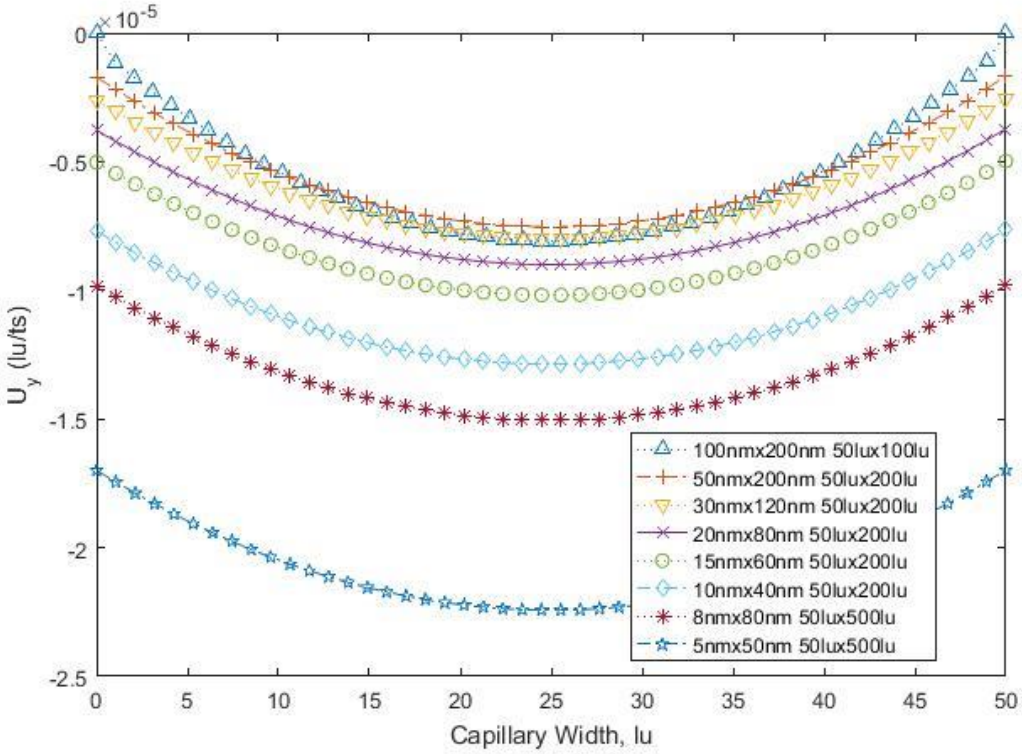

Figure 4-19: Velocity Profile of reducing capillary widths (100nm to 5 nm) (in lattice unit) (Pp=600 psi T = 77F)

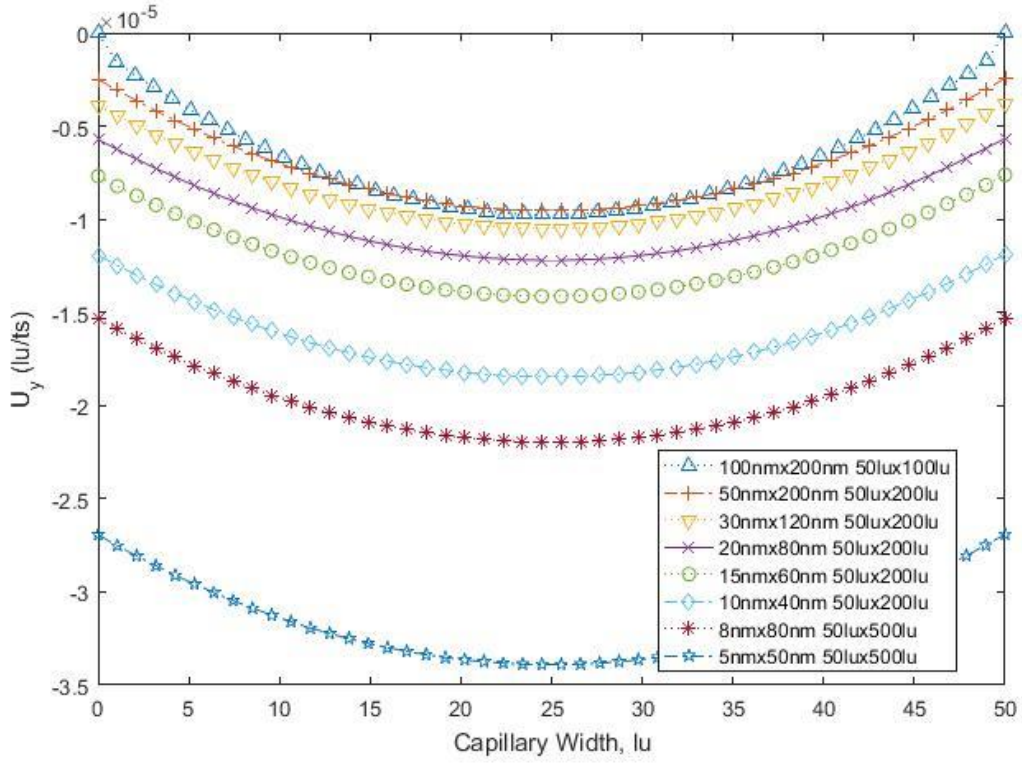

Figure 4-20: Velocity Profile of reducing capillary widths (100nm to 5 nm) (in lattice unit) (Pp=600 psi T = 150F)

Considering the temperature effects at 600 psi pore pressure: the critical pore width at 77F and 150F is noticed at 50 nm where the Klinkenberg slippage theory is identified i.e. with the reduction in capillary widths the wall velocity increases but the overall velocity profile decreases. Beyond the 50 nm capillary width, the velocity profile increases both at the wall and at the center due to the interaction of molecules at the walls and the momentum transfer to the bulk at the center. When the temperature is increased to 350F (Figure 4-21) at 600 psi, the velocity profile changes from parabolic velocity profile with slip velocity to more of a plug like velocity profile that shows the dominance of the wall confinement on non-ideal gas dynamics.

Examining the 5 nm velocity profile across the temperature changes, it is observed that the wall velocity ($6.73 \times 10^{-5}\ lu/ts$) at 350F is more than three times the wall velocity ($1.70 \times 10^{-5}\ lu/ts$) at 77F, also as observed for the higher 1623 psi pressure case. This is due to the dependence of temperature on the mean free path which leads to increased kinetic energy of momentum transfer near the wall.

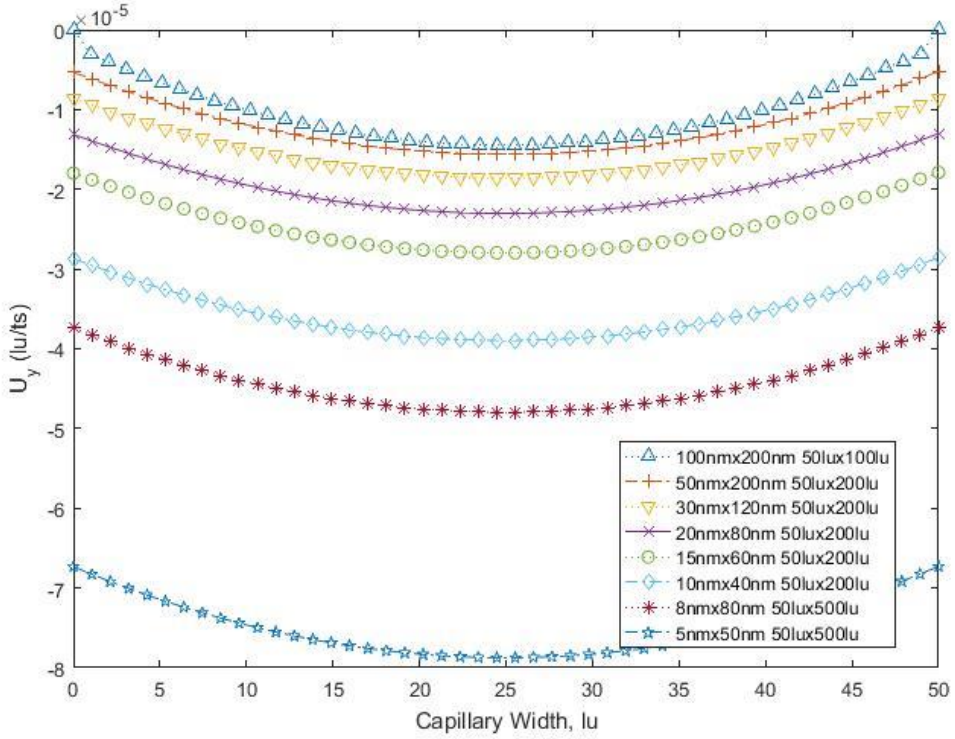

Figure 4-21: Velocity Profile of reducing capillary widths (100nm to 5 nm) (in lattice unit) (Pp=600 psi T = 350F)

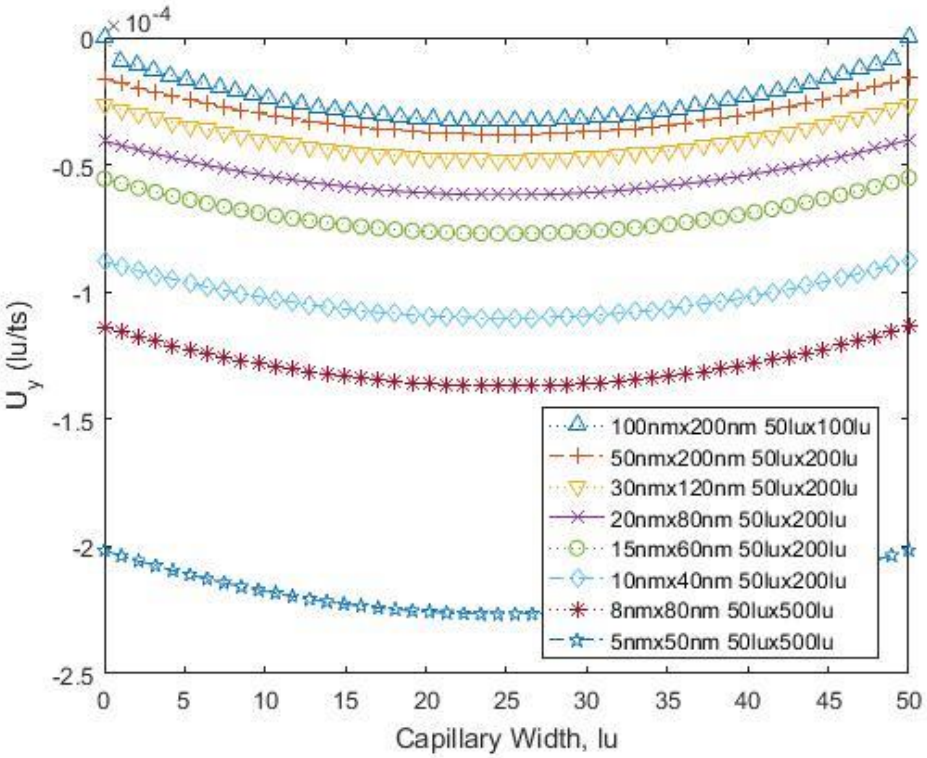

Figure 4-22: Velocity Profile of reducing capillary widths (100nm to 5 nm) (in lattice unit) (Pp=300 psi T = 77F)

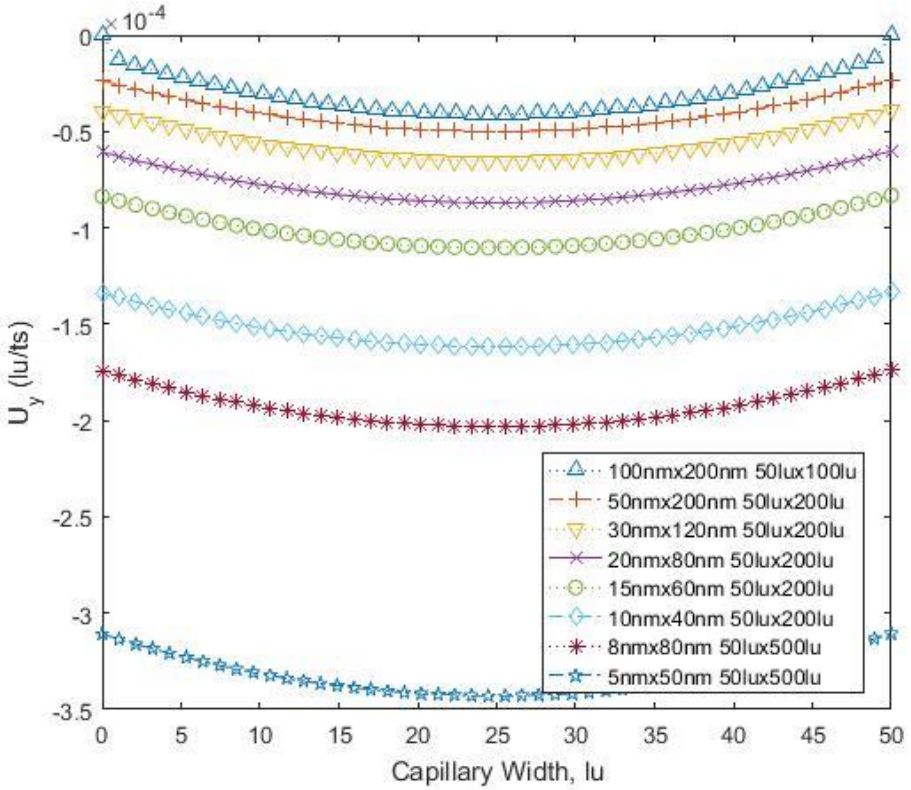

Figure 4-23: Velocity Profile of reducing capillary widths (100nm to 5 nm) (in lattice unit) (Pp=300 psi T = 150F)

Extending the LBM simulation model to study the gas flow behavior in nanopores at low pore pressure. Figure 4-22 through Figure 4-24 are the velocity profiles of capillary widths ranging from 100 nm to 5 nm at a reduced pore pressure of 300 psi with varying temperature. The velocities measured are in the range of $10^{-4}\ lu/ts$. This clearly indicates that as the pressure reduces to 300 psi, the velocities calculated are one order higher when compared to velocity at 600 psi, and two orders higher when compared to velocity at 1623 psi.

It is already understood from the previous simulation run at 600 psi that as the pore pressure reduces, the velocity profile increases as the double slippage effect is more prevalently detected at larger capillary tubes and the wall velocity become remarkable that the velocity profiles become non-parabolic (straight line profiles). Considering Figure 4-16, Figure 4-19 and Figure 4-22 where the temperature is 77F and the pore pressures are 1623 psi, 600 psi and 300 psi respectively. Although the case of 1623 psi and 600 psi were examined in the previous section where the Klinkenberg slippage theory was noticeable. However, with the further reduction of pressure to 300 psi, the wall dominance and double slippage became very evident that the capillary tubes smaller than 100 nm tend to have higher velocity profiles where majorly transition flow regime prevails (Table 4-1).

Investigating the temperature effects at 300 psi pore pressure: with the increase in temperature from 77F to 150F and 350F, the total velocity profile increases.

Examining the 5 nm velocity profile across the temperature changes, it is observed that the wall velocity($7.53 \times 10^{-4}\ lu/ts$) at 350F is more than three times the wall velocity($2.02 \times 10^{-4}\ lu/ts$) at 77F, also as observed for 1623 psi and 600 psi pressure case. This is due to the dependence of temperature on the mean free path which leads to increased kinetic energy of momentum transfer near the wall and eventually in the bulk called double slippage.

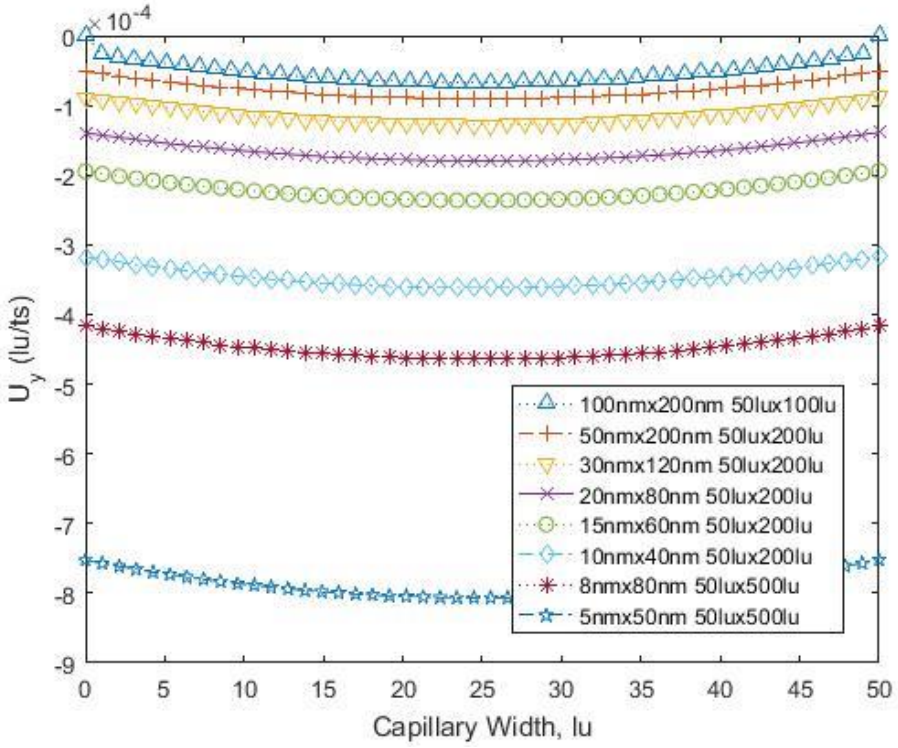

Figure 4-24: Velocity Profile of reducing capillary widths (100nm to 5 nm) (in lattice unit) (Pp=300 psi T = 350F)

Examining the 50 nm capillary pore width, Figure 4-25 displays the comparison between velocity profiles of Analytical solution and LBM simulation at pore pressure 1623 psi and various temperatures of 77F, 150F and 350F. To summarize, as the temperature increases, the velocity profiles of LBM numerical solution increase i.e. the velocity at the center of the tube increases from $1.16 \times 10^{-6}\ lu/ts$ to $1.44 \times 10^{-6}\ lu/ts$ and $2.15 \times 10^{-6}\ lu/ts$, and velocity at the walls increases from $0.13 \times 10^{-6}\ lu/ts$ to $0.18 \times 10^{-6}\ lu/ts$ and $0.35 \times 10^{-6}\ lu/ts$ for temperatures 77F, 150F and 350F respectively. LBM solution shows increased permeability with temperature due to the effect of Knudsen diffusion and double slippage (as explained in the earlier section), whereas the velocity profiles using the analytical solution keeps decreasing with increase in temperature having zero wall velocity.

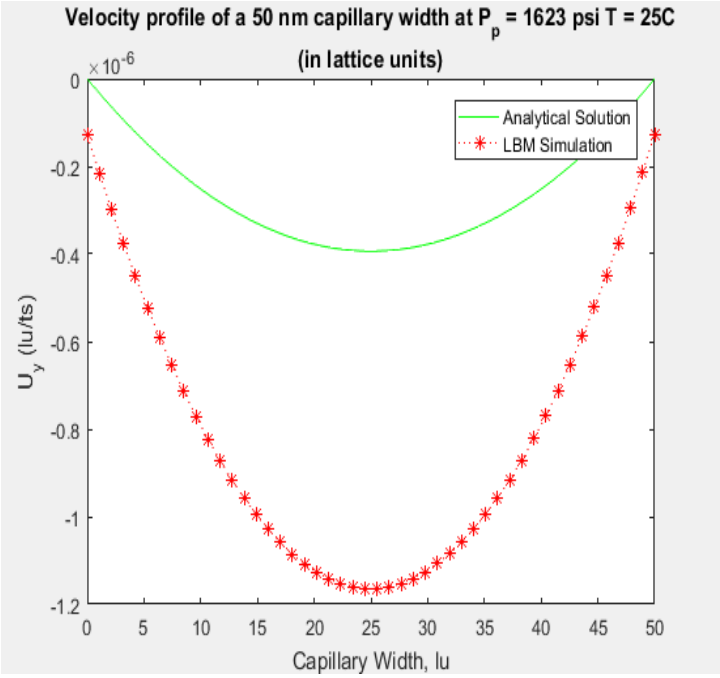

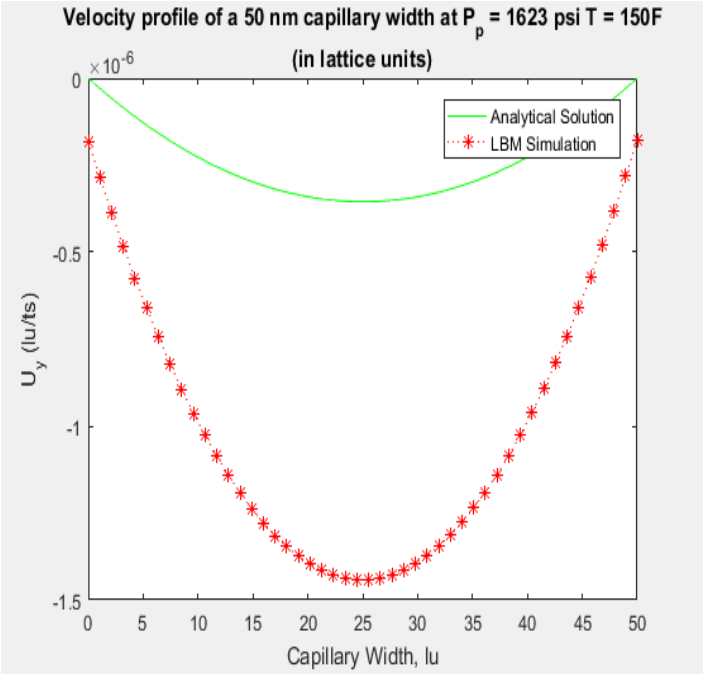

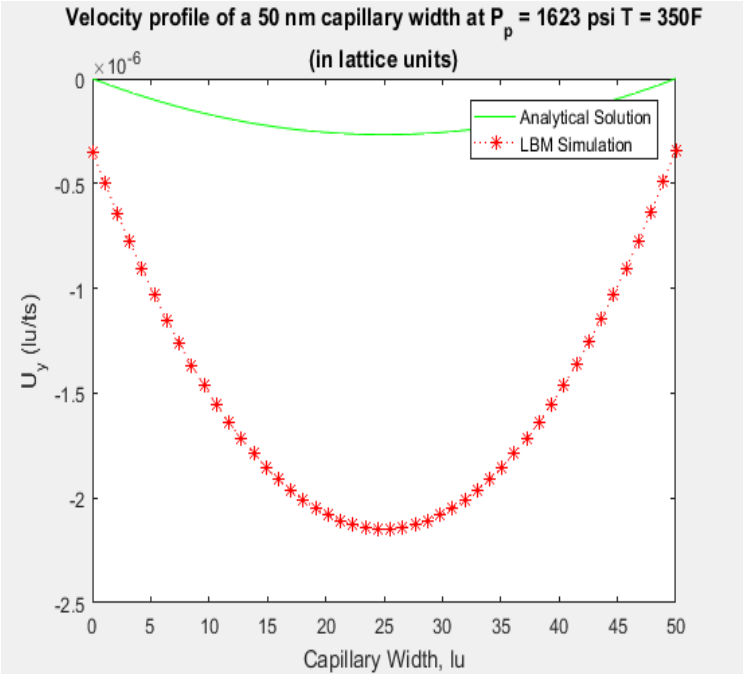

Figure 4-25: Velocity Profiles of 50 nm capillary widths at Pp=1623 psi and different temperatures of T = 77F, 150F and 350F respectively

4.3.1. LBM results in physical units

The next segment concentrates on the capillary center velocity and wall velocity for various capillary widths and flow regimes, mainly slip and transition flows, calculated using the LBM numerical solution in physical units.

At reservoir conditions- 1623 psi and 77F, from analytical solution and Klinkenberg results we knew that the maximum velocities are higher only in larger capillary tubes (low Knudsen number) and the maximum velocity decreases as the capillary width reduces (high Knudsen number), referring to Figure 4-2, Figure 4-4, Figure 4-5. But as the LBM solution incorporates the phenomenon of interactive adsorptive-cohesive forces in the fluid-solid, fluid-fluid molecules which brings into account the effects of Knudsen diffusion, double slippage and wall confinement as studied in previous section, the maximum velocity in the smaller capillary tubes is considerable and becomes more predominant when the temperature increases, refer Figure 4-26 (a). The increase in maximum velocity in smaller capillary tubes is because the mean free path of the capillary becomes higher (comparable to the width) thereby leading to numerous collisions occurring in this average distance resulting in higher velocity. Therefore, to summarize at higher pore pressure, as the temperature is increased and capillary width is reduced from 100 nm to 5 nm, the maximum velocity initially drops until a critical capillary width, after which the maximum velocity increases significantly with reduction in pore size shown in Figure 4-26 (a). This anomaly from the analytical solution is be attributed to the double slippage effect.

The same results of maximum velocity at 1623 psi are plotted against Knudsen number, refer to Figure 4-26 (b). Similar to the existence of critical capillary width, a critical Knudsen number exists. The larger capillary widths has a Knudsen number closer to the continuum flow region (beginning of slip flow regime) and thus the velocity profile observes a dip in maximum velocity with the increase in Knudsen number until a critical point, showing an inclination towards the analytical results. Above the critical Knudsen number, the maximum velocity value increases with increase in Knudsen number, moving towards slip and transition flow regimes, due to the molecular interaction and double slippage effect discussed earlier. Considering the smallest capillary width (5 nm): the maximum velocity at 350F ($3.67 \times 10^{-3} m/s$) is almost four times the maximum velocity at 77F ($0.99 \times 10^{-3} m/s$) ; considering the larger capillary width (100 nm): the maximum velocity at 350F ($2.11 \times 10^{-3} m/s$) is twice the maximum velocity at 77F ($1.05 \times$

$10^{-3} m/s$). This can be referred to the increased interaction between molecules at lower pressure and high temperature due to increased kinetic energy of the molecules.

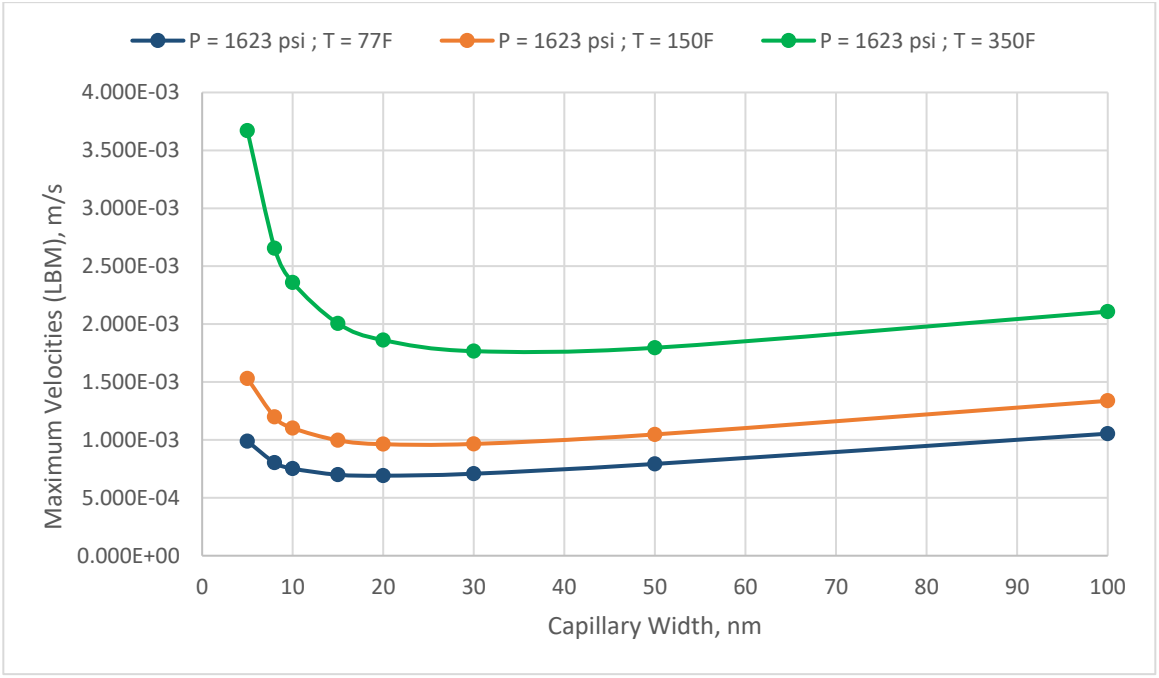

(a)

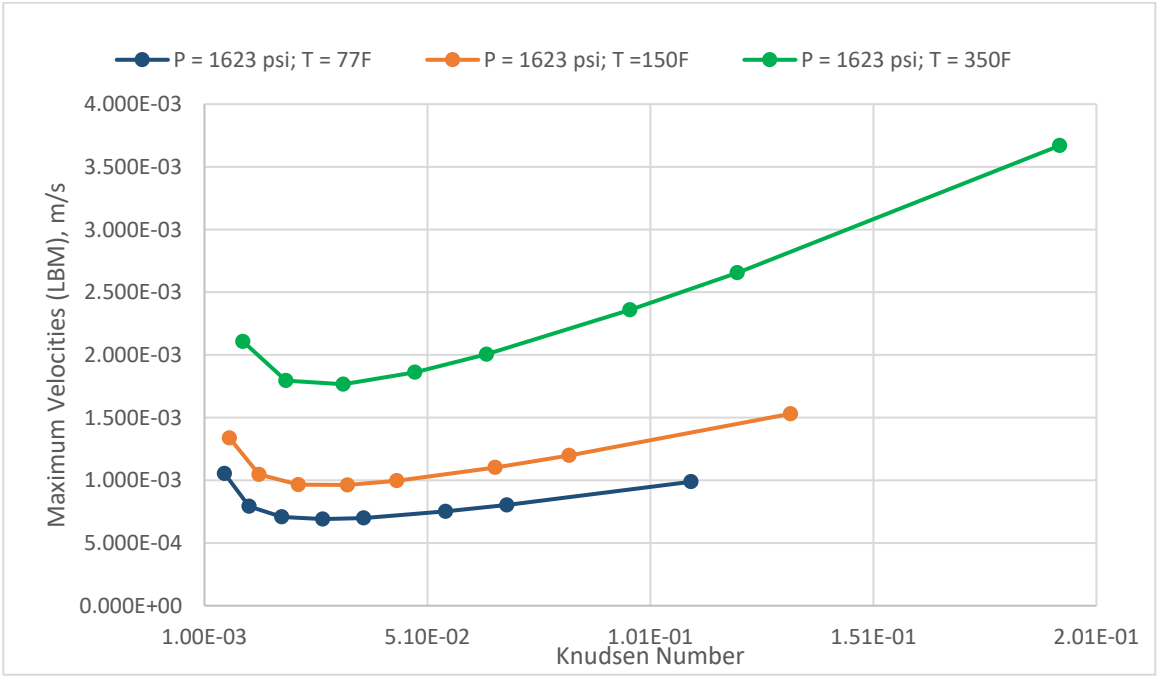

(b)

Figure 4-26: Plot displaying the maximum velocity at higher pore pressure of 1623 psi, varying temperature using LBM numerical solution against (a) capillary widths from 5 nm to 100 nm (b) Knudsen number

When the pore pressure drops to 600 psi, a critical point which was observed in 1623 psi case doesn't exist showing a linear fluid flow along the changes in capillary width/Knudsen number (Figure 4-27). With the decrease in pressure from 1623 psi to 600 psi, the maximum velocity increases by an order of magnitude 10 (in the range of $10^{-2}\ m/s$) compared with 1623 psi pressure ($10^{-3}\ m/s$).

Here, by lowering the capillary width or increasing the temperature, the maximum velocity increases as shown in Figure 4-27 (a). This shows an anomaly from the analytical solution, because the analytical solution is only valid in the continuum flow and does not hold good when the slip or transition flow regimes prevail.

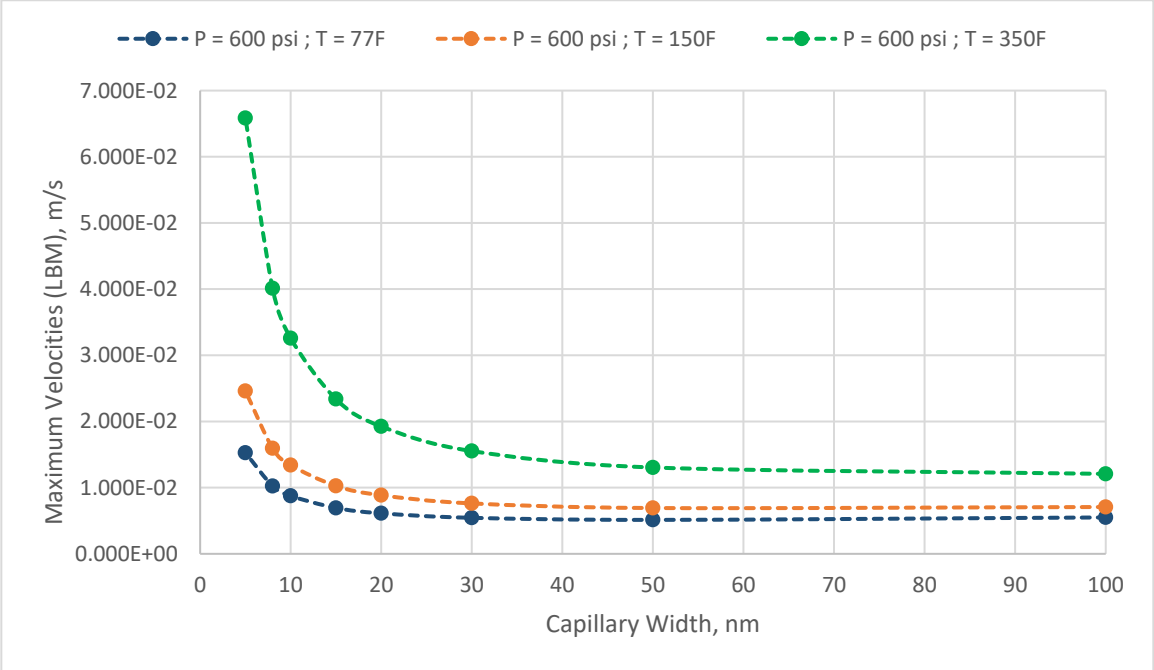

(a)

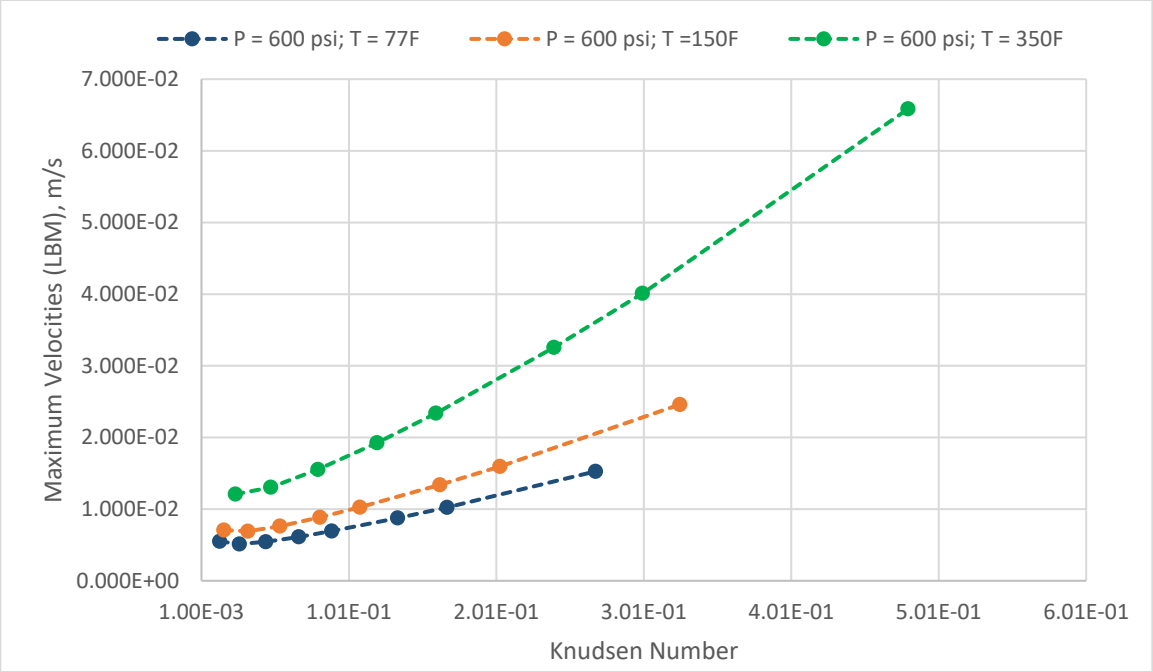

(b)

Figure 4-27: Plot displaying the maximum velocity at lower pore pressure of 600 psi, varying temperature using LBM numerical solution against (a) capillary widths from 5 nm to 100 nm (b) Knudsen number

At 600 psi pore pressure, the maximum velocity increases drastically as flow moves towards slip and transition regimes i.e. when Knudsen number becomes higher. As a general trend- as the temperature increases, lowering the capillary width, the Knudsen number increases and the maximum velocity also increases. Referring to Figure 4-27 (b), a linear trend is observed between the maximum velocity and Knudsen number. This linearity is obvious in the high Knudsen number region and at higher temperatures. Considering the smallest capillary width (5 nm): the maximum velocity at 350F ($5.63 \times 10^{-2} m/s$) is more than four times the maximum velocity at 77F ($1.16 \times 10^{-2} m/s$); considering the larger capillary width (100 nm): the maximum velocity at 350F ($1.21 \times 10^{-2} m/s$) is almost twice the maximum velocity at 77F ($0.55 \times 10^{-2} m/s$).

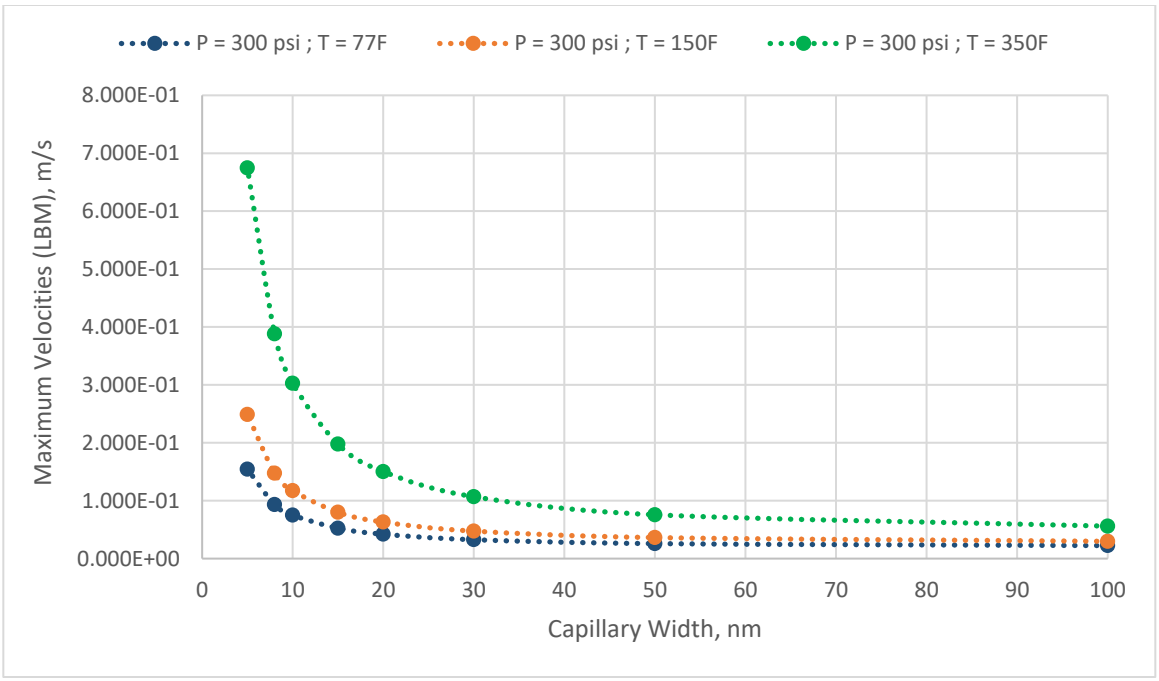

(a)

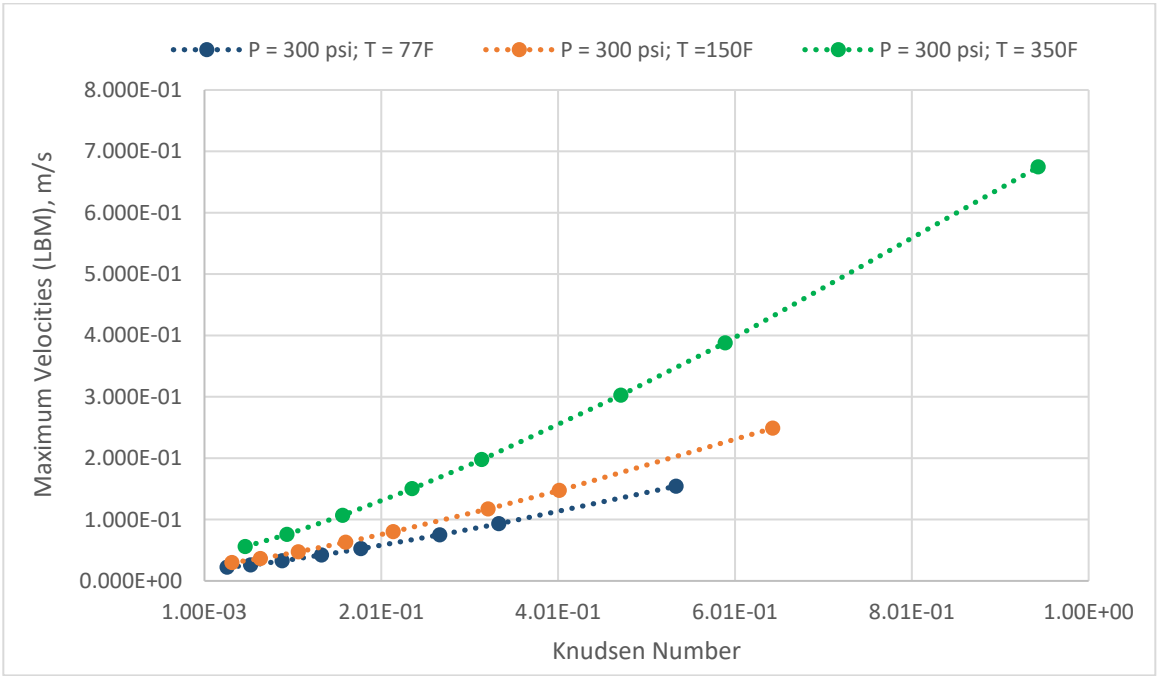

(b)

Figure 4-28: Plot displaying the maximum velocity at low pore pressure of 300 psi, varying temperature using LBM numerical solution against (a) capillary widths from 5 nm to 100 nm (b) Knudsen number

When the pore pressure further decreases to 300 psi, the maximum velocities increases in the range of $10^{-1}\ m/s$. With the decrease in capillary width or increasing the temperature, the maximum

velocity increases as shown in Figure 4-28 (a), reversing the flow i.e. 5 nm capillary having higher velocity than 100 nm. This deviated behavior from analytical solution is due to the presence of high molecular interactions leading to double slippage effects.

At 300 psi pore pressure, the maximum velocity increases drastically as flow moves towards transition regime i.e. when Knudsen number becomes higher (≈1). Referring to Figure 4-28 (b), a true linear trend is observed between the maximum velocity and Knudsen number. This linearity is clearly observed in the high Knudsen number region and at higher temperatures. Considering the smallest capillary width (5 nm): the maximum velocity at 350F ($6.75 \times 10^{-1} m/s$) is more than four times the maximum velocity at 77F ($1.54 \times 10^{-1} m/s$) ; considering the larger capillary width (100 nm): the maximum velocity at 350F ($5.6 \times 10^{-2} m/s$) is more than twice the maximum velocity at 77F ($2.24 \times 10^{-2} m/s$). This can be referred to the increased interaction between molecules at lower pressure and high temperature due to increased kinetic energy of the molecules.

Figure 4-29 is plotted to check the discrepancy between the analytical and LBM simulation results at different pressures and temperatures. It is noticed that highest abnormality is observed at low pore pressure and high temperature as the analytical solution is valid only in the continuum flow regime, it does not take account of the molecular interactions in the fluid, slippage effect near the walls and fails when Knudsen number becomes larger. The least abnormality is seen at high pore pressure and low temperature where the mean free path of molecules is relatively small to have higher interactions as compared to high temperatures.

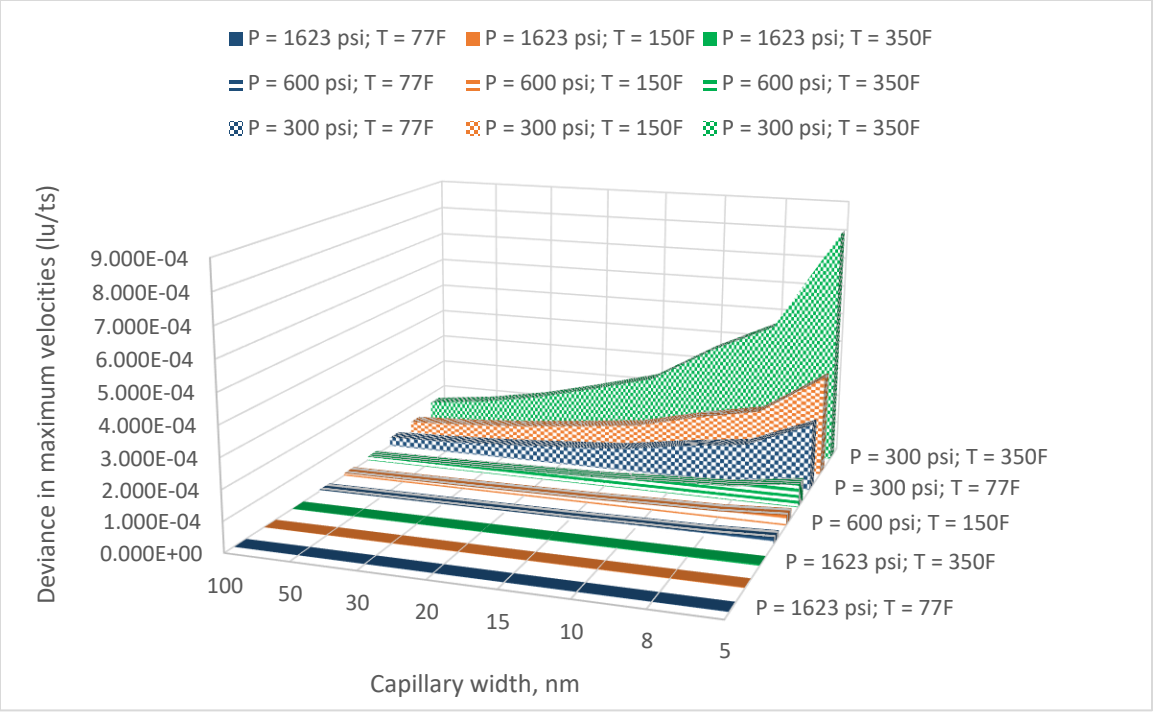

Figure 4-29: Deviance between Analytical and LBM numerical solution- maximum velocity with varying pore pressures and temperatures

Some general observations noted from comparing above analytical solution and LBM solution are stated below where the maximum velocity is a function of P_p, T, H pore pressure, temperature and capillary pore width respectively.

1. H - When capillary width is reduced

- Analytical Solution- Vmax reduces
- LBM Solution- as capillary width is reduced the Vmax initially drops until a critical capillary width, after which the Vmax increases significantly with reduction in pore size

2. T - When temperature is increases

- Analytical Solution- Vmax reduces
- LBM Solution- Vmax increases

3. P_p - When pressure is reduced

- Analytical Solution- Vmax increases
- LBM Solution- Vmax increases

As observed from above results that the significant increase in maximum velocity in smaller capillary tubes is due to the effect of double slippage, it is important to study the distribution of wall velocities across different flow regimes with the change in pressure and temperature. Similar to the maximum velocity, the wall velocities are also plotted against Knudsen number, as shown in Figure 4-30, Figure 4-31, and Figure 4-32. It is observed that the wall velocity also increases with decrease in pressure i.e. increases from range of $10^{-3}\ m/s$ to $10^{-1}\ m/s$ when pressure increases from 1623 psi to 300 psi respectively . At 1623 psi pore pressure, majority of flow regime seen is slip flow; at 600 psi pressure slip and transition flow regimes are observed; and at 300 psi pressure majority of transition flow regime is seen. When the flow is in slip regime, the wall velocities are fairly low; but as the flow shifts into transition regime, the wall velocities become higher showing the influence of wall dominance.

With the increase in temperature, the wall velocity increases and at higher temperatures of 350F, highest wall velocity is observed. Considering the wall velocity distribution at 1623 psi and comparing the velocity profiles across temperatures (Figure 4-30): for 5 nm it is observed that the wall velocity at 350F ($2.4 \times 10^{-3} m/s$) is more than four times the wall velocity at 77F ($0.503 \times 10^{-3}\ m/s$). This is due to the dependence of temperature on the mean free path which leads to increased kinetic energy of momentum transfer near the wall. At low temperature of 77F, there is no wall velocity observed in the larger capillary tube (100 nm) as continuum flow still prevails and the analytical solution is still valid. However, as the temperature increases to 350F, a low wall velocity is observed ($4.6 \times 10^{-5}\ m/s$) as slip flow regime comes into play.

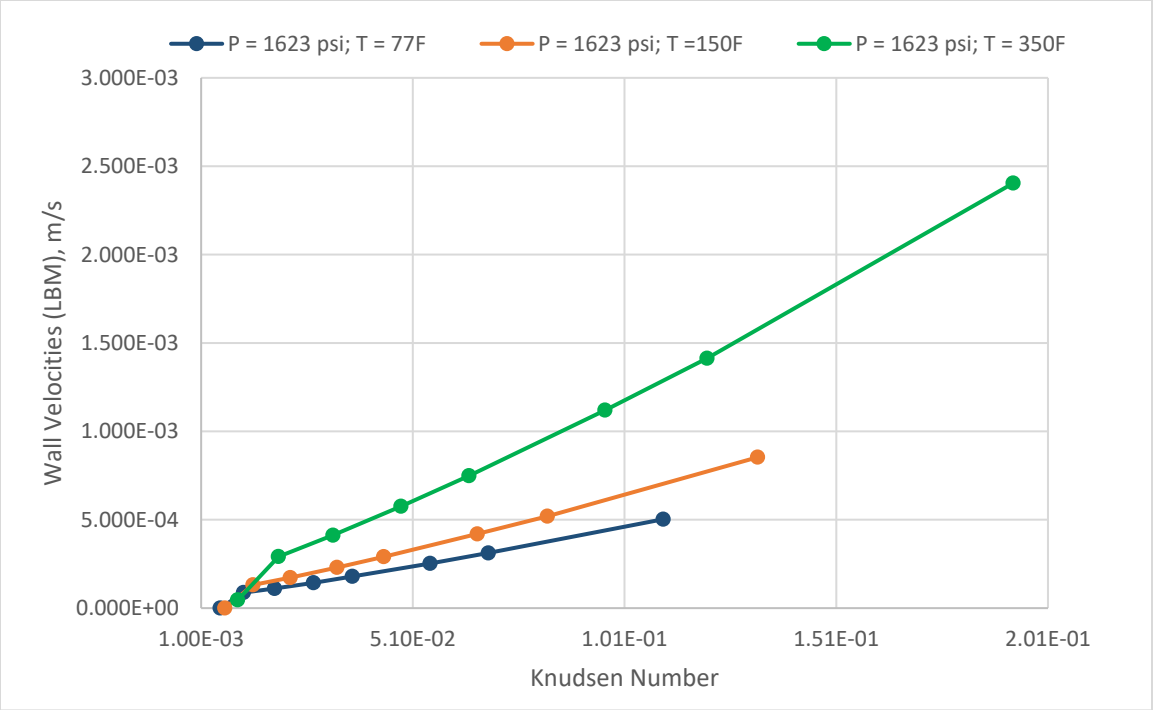

Figure 4-30: Plot displaying the wall velocity at high pore pressure of 1623 psi, varying temperature using LBM numerical solution against Knudsen number

Examining the velocity profile at 600 psi across the temperature (Figure 4-31): for 5 nm, it is observed that the magnitude increase in wall velocity at 350F ($5.63 \times 10^{-2}\ m/s$) is more than four times the wall velocity at 77F ($1.16 \times 10^{-2}\ m/s$), also as observed for the higher 1623 psi pressure case. For 100 nm, the wall velocity at 350F ($1.41 \times 10^{-3}\ m/s$) is four times the wall velocity at 77F ($0.34 \times 10^{-3}\ m/s$). Next, studying the velocity profile at 300 psi across the temperature (Figure 4-32): for 5 nm, it is observed that the magnitude increase in wall velocity at 350F ($6.3 \times 10^{-1}\ m/s$) is more than four times the wall velocity at 77F ($1.38 \times 10^{-1}\ m/s$). For 100 nm, the wall velocity at 350F ($2.08 \times 10^{-2}\ m/s$) is almost four times the wall velocity at 77F ($0.54 \times 10^{-2}\ m/s$). This increased wall velocities at high temperature and larger Knudsen numbers is due to the increased momentum transfer (as molecules collide with higher kinetic energies near the wall with increased temperature).

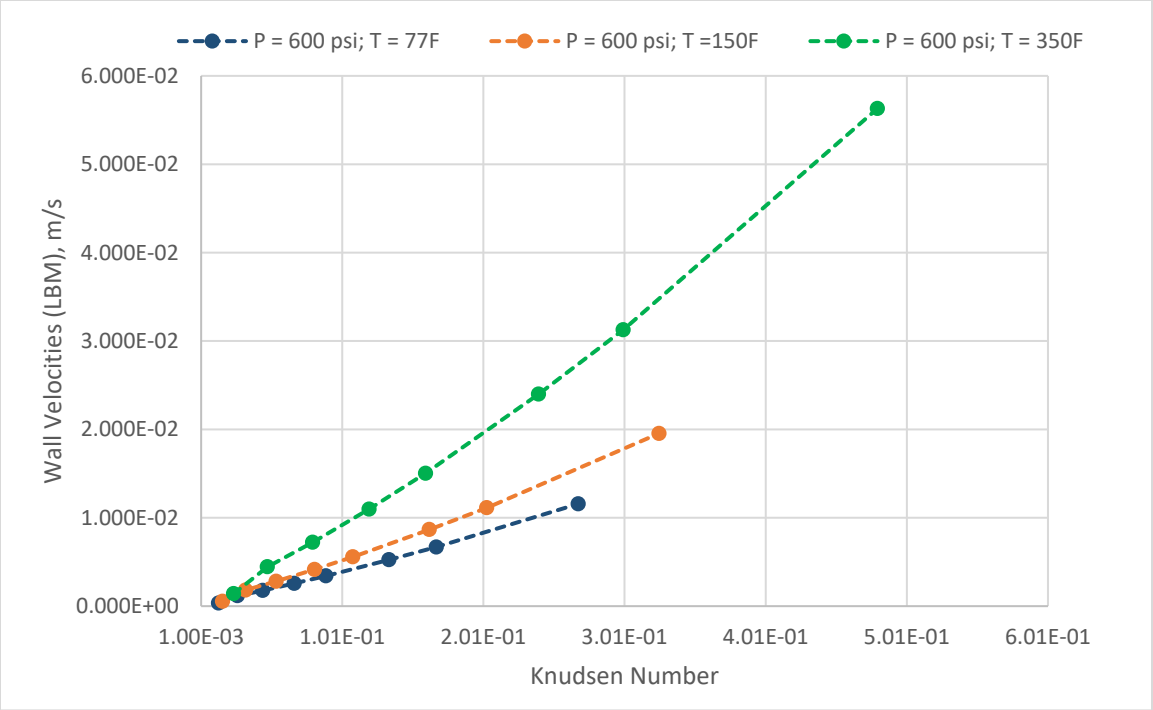

Figure 4-31: Plot displaying the wall velocity at lower pore pressure of 600 psi, varying temperature using LBM numerical solution against Knudsen number

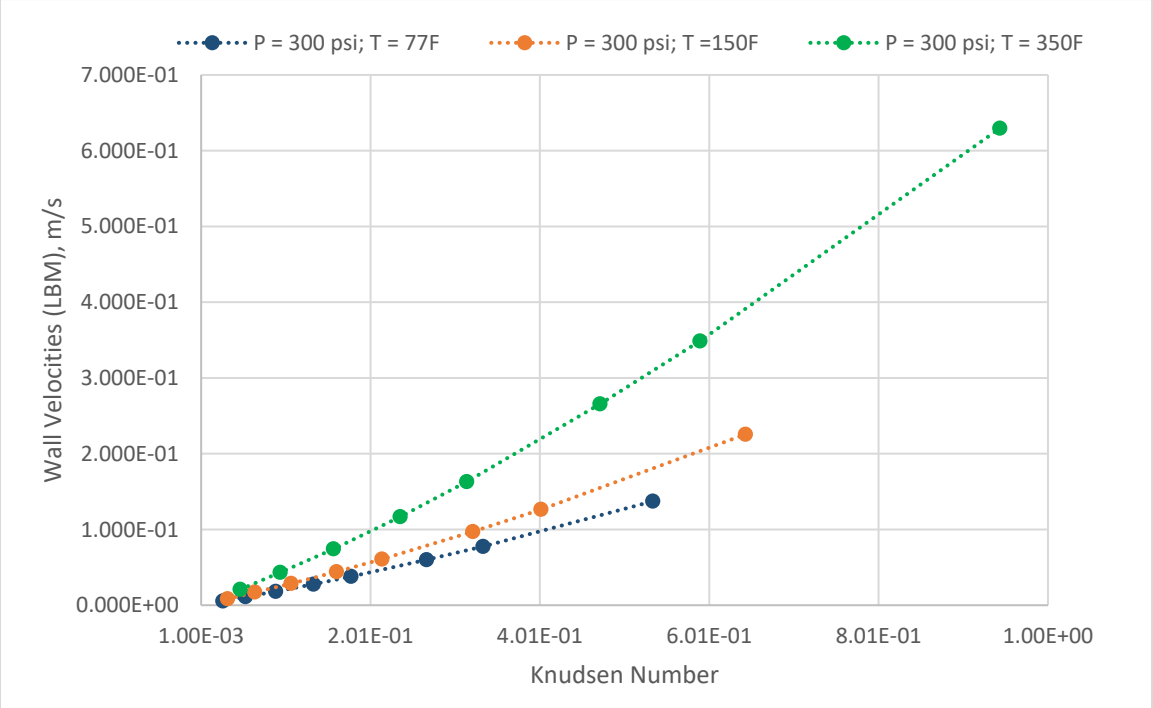

Figure 4-32: Plot displaying the wall velocity at lower pore pressure of 300 psi, varying temperature using LBM numerical solution against Knudsen number

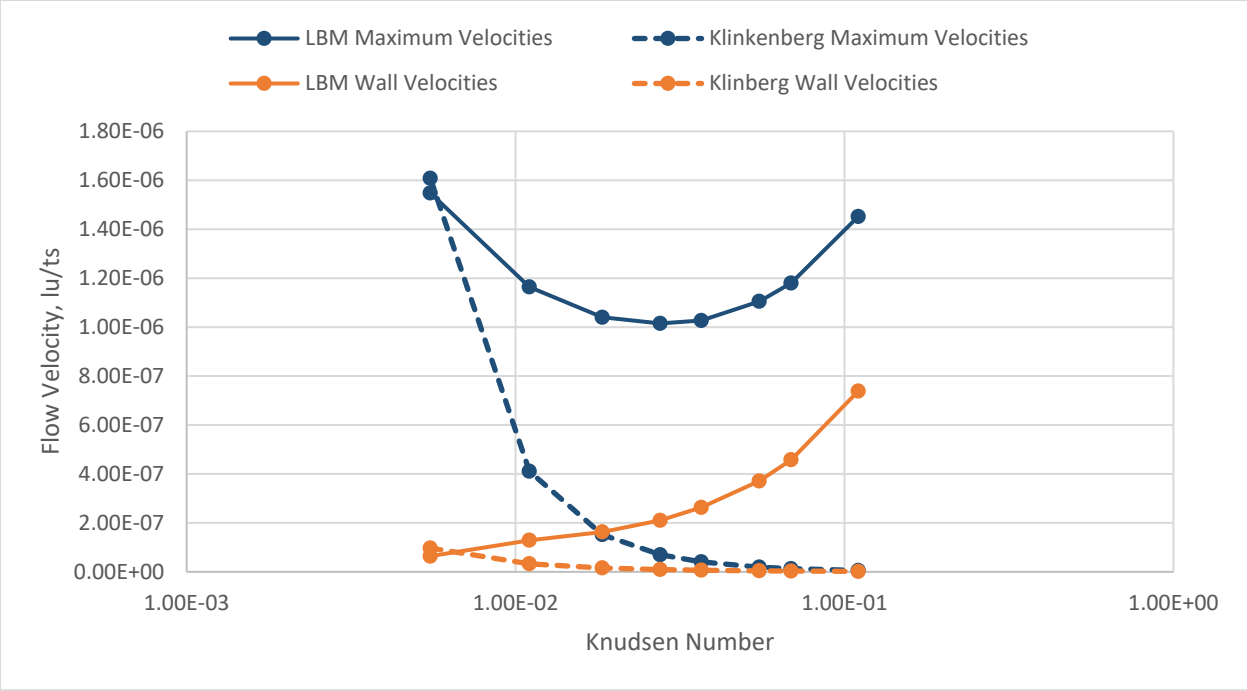

Figure 4-33: Plot displaying the maximum velocity and wall velocity at high pore pressure of 1623 psi and 77F temperature at various flow regimes comparing LBM solution and Klinkenberg slip flow equation

Figure 4-33 compares the maximum velocities and wall velocities from the developed LBM numerical solution and the Klinkenberg slip flow equation at a pressure of 1623 psi and 77F temperature. It is observed that most of the data points falls in the slip flow regime.

Looking at the maximum velocities (blue line- Figure 4-33): at larger capillary (100 nm) the maximum velocity from both the solutions are the same, as there are no huge interactions near the wall causing slippage or Knudsen diffusion. But as the capillary size decreases, the Klinkenberg solution maximum velocities dies out indicating no flow whereas the LBM solution maximum velocities initially show a dip until a critical Knudsen number (at 20 nm) after which the maximum velocity increases due to the fluid-solid interactions at the wall including slippage and double slippage effects.

Examining the wall velocities (orange line- Figure 4-33): Klinkenberg theory fails to capture the wall confinement and slippage effects near the wall when the flow regime shifts from continuum to higher Knudsen flow regimes, as molecules near the wall form a stationary wall where no interactions takes place resulting in zero wall velocity; whereas LBM simulation results show

increasing wall velocities with reduction in capillary width as the molecules in the mean free path endlessly collide generating high velocity in the vicinity of the wall.

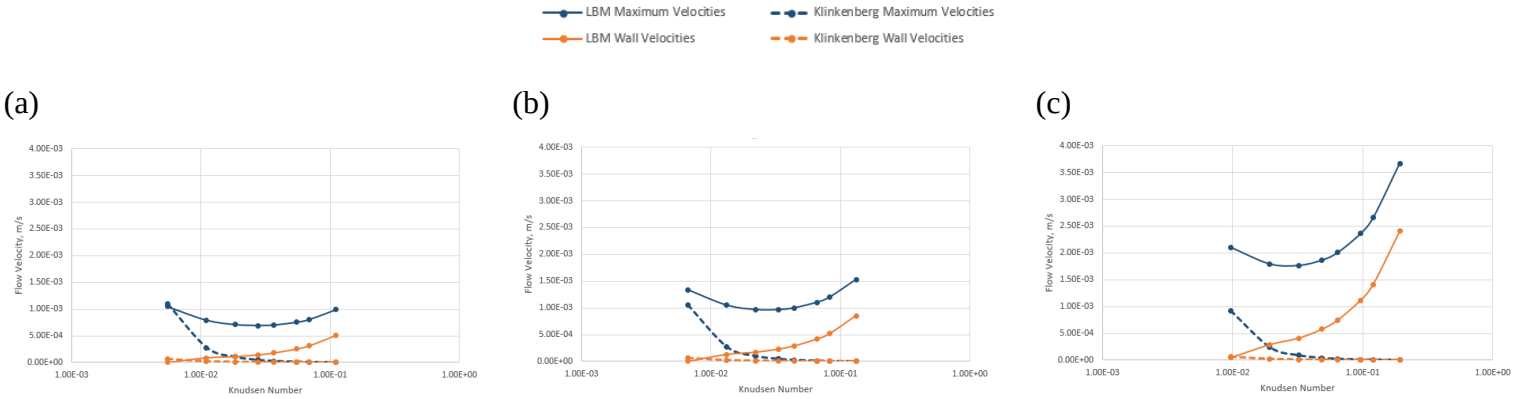

Figure 4-34: Plot displaying the maximum velocity and wall velocity at various flow regimes comparing LBM solution and Klinkenberg slip flow equation at pore pressure of 1623 psi and temperature of (a)77F (b) 150F (c) 350F in physical units

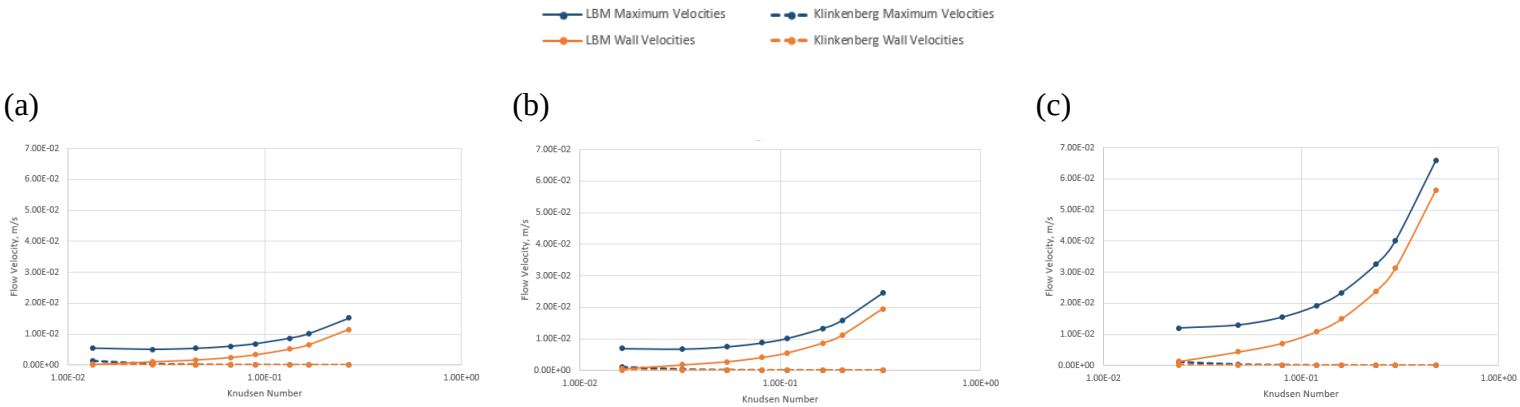

Figure 4-35: Plot displaying the maximum velocity and wall velocity at various flow regimes comparing LBM solution and Klinkenberg slip flow equation at pore pressure of 600 psi and temperature of (a)77F (b) 150F (c) 350F in physical units

Figure 4-34, Figure 4-35, and Figure 4-36 are plotted to analyze the effect of temperature and pressure on LBM numerical solution results, Klinkenberg slip flow equation results to study the flow velocity changes i.e. maximum center velocity and wall velocity changes. It is observed that as the pressure is decreased from 1623 psi to 600 psi to 300 psi, the magnitude of flow velocity increases from $10^{-3}m/s$ to $10^{-2}m/s$ to $10^{-1}m/s$ respectively.

Considering Figure 4-34 it is observed that the maximum center velocity and wall velocity calculated using LBM increases with increase in temperature due to the increased kinetic energy

of the molecules. However, for maximum velocity calculated through LBM solution, there is a dip in velocity showing a critical Knudsen number (at 20 nm) and then increases again for smaller capillary tubes due to addition of wall confinement effect. Whereas, the Klinkenberg maximum center velocity values die out as the flow regime shifts from slip to transition flow regime. The Klinkenberg slip flow equation failed to capture the wall velocity in slip flow regime.

As the pressure is reduced from 1623 psi to 600 psi and eventually to 300 psi, the Knudsen number regimes move from slip flow regime to slip-transition flow regimes. From Figure 4-35 and Figure 4-36 it is observed that Klinkenberg slip flow equation doesn't capture the maximum center velocity and wall velocity as much as the LBM numerical solution does due to the effect of wall confinement and Knudsen diffusion. Similar to above inferences made about LBM solution flow velocities, in this case too the LBM maximum center velocity and LBM wall velocity increases with increase in temperature and pressure.

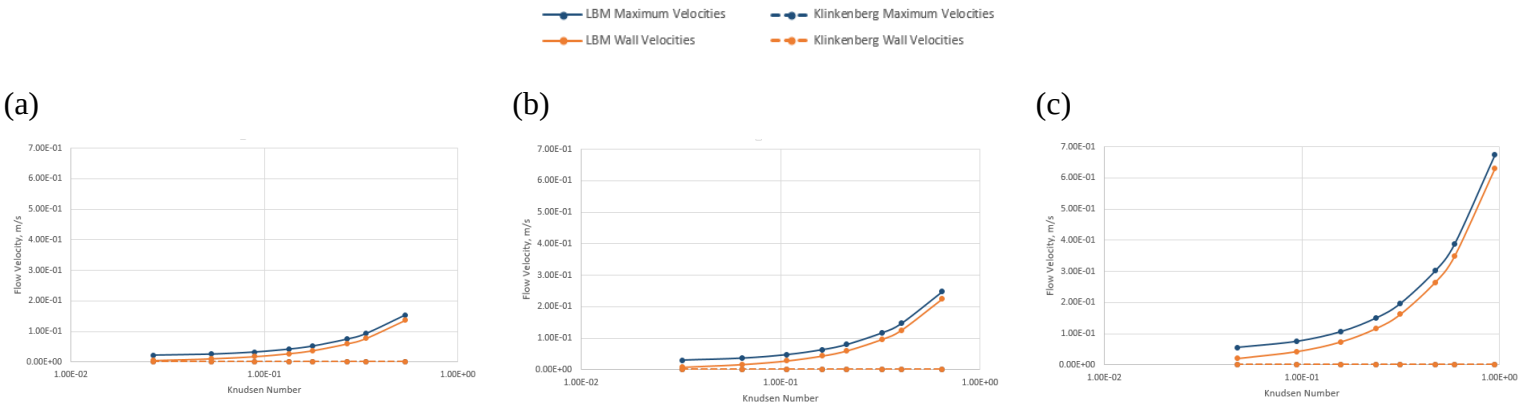

Figure 4-36: Plot displaying the maximum velocity and wall velocity at various flow regimes comparing LBM solution and Klinkenberg slip flow equation at pore pressure of 300 psi and temperature of (a)77F (b) 150F (c) 350F in physical units

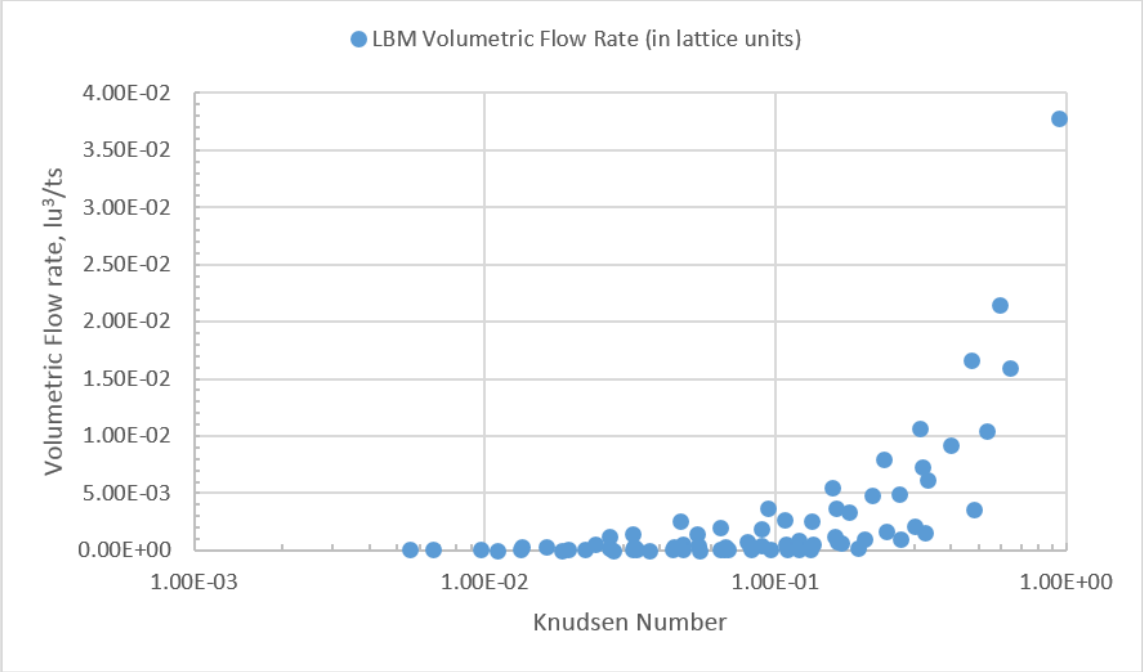

Figure 4-37: Plot displaying the maximum velocity and wall velocity at various flow regimes comparing LBM solution and Klinkenberg slip flow equation at pore pressure

Anomalies in gas dynamics in nanopores, such as Knudsen's minimum in the mass flow rate during pressure driven flows, are interpreted as constituting deviations from equilibrium associated with high Knudsen numbers and classified accordingly in the kinetic theory of gases. Dongari et al. [53], combined this approach with a description wherein the total mass flux through the channel is regarded as composed of a combination of convective and diffusive fluxes. Their scheme resulted in reasonably good agreement with data over the full Knudsen number range. However, the value of the Knudsen minimum was underpredicted. Dadzie and Brenner [54], pointed out the same additional diffuse mass-density flux term to lead correct predictions of experimental data in the slip-transition regime, including specifically the enhanced mass flow rate phenomenon in microchannels, an observation confirmed separately also by Veltzke and Thaming [55]. The experimental data used was based on Helium mass flow rate measurements in a single microchannel by Ewart et al. 2007 [56]. However, in this experiment the adsorption and adsorbed gas transport that can lead to higher slippage velocity and mass flow rate is not considered. Using LBM simulation of adsorptive gas Methane in a similar single microchannel we have investigated the impact of Knudsen number on volumetric flow rate in Figure 4-37. It is observed that the

minimum Knudsen number can happen earlier at Kn= 0.2 considering the gas adsorption and adsorbed phase transport in organic nanopores.

4.4. Comparison of slip flow with various analytically derived solutions

The next section analyzes the effect of slip flow, displaying the normalized slip velocity with the changing flow regime shown in Figure 4-38.

The normalized slip velocity is calculated using the Eq. (3-26) [43] which is a function of Knudsen number. Various analytically derived and empirical corrected second-order slip model were developed, their normalized slip velocity is calculated using first-order slip coefficient (C_1) and second-order slip coefficient (C_2) described in Table 3-2. From the Eq. (3-26) it is understood that the coefficient C_2 impacts in deviation from straight line when normalized slip velocity is plotted against Knudsen number. This curve exponentially increase (C_2 positive), decrease (C_2 negative) or show no difference i.e. linear (C_2 =0) based on the second-order slip coefficient value.

The LBM results shown previously displays high impact of double slippage leading to high velocities near the wall and overall increased velocity profile. Referring to the research of Fathi et al 2012[1], where the double slippage was first introduced through experimental results from shale rock samples; in this segment we use the double-slip Klinkenberg slip permeability equation which quantifies the molecular streaming effect Eq. (3-30) to investigate the influence of having only first-order slip coefficient expressed in Eq. (3-32). In the re-arranged equation (3-32), it is observed that only including the first-order slip coefficient impacts the normalized slip equation. Thus, to correlate the fluid behavior in recognizing the importance of just the coefficient C_1 and not considering the second order slip order equation i.e. $C_2 = 0$; new first-order slip coefficients are introduced (Table 4-2) to match the profiles generated when both first and second-order slip coefficients are considered as shown in Figure 4-38.

Table 4-2-: List of various second-order slip model coefficients and matching first-order slip coefficient

Authors	C_1	C_2	**Match C_1**
Schamberg, 1947 [45]	1	$5\pi/2$	1.2
Cercignani, 1964 [46]	1.1466	0.9756	1.31

Deissler, 1964 [48]	1	9/8	1.19
Hsia and Domoto, 1983 [50]	1	0.5	1.1
Beskok et al., 1996 [52]	1	-0.5	0.93
LBM Solution Results			2.35

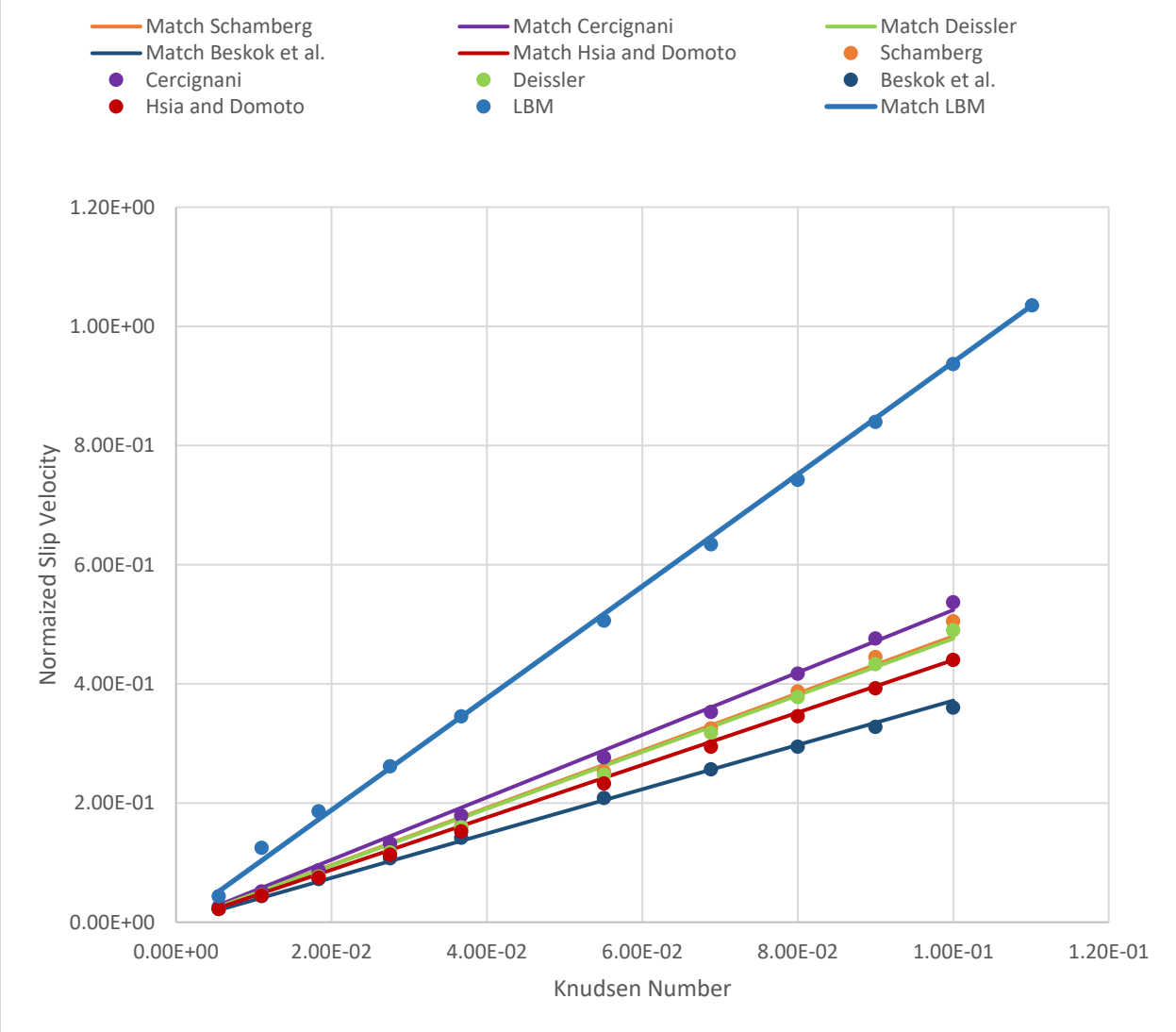

Figure 4-38: Plot displaying the normalized slip velocities compared using second-order slip models and the LBM simulation results at high pore pressure of 1623 psi and 77F temperature at various flow regimes

For this segment, slip flow regime is considered ($10^{-3} < Kn \leq 10^{-1}$) and it is observed from Figure 4-38 that even when the second-order slip coefficient is neglected, the normalized slip flow velocities match the earlier second-order slip model profile with only slight deviation. LBM results are also plotted which shows higher slip velocity as LBM simulation incorporates the influence of high molecular interaction in the mean free path layer leading to higher kinetic energy and velocities due to the effect of double slippage.

However, while extending the flow regime from earlier slip flow to transition flow regime, it is observed that the match values as introduced in Table 4-2, fail to capture the slip velocity profile as seen in Figure 4-39 due the inclusion of second-order slip coefficient to calculate the normalized slip velocity.

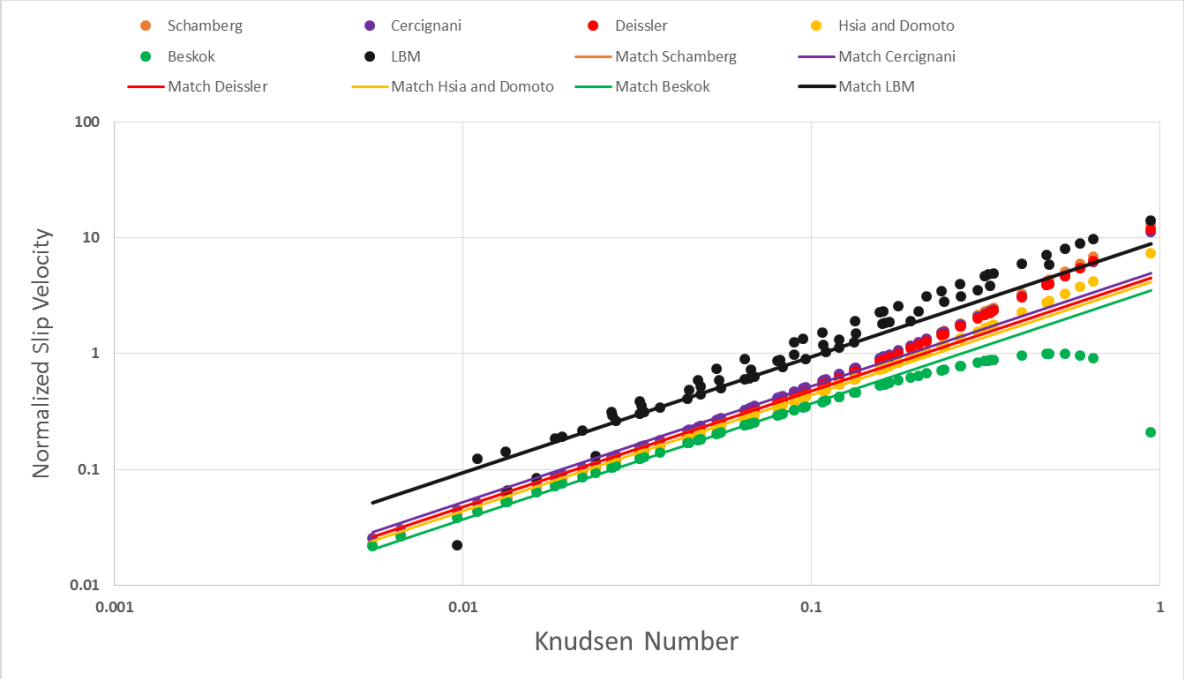

Figure 4-39: Plot displaying the normalized slip velocities compared using second-order slip models and the LBM simulation results of slip and transition flow regimes

4.5. Conclusion

This study focuses on the non-ideal single phase single component gas dynamics in organic nano capillary tubes in different flow regime conditions, ranging between continuum to slip to high transition flow. The dimensionless number, Knudsen number, defines the flow regimes based on capillary pore width and the mean free path. The mean free path of the molecules determines the

average collision distance between two particles and is dependent on the type of the gas, pore pressure and temperature.

To understand the fluid flow behavior of methane gas on a broader outlook, the study was carried out where the pore pressure and reservoir temperature is altered between 1623 psi, 600 psi, 300 psi and 77F, 150F, 350F respectively to consider the effects of pressure and temperature on fluid flow and at varying capillary widths. Using the analytical Poiseuille flow, analytical Klinkenberg slip equation, and modified Klinkenberg slip flow equation, the maximum center velocity and wall velocity based on flow regimes were examined. From this exercise, it was inferred that the analytical solutions capture the flow only at larger capillary widths where the Knudsen number is low, falling in the continuum and maybe can be extended to early slip flow regimes.

To summarize the effect of different reservoir conditions on the ***analytical solutions***, it is observed that the maximum velocity at the center of the capillary is dominant at low pressure and low temperature and the slip velocity is observed only in larger pores. And as the pore size reduces to 5 nm, the permeability of the fluid decreases resulting in decrease in flow rate and hence the velocity.

Next, the effect of slippage, wall confinement, Knudsen diffusion, and double slippage were analyzed through the new ***LBM-Ls*** model[8]. In this model, the system is considered closed by applying periodic boundary condition at the capillary inlet and outlet. The modified Langmuir slip boundary condition is applied to account for the adsorbed phase transport and slip flow by the walls. This model incorporates the molecular interactions (adsorptive/cohesive forces) between the fluid particles (fluid-fluid, fluid-solid) leading to a viscous-flow inside the capillary. For better understanding the results presented in this study are calculated both in lattice units and physical units.

Implementing the LBM numerical simulation, the gas behavior is studied across capillary widths ranging from 100 nm to 5 nm. It is observed that at lower pressures, slippage is higher due to the larger mean free path of gas molecules wrt to the pore size. The range of Knudsen number when slippage occurs increases with decrease in pressure, and is dependent on the size of the pore through which gas flows. Under conditions where slippage occurs, Poiseuille and Darcy laws do not hold good. However at higher pressures, effect of slippage is not extensively seen as the mean

free path of gas molecules become smaller wrt to the pore size. But as the pore size reduces at higher pressures, slippage conditions become prevalent leading to high wall velocity.

As the temperature increases with reducing capillary pore widths, the wall velocity keeps increasing to a point where the flow in smaller pores become greater than larger pore and the wall velocity becomes predominant. A critical Knudsen number comes into the role which alters the flow pattern where not only the wall velocity increases but the center velocity increases showing the influence of double slippage, introduced earlier by Fathi et al[1], caused due to the unceasing molecular collisions in the mean free path where the bounced back molecules carry their momenta to the bulk fluid at the center of the capillary causing molecular streaming effect on the fluid flow across the capillary. Thus, leading to amplified velocity profile.

Lastly, the normalized slip velocity of LBM is compared with various analytically derived and empirical corrected second-order slip models and based on the double-slip Klinkenberg slip permeability equation, which quantifies the molecular streaming effect, the normalized slip velocity profiles are matched with new set of slip coefficients.

Bibliography

[1] E. Fathi, A. Tinni, and I. Y. Akkutlu, "Correction to Klinkenberg slip theory for gas flow in nano-capillaries," *Int. J. Coal Geol.*, vol. 103, pp. 51–59, 2012.

[2] A. G. Adesida, I. Y. Akkutlu, D. E. Resasco, and C. S. Rai, "SPE 147397 Kerogen Pore Size Distribution of Barnett Shale using DFT Analysis and Monte Carlo Simulations," pp. 1–14, 2011.

[3] W. H. Fissell, A. T. Conlisk, and S. Datta, "High Knudsen number fluid flow at near-standard temperature and pressure conditions using precision nanochannels," pp. 425–433, 2011.

[4] S. M. Kang, E. Fathi, R. J. Ambrose, I. Y. Akkutlu, and R. F. Sigal, "Carbon Dioxide Storage Capacity of Organic-Rich Shales," *SPE J.*, pp. 1–14, 2011.

[5] K. Wu, X. Li, C. Wang, W. Yu, and Z. Chen, "Model for Surface Di ff usion of Adsorbed Gas in Nanopores of Shale Gas Reservoirs," 2015.

[6] J. Wang, L. Chen, Q. Kang, and S. S. Rahman, "The lattice Boltzmann method for isothermal micro-gaseous flow and its application in shale gas flow : a review."

[7] A. Elamin, E. Fathi, and S. Ameri, "Simulation of Multicomponent Gas Flow and Condensation in Marcellus Shale Reservoir," *SPE J.*, 2013.

[8] E. Fathi, I. Y. Akkutlu, and A. Texas, "Lattice Boltzmann Method for Simulation of Shale Gas Transport in Kerogen," no. February, pp. 27–37, 2013.

[9] M. C. Sukop and D. T. Throne Jr., *Lattice Boltzmann Modeling An Introduction for Geoscientists and Engineers*. 2006.

[10] Y. H. Qian, D. D'Humieres, and P. Lallemand, "Lattice BGK Models for Navier-Stokes Equation."

[11] P. L. Bhatnagar, E. P. Gross, and M. Krook, "A Model for Collision Processes in Gases. I.

Small Amplitude Processes in Charged and Neutral One-Component Systems," 1954.

[12] A. A. Mohamad, *Lattice Boltzmann Method*, vol. 30. 1998.

[13] B. Chopard *et al.*, "Cellular Automata and Lattice Boltzmann Techniques: an Approach To Model and Simulate Complex Systems," *Adv. Complex Syst.*, vol. 5, no. 02n03, pp. 103–246, 2002.

[14] L. Luo, W. Liao, X. Chen, Y. Peng, and W. Zhang, "Numerics of the lattice Boltzmann method : Effects of collision models," *Phys. Rev. E*, vol. 56710, no. 83, pp. 1–24, 2011.

[15] I. Ginzburg, "Equilibrium-type and link-type lattice Boltzmann models for generic advection and anisotropic-dispersion equation," vol. 28, pp. 1171–1195, 2005.

[16] Z. Guo, C. Zheng, and B. Shi, "Lattice Boltzmann equation with multiple effective relaxation times for gaseous microscale flow," no. October 2007, pp. 1–12, 2008.

[17] X. He, S. Chen, and G. D. Doolen, "A Novel Thermal Model for the Lattice Boltzmann Method in Incompressible Limit," *J. Comput. Phys.*, vol. 146, no. 1, pp. 282–300, 1998.

[18] K. Suga, S. Takenaka, T. Ito, M. Kaneda, T. Kinjo, and S. Hyodo, "Evaluation of a lattice Boltzmann method in a complex nanoflow," *Phys. Rev. E - Stat. Nonlinear, Soft Matter Phys.*, vol. 82, no. 1, pp. 1–10, 2010.

[19] K. Suga, "Corrigendum : Lattice Boltzmann methods for complex micro flows : applicability and limitations for practical applications," 2013.

[20] M. C. Sukop and D. Or, "Lattice Boltzmann method for modeling liquid-vapor interface configurations in porous media," vol. 40, pp. 1–11, 2004.

[21] Q. Zou and X. He, "On pressure and velocity boundary conditions for the lattice Boltzmann BGK model," vol. 9, no. 6, 1997.

[22] L. J. Klinkenberg, "The Permeability Of Porous Media To Liquids And Gases.," *Am. Pet. Institute.*, 1941.

[23] A. Ashra and R. Chalaturnyk, “International Journal of Coal Geology Expansion of the Klinkenberg â€TM s slippage equation to low permeability porous media,” vol. 123, pp. 2–9, 2014.

[24] N. S. Martys and H. Chen, “Simulation of multicomponent fluuids in complex three-dimensional geometries by the lattice Boltzmann method,” *Phys. Rev. E*, vol. 53, no. 1, 1996.

[25] D. Or and M. Tuller, “Cavitation during desaturation of porous media under tension,” vol. 38, no. 5, pp. 1–4, 2002.

[26] X. Nie, G. D. Doolen, and S. Chen, “Lattice-Boltzmann Simulations of Fluid Flows in MEMS,” vol. 107, no. April, 2002.

[27] S. Succi, “Mesoscopic Modeling of Slip Motion at Fluid-Solid Interfaces with Heterogeneous Catalysis North wall s r Streamwise flow speed,” no. 1, pp. 1–4, 2002.

[28] J. C. Maxwell, “On Stresses in Rarifed Gases arising from Inequalities of Temperature.,” *Philisophical Trans. R. Soc. London*, vol. 170, pp. 231–256, 1879.

[29] R. S. Myong, “A generalized hydrodynamic computational model for rarefied and microscale diatomic gas flows,” *J. Comput. Phys.*, vol. 195, pp. 655–676, 2004.

[30] H. M. Kim, D. Kim, W. T. Kim, P. S. Chung, and M. S. Jhon, “Langmuir Slip Model for Air Bearing Simulation Using the Lattice Boltzmann Method,” *IEEE Trans. Magn.*, vol. 43, no. 6, pp. 2244–2246, 2007.

[31] S. Chen and Z. Tian, “Simulation of microchannel flow using the lattice Boltzmann method,” *Physica A*, vol. 388, pp. 4803–4810, 2009.

[32] R. S. Myong, J. M. Reese, R. W. Barber, and D. R. Emerson, “Velocity slip in microscale cylindrical Couette flow : The Langmuir model,” *Phys. Fluids*, vol. 87105, no. 17, 2005.

[33] E. Fathi and I. Y. Akkutlu, “Mass Transport of Adsorbed-Phase in Stochastic Porous Medium with Fluctuating Porosity Field and Nonlinear Gas Adsorption Kinetics,” *Transp.*

Porous Media, vol. 91, pp. 5–33, 2011.

[34] E. Fathi and I. Y. Akkutlu, "Matrix Heterogeneity Effects on Gas Transport and Adsorption in Coalbed and Shale Gas Reservoirs," *Transp. Porous Media*, vol. 80, pp. 281–304, 2009.

[35] S. Chen and Z. Tian, "Simulation of thermal micro-flow using lattice Boltzmann method with Langmuir slip model," *Int. J. Heat Fluid Flow*, vol. 31, no. 2, pp. 227–235, 2010.

[36] S. Chen and G. D. Doolen, "Lattice Boltzmann method for fluid flows," *Annu. Rev. Fluid Mech.*, vol. 30, pp. 329–64, 1998.

[37] G. H. Tang, W. Q. Tao, and Y. L. He, "Thermal boundary condition for the thermal lattice Boltzmann equation," *Phys. Rev. E*, vol. 72, no. 16703, pp. 1–6, 2005.

[38] G. H. Tang, X. J. Gu, R. W. Barber, D. R. Emerson, and Y. H. Zhang, "Lattice Boltzmann simulation of nonequilibrium effects in oscillatory gas flow," *Physica A*, vol. 78, no. 0.6706, pp. 1–8, 2008.

[39] X. Shan and H. Chen, "Lattice Boltzmann model for simulating flows with multiple phases and components," *Phys. Rev. E*, vol. 47, no. 3, 1993.

[40] X. He and G. D. Doolen, "Thermodynamic Foundations of Kinetic Theory and Lattice Boltzmann Models for Multiphase Flows," *J. Stat. Phys.*, vol. 107, pp. 309–328, 2002.

[41] R. J. Ambrose, R. C. Hartman, M. Diaz-campos, I. Y. Akkutlu, and C. H. Sondergeld, "Shale Gas-in-Place Calculations Part I : New Pore-Scale Considerations," *SPE J.*, no. March, pp. 219–229, 2012.

[42] B. R. Didar, "Multi-component shale gas-in-place calculations," University of Oklahoma, 2012.

[43] N. Okamoto, Y. Liang, S. Murata, T. Matsuoka, T. Akai, and S. Takagi, "Slip Velocity and Permeability of Gas Flow in Nanopores for Shale Gas," 2015.

[44] G. H. Tang, W. Q. Tao, and Y. L. He, "Gas slippage effect on microscale porous flow using the lattice Boltzmann method," *Phys. Rev. E*, vol. 72, pp. 1–8, 2005.

[45] R. Schamberg, “The Fundamental Differential Equations and the Boundary Conditions for High Speed Slip-Flow, and Their Application to Several Specific Problems,” California Institute of Technology, 1947.

[46] C. Cercignani, “Higher Order Slip According to the Linearized Boltzmann Equation,” 1964.

[47] N. G. Hadjiconstantinou, “Comment on Cercignani’s second-order slip coefficient,” *Phys. Fluids*, vol. 15, no. 8, pp. 2352–2354, 2003.

[48] R. G. Deissler, “AN ANALYSIS OF SECOND-ORDER SLIP FLOW AND TEMPERATURE-JUMP BOUNDARY CONDITIONS FOR RAREFIED GASES,” *Int. J. Heat Mass Transf.*, vol. 7, pp. 681–694, 1964.

[49] A. K. Sreekanth, “Slip flow of nitrogen gas through long circular tubes, measuring mass flow, pressure drop and cross sectional velocity profiles,” *Acad. Press. Inc., New York, USA*, vol. 1970004225, pp. 667–680, 1969.

[50] Y.-T. Hsia and G. A. Domoto, “An Experimental Investigation of Molecular Rarefaction Effects in Gas Lubricated Bearings at Ultra-Low Clearances,” *J. Lubr. Technol.*, vol. 105, pp. 120–129, Jan. 1983.

[51] Y. Mitsuya, “Modified Reynolds Equation for Ultra-Thin Film Gas Lubrication Using 1.5-Order Slip-Flow Model and Considering Surface Accommodation Coefficient,” *J. Tribol.*, vol. 115, no. 2, pp. 289–294, Apr. 1993.

[52] A. Beskok, G. E. Karniadakis, and W. Trimmer, “Rarefaction and Compressibility Effects in Gas Microflows,” *J. Fluids Eng.*, vol. 118, no. 3, pp. 448–456, Sep. 1996.

[53] N. Dongari, A. Sharma, and F. Durst, “Pressure-driven diffusive gas flows in micro-channels : from the Knudsen to the continuum regimes,” pp. 679–692, 2009.

[54] S. K. Dadzie and H. Brenner, “Predicting enhanced mass flow rates in gas microchannels using nonkinetic models,” vol. 36318, pp. 1–10, 2012.

[55] T. Veltzke and J. Thöming, “An analytically predictive model for moderately rarefied gas

flow," pp. 406–422, 2012.

[56] T. EWART, P. PERRIER, I. A. GRAUR, and J. G. M'EOLANS, "Mass flow rate measurements in a microchannel, from hydrodynamic to near free molecular regimes ′," vol. 584, pp. 337–356, 2007.

Appendix

Knudsen number values at different pressures

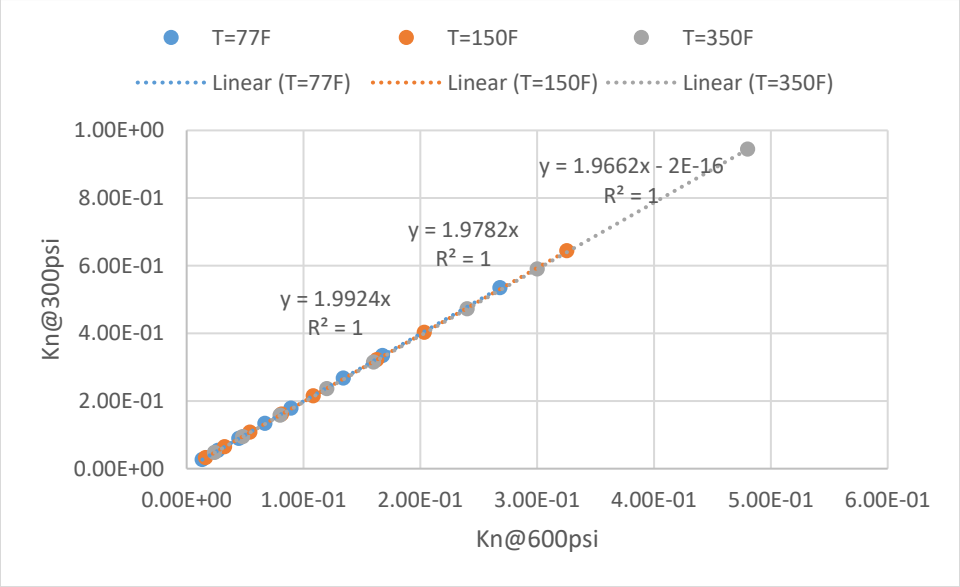

Figure 0-1: Range of Knudsen number values plotted between 600 psi and 300 psi

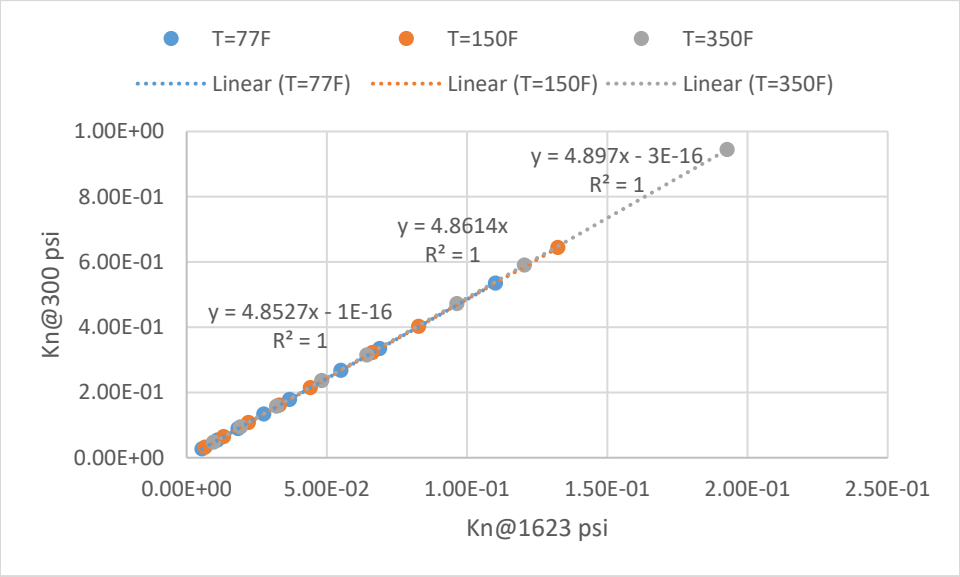

Figure 0-2: Range of Knudsen number values plotted between 1623 psi and 300 psi

Table 0-1: Kinematic Viscosity Values at different reservoir conditions

Pore Pressure	Reservoir Temperature	Kinematic Viscosity, cm2/s
1623 psi	77F	1.73E-03
	150 F	2.21E-03
	350 F	3.71E-03
600 psi	77F	4.21E-03
	150 F	5.44E-03
	350 F	9.25E-03
300 psi	77F	8.38E-03
	150 F	1.08E-02
	350 F	1.82E-02

Table 0-2: Ratio of Kinematic Viscosities to acquire the slop value

	Kn b/w 1623 psi & 600 psi	Kn b/w 600 psi & 300 psi	Kn b/w 1623 psi & 300 psi
77F	2.43	1.99	4.85
150 F	2.46	1.98	4.86
350 F	2.49	1.97	4.90

Conversion from physical units to lattice units

The thermodynamic and transport properties of pure hydrocarbon fluids and fluid mixtures up to 20 components can be predicted using an interface, known as SUPERTRAPP. This interactive computer program executes phase equilibria calculations to anticipate the thermophysical properties of all phases and the feed.

Considering a single phase, methane gas at Temperature $T = 25℃$ and Pore pressure $P = 2500\ psi$. The thermophysical properties obtained are displayed in

Table 0-3: Thermophysical properties of methane gas at 2500 psi and 25 C using SUPERTRAPP program

Molar Mass, $M, gm/mol$	16.0425
Compressibility Factor, z	0.82297

Density, $\rho_g, gm/cm^3$	0.13554
Dynamic Viscosity, $\mu, \frac{gm}{cm-s}$	1.81E-04
Universal Gas Constant, $R, \frac{erg}{K-mol}$	8.31E+07

Table 0-4: Assumed capillary size and measured gas storage capacity for methane gas

Length of capillary tube, L	100 nm (50 lu)
Width of capillary tube, H	20 nm (10 lu)
Langmuir pressure, P_L, psi	1800
Adsorbed gas density, $\rho_{ads}, \frac{gm}{cm^3}$	0.4
Maximum adsorption capacity, $C_{\mu s}, \frac{mol}{cm^3}$	0.025

Calculations

$$P_p = 2500\ psi = 1.7237 \times 10^8 \frac{gm}{cm.s^2}$$

$$P_L = 1800\ psi = 1.241 \times 10^8 \frac{gm}{cm.s^2}$$

$$\left[Conversion: 1\ psi = 6894.7573\ Pa = 68947.573 \frac{gm}{cm.s^2}\right]$$

$$T = 25℃ = 293.15\ K\ [Conversion: 0℃ = 273.15\ K]$$

Conversion from 'cm' to 'lu'

$$H = 20\ nm = 10\ lu \rightarrow 20 \times 10^{-7} cm = 10\ lu$$

$$\therefore \mathbf{1\ cm = 5 \times 10^6\ lu}$$

Conversion from 'sec' to 'ts'

$$\nu = \frac{\mu}{\rho} = 0.001331929 \frac{cm^2}{s}$$

From the definition of Knudsen number, we have:

$$Kn = \frac{\lambda}{H} \; ; \; \frac{\lambda}{H} = \frac{\mu}{\rho H}\sqrt{\frac{\pi\, m}{2k_B T}}$$

$$Kn = \frac{\nu}{H}\sqrt{\frac{\pi}{2\left(\frac{k_B T}{m}\right)}} = \frac{\nu}{H}\sqrt{\frac{\pi}{2\left(\frac{RT}{M}\right)}}$$

Relationship between k_B and R:

$$k_B = \frac{R}{N_R} \; [and \; N \times m = M]$$

$$\therefore Kn = \frac{\nu}{H}\sqrt{\frac{\pi}{2\left(\frac{RT}{M}\right)}}$$

$$Kn = \frac{\nu}{H}\sqrt{\frac{\pi}{2\left(\frac{RT}{M}\right)}} = \frac{0.00133193}{20 \times 10^{-7}}\sqrt{\frac{\pi}{2\left(\frac{8.314 \times 10^7 \times 298.15}{16.0425}\right)}} = 2.12 \times 10^{-2}$$

Re-arranging the Knudsen equation to calculate kinematic viscosity in lattice units.

$$\nu = \frac{Kn\,.H}{\sqrt{\frac{\pi}{2(RT)}}} = \frac{Kn\,.H}{\sqrt{\frac{3\pi}{2}}} = \frac{2.12 \times 10^{-2} \times 10}{\sqrt{\frac{3\pi}{2}}}$$

$$= 0.097812\,\frac{lu^2}{ts}\left[as \; RT = \frac{1}{3} \,\&\, M \approx 1 \; in \; lattice \; units\right]$$

$$Equating \; \nu \; in \frac{cm^2}{s} and \frac{lu^2}{ts} \rightarrow \; 0.001331929\,\frac{cm^2}{s} = 0.097812\,\frac{lu^2}{ts}$$

$$\therefore \mathbf{1 \; sec = 3.4043 \times 10^{11} \; ts}$$

Calculation of maximum velocity in y-direction, Reynold's number

From Poiseuille flow definition:

$$u(y) = \frac{G^*}{2\mu}(a^2 - x^2)$$

$$where, G^* = \begin{cases} (P_{in} - P_{out})/L \\ \rho g \end{cases} \; (or)$$

$$\frac{dP}{dL} = 1270007.008 \frac{gm}{cm^2.s^2}$$

$$u(y)_{max} = \frac{\left(\frac{dP}{dL}\right)}{2\mu}(a^2) = \frac{\left(\frac{dP}{dL}\right)}{2\mu}\left(\frac{H}{2}\right)^2 [at\ x = 0]$$

$$u(y)_{max} = \frac{1270007.008 \frac{gm}{cm^2.s^2}}{2 \times \left(1.8 \times 10^{-4} \frac{gm}{cm.s}\right)}\left(\frac{2 \times 10^{-6}\ cm}{2}\right)^2 = 3.517 \times 10^{-3} \frac{cm}{s} = 5.166 \times 10^{-8} \frac{lu}{ts}$$

$$u_{avg} = \frac{2}{3} u(y)_{max} = \frac{2}{3}(5.166 \times 10^{-8}) = 3.44 \times 10^{-8} \frac{lu}{ts}$$

$$Re = \frac{DV\rho}{\mu} = \frac{DV}{\nu} = \frac{H.U_{avg}}{\nu} = \frac{10\ lu \times\ 3.44 \times 10^{-8}\ \frac{lu}{ts}}{0.097812\ \frac{lu^2}{ts}} = 3.52 \times 10^{-6}$$

Conversion from 'gm' to 'mu'

From Ideal Gas law, we have:

$$PV = nRT \rightarrow PV = \frac{m}{M}RT \rightarrow P = \frac{m}{V}\frac{1}{M}RT \rightarrow P = \rho\frac{RT}{M} \rightarrow P = \left(\frac{\rho}{M}\right)RT$$

$$\frac{\rho}{M} = \frac{0.135544\ gm/cm^3}{16.0425\ gm/mol} = 0.00844906 \frac{mol}{cm^3}$$

$$\left(\frac{\rho}{M}\right)RT = \frac{1}{3}(lattice\ units)$$

$$\left(0.00844906 \frac{mol}{cm^3}\right) \times \left(8.314 \times 10^7 \frac{gm.cm^2}{s^2.K.mol}\right) \times (298.15\ K) = \frac{1}{3}$$

$$2.09 \times 10^8 \frac{gm}{cm.s^2} = \frac{1}{3}\frac{mu}{lu.ts^2}$$

$$2.09 \times 10^8 \frac{gm}{(5 \times 10^6\ lu) \times (3.4 \times 10^{11})^2 ts^2} = \frac{1}{3}\frac{mu}{lu.ts^2}$$

$$\therefore \mathbf{1\ gm = 9.22 \times 10^{20} mu}$$

Conversion from 'mol' to 'l-mol'

For single component single phase and single component multi-phase, the value of RT is fixed as

$$RT = \frac{1}{3}$$

$$\left(8.314 \times 10^7 \frac{gm.cm^2}{s^2.K.mol}\right) \times (293.15\ K) = \frac{1}{3}\frac{mu.lu^2}{ts^2.l-mol}$$

$$(2.48 \times 10^{10})\frac{gm.cm^2}{s^2.mol} \rightarrow (2.48 \times 10^{10})\frac{(9.22 \times 10^{20})mu.(5 \times 10^6)^2 lu^2}{(3.4 \times 10^{11})^2 ts^2.mol} = \frac{1}{3}\frac{mu.lu^2}{ts^2.lmol}$$

$$\therefore \boldsymbol{1\ mol = 1.48 \times 10^{22}\ l-mol}$$

Verification

$$M = 16.0425\frac{gm}{mol} = \frac{16.0425 \times (9.22 \times 10^{20}\ mu)}{1.48 \times 10^{22}\ l-mol} = 0.9994 \approx 1$$

Thus the conversions are true and valid.

Calculation of the local wall velocity

$$U_{surf} = \left(\frac{D_S}{D_K \rho_{ads}}\right)\left[\rho_g U_{g,slip}\frac{KC_{\mu s}}{(1+KC)^2}\right] = \left(\frac{D_s}{D_k}\right)\left(\frac{KC_{\mu s}}{\rho_{ads}}\right)(\rho_g U_g)\ \frac{1}{(1+KC)^2} =$$

$$= \left(\frac{D_s}{D_k}\right)\left(\frac{KC_{\mu s}}{\rho_{ads}}\right)(\rho_g U_g)\ \frac{1}{\left(1+K\left(\frac{\rho_g}{M}\right)\right)^2}$$

Considering an analogy between the equilibrium Langmuir isotherm equations expressed in terms of adsorbed gas amounts and pore pressure:

$$\frac{C_\mu}{C_{\mu s}} = \frac{KC}{1+KC}\ and\ \frac{V_a}{V_{amax}} = \frac{\frac{1}{P_L}P}{1+\frac{1}{P_L}P};\ we\ get\ KC = \frac{P}{P_L}$$

$$PV = nzRT \rightarrow\ P = \left(\frac{n}{V}\right)zRT \rightarrow\ C = \frac{P}{zRT}$$

$$KC = \frac{P}{P_L} \rightarrow K\frac{P}{RT} = \frac{P}{P_L}\ \therefore K = \frac{RT}{P_L} = \frac{8.314 \times 10^7 \frac{gm.cm^2}{s^2.K.mol} \times 298.15\ K}{124105631.04\ \frac{gm}{cm.s^2}} = 164.385\frac{cm^3}{mol}$$

$$K = 164.385\ \frac{(5 \times 10^6\ lu)^3}{(1.48 \times 10^{22}\ l-mol)} = 1.39\frac{lu^3}{l-mol}$$

$$PV = nzRT \rightarrow\ PM = \left(\frac{nM}{V}\right)zRT \rightarrow\ PM = \rho zRT \rightarrow \frac{P}{zRT} = \frac{\rho}{M}$$

$$\therefore C = \frac{P}{zRT} = \frac{\rho}{M}$$

$$\rho_{ads} = 0.4\frac{gm}{cm^3} = 0.4 \times \frac{9.22 \times 10^{20} mu}{(5 \times 10^6\ lu)^3} = 2.95\frac{mu}{lu^3}$$

$$C_{\mu s} = 0.025\frac{mol}{cm^3} = 0.025\ \frac{1.48 \times 10^{22} l - mol}{(5 \times 10^6 lu)^3} = 2.96\frac{l - mol}{lu^3}$$

$$U_{surf} = \left(\frac{D_s}{D_k}\right)\left(\frac{KC_{\mu s}}{\rho_{ads}}\right)(\rho_g U_g)\ \frac{1}{\left(1 + K\left(\frac{\rho_g}{M}\right)\right)^2}$$

$$U_{surf} = \left(\frac{D_s}{D_k}\right)\left(\frac{1.39\frac{lu^3}{l - mol} \times 2.96\frac{l - mol}{lu^3}}{2.95\frac{mu}{lu^3}}\right)(\rho_g U_g)\ \frac{1}{\left(1 + 1.39\frac{lu^3}{l - mol}\left(\frac{\rho_g}{1}\right)\right)^2}$$

$$U_{surf} = \left(\frac{D_s}{D_k}\right)(1.395)(\rho_g U_g)\ \frac{1}{\left(1 + 1.39\rho_g\right)^2}$$